Karl-Franzens-Universität Graz
Institut für Physik

SYMMETRIES OF QCD AT HIGH TEMPERATURE

Dissertation

zur Erlangung des akademischen Grades eines

Doktor der Naturwissenschaften

an der

Karl-Franzens-Universität Graz

vorgelegt von

CHRISTIAN ROHRHOFER

und betreut durch

Assoz. Prof. Dr. L. GLOZMAN.

Graz, Dezember 2018

Abstract

The dynamics of Quantum Chromodynamics (QCD) at high temperatures are subject of current theoretical and experimental research. In large collider experiments a state of matter is produced, whose properties differ greatly from ordinary hadronic matter in vacuum. In this thesis, lattice methods are applied to study the symmetry properties of strongly interacting matter at high temperatures. Most notably, the theoretically expected restoration of chiral symmetry is observed. In the meson spectrum correlation functions of chiral partners become degenerate after some critical temperature T_c, and for ground state nucleons parity doubling is observed. In a specific domain around $2T_c$ an additional $\mathrm{SU}(4)$ symmetry naturally emerges in the spectrum of mesons, which was previously observed in numerical experiments, where chiral symmetry was artificially restored. The implications of this $\mathrm{SU}(4)$ symmetry on the gluonic degrees of freedom in the high temperature phase are discussed.

Furthermore, the previously established method to artificially restore chiral symmetry by removing the low-mode spectrum of valence quark propagators is applied to a quenched simulation of chiral fermions for multiple quark masses. The effects of the truncation on $J = 1$ mesons are studied in dependence of different pion masses.

Kurzfassung

Die Effekte der Quantenchromodynamik (QCD) bei hohen Temperaturen sind aktuell Gegenstand von theoretischem und experimentellem Interesse. Mithilfe großer Teilchenbeschleuniger wird ein neuartiger Materiezustand erzeugt, der sich bedeutend von herkömmlicher hadronischer Materie im Vakuum unterscheidet. In dieser Arbeit werden Gitterfeldmethoden verwendet, um die Symmetrieeigenschaften von stark–wechselwirkender Materie bei hohen Temperaturen zu studieren. Dabei wird insbesondere die Restaurierung von Chiraler Symmetrie untersucht. Im Spektrum von Mesonen wird dies durch Entartung der Korrelationsfunktionen von Chiralen Partnern über einer kritischen Temperatur T_c beobachtet, und für Nukleonen im Grundzustand durch Entartung von Paritäts–Partnern. In einem speziellen Fenster um $2T_c$ manifestiert sich eine zusätzliche $\mathrm{SU}(4)$ Symmetrie, die zuvor in numerischen Experimenten mit künstlicher Wiederherstellung Chiraler Symmetrie beobachtet wurde. Implikationen der $\mathrm{SU}(4)$ Symmetrie auf die Freiheitsgrade von Gluonen bei hoher Temperatur werden diskutiert.

Weiters wird die zuvor erwähnte Methode zur künstlichen Wiederherstellung Chiraler Symmetrie auf eine ‘quenched’ Simulation mit chiralen Fermionen und mehreren Quarkmassen angewandt. Dies geschieht, indem niedrige Eigenmoden der Valenz–Quarkpropagatoren entfernt werden. Die Auswirkungen dieser Methode auf das Massenspektrum von $J = 1$ Mesonen werden für verschiedene Pionmassen studiert.

Contents

Chapter 1

Introduction

Hadrons act as if they where made up of quarks,
but the quarks don't have to be real.

— Murray Gell-Mann, *Lectures on Quarks*

The *Large Hadron Collider* at CERN underneath the border of France and Switzerland is generally considered to be the biggest machine build by man. When it started its operation in September 2008, its mission was clear: collide hadrons, probe the *Standard Model*, and discover new physics. A first milestone was achieved in 2012 with the discovery of the Higgs particle. Thereby the last missing piece of the Standard Model has been found, and its correctness and consistent description of nature been verified. While many efforts are nowadays directed towards finding new physics, unifying forces and explaining open cosmological questions commonly referred to as dark matter and dark energy, there is still a multitude of unresolved details within the Standard Model, which require for a better understanding.

Some particular notorious puzzles revolve around the strongly interacting, *i.e.* hadronic, part of nature, which is described by the theory of *Quantum Chromodynamics* (QCD) in the Standard Model. QCD is formulated as non-abelian gauge theory, whose $\mathrm{SU}(3)$ gauge group offers a rich mathematical structure, while at the same time renders it analytically inaccessible. The most prominent peculiarities of QCD are chiral symmetry breaking, the mass gap, asymptotic freedom, and confinement[1].

A bulk of evidence and understanding of chiral symmetry breaking effects in the low energy regime of the theory have been gathered so far for various approaches to QCD. Its manifestation and dynamics in the lattice approach to QCD will be covered in this thesis. The mass gap problem of Yang-Mills theories on the other hand is one of the seven Millenium Prize problems issued by the Clay Mathematics Institue and still an open question, the solution of which is rewarded with one million dollars. As such, it is naturally within the domain of mathematical physics, and the relative absence of experimental findings of gluonic states relieves the problem from the urgency to shed light on the mass gap problem.

The main part of this thesis however deals with phenomena generally associated with asymptotic freedom and confinement. Both effects are related by the specific way of how the coupling strength of QCD behaves at different energies, and which effects this has on the effective degrees of freedom. Extra care has to be taken when discussing these topics, as there are different definitions of confinement used in existing literature. Its interpretation is often impaired by imprecise terminology along with uncertainty on how to measure alleged *deconfinement* in experiment, which results in an overall ambiguous situation. In addition, the properties of confined hadrons change rapidly in a temperature range at which the transition of a chirally broken to a chirally symmetric regime takes place. Again, extra care is necessary to

[1] In analogy to the phenomenon of asymptotic freedom, confinement is sometimes refered to as *infrared slavery*. The relation of both terms and exact meaning of confinement are discussed later in this thesis.

distinguish the effects of both phenomena. To illustrate the conceptual difficulties, let us assume a basic definition of confinement as the property that all observable hadrons are color-neutral states. This in turn defines deconfinement as the possibility to observe color-charged states, *i.e.* free quarks. Now the quote in the epigram at the beginning of this chapter is taken from a lecture, which Murray Gell-Mann, a founding father of QCD, gave during the 11th Winter School in Schladming, Austria, in 1972. There he introduces quarks as building blocks of hadrons, with an additional property to distinguish quarks in the same state: color. Gell-Mann stressed out that quarks are a mathematical concept, a simple, childish model to describe the observed spectrum, and that quarks do not necessarily have to be real. The idea is mentioned that there may be no fundamental things at all. Here the naive definition of deconfinement given above runs into troubles.

In the infrared region of QCD, where momentum transfers are small and the coupling strong, the effective degrees of freedom are hadrons, as we measure them in nature. Under certain conditions of high temperature or high matter density this could change: conditions as they are expected at the beginning of the universe or as they are produced during heavy-ion collisions in experiments at the Large Hadron Collider (LHC) or the Relativistic Heavy Ion Collider (RHIC) of the Brookhaven National Laboratory in Upton, New York[2]. This heavy-ion collisions leave around 400 participating nucleons in a state of extremely high temperature for a fraction of a second, during which the traditional hadrons are expected to dissolve into lighter degrees of freedom. This experiments allow to probe confining properties of hadronic matter and thereby guide and verify the theoretical understanding.

Theoretical approaches to this questions of QCD are characterized by the fact that the infrared physics cannot be treated perturbatively due to the strong coupling in this domain. Therefore genuine non-perturbative methods have to be used. In this thesis the lattice approach to QCD will be applied. Lattice QCD is a well established method for extracting hadron properties in the vacuum, as well as scattering data and bulk properties of high temperature QCD. It is a priori not clear which role non-perturbative effects have in the high temperature region of QCD and at which temperature methods of perturbation theory become an eligible tool to accurately describe the physics, *i.e.* at which temperature an asymptotically free scenario is reached – if at all.

Non-perturbative effects of QCD are strongly connected to the low-lying eigenmodes of the Dirac operator and have been shown to include interesting physics: *e.g.* the relation of Banks–Casher links the chiral condensate to the near-zero modes, and the index theorem of Atiyah–Singer directly connects topology and zero modes. Topological excitations can be interpreted as instantons, which, inter alia, effectively describe the physics related to the $\mathrm{U}(1)_A$ anomaly.

Now the use of lattice methods has a big virtue when addressing questions like this: working with a discretized version of space-time it becomes feasible to explicitly calculate eigenvalues of operators and explore the low-mode Dirac sector numerically. This has been done in a set of experiments, where low-lying fermion modes have been used to examine topological and chiral properties, as well as to construct hadron-like propagators [1–3]. In a similar set of numerical experiments [4–16] the 'inverse' has been done: modified hadron propagators have been constructed by excluding the low-lying modes of the Dirac operator. Thus chiral symmetry has been found to be *unbroken*, while most hadronic properties are kept intact. Moreover, an additional, dynamically emergent symmetry of the truncated spectrum has been observed and identified as $\mathrm{SU}(4)$ symmetry in this specific simulation. More details on this artifical trunaction scheme and its effects on the hadron spectrum will be discussed in section 4.1.

In the work at hand central elements and building blocks of observables are quark propagators, whose distribution of eigenmodes is strongly dependent on the temperature of the system: it has been shown that the low modes are strongly suppressed close to the chiral transition [17–20] . The question whether or not there is a gap opening in the eigenmode spectrum, is still subject of current research. Along with the theoretical and numerical considerations above, this situation gives additional motivation to study

[2]Whereas the operation of RHIC is specifically dedicated towards heavy-ion collisions, the LHC operates with heavy-ions just for a few weeks during a year, usually at the end of each proton-proton run.

QCD at high temperature and induces expectations of changing physics in the hadronic spectrum.

The main body of this thesis will cover correlation functions of mesons and baryons in the high temperature phase of two flavor QCD. By carefully studying appropriate operators, it is thus possible to study the long–range effects of chiral symmetry restoration in the spectrum of QCD, in contrast to directly measuring susceptibilities. A close look at the effects of the $\mathrm{U}(1)_A$ anomaly on the spectrum is possible, and its effective restoration in dependence of the quark mass and temperature will be tracked. Finally, properties of the previously mentioned $\mathrm{SU}(4)$ symmetry will be investigated. While in previous studies this symmetry was found by artificially removing parts of QCD, here it emerges naturally in a specific domain of the high temperature spectrum. This observation, its implications and consequences on the effective degrees of freedom will be discussed.

To summarize the introduction, a few more open questions of general nature can be stated, which are related to the non-perturbative physics of QCD:

- What is the mechanism of mass generation in hadrons?
- Is chiral symmetry related to confinement?
- Is there deconfinement?
- Are there hadrons in a chirally symmetric regime?
- What are the effective degrees of freedom there?
- What about quarkyonic matter?

Using modern lattice methods we are in a situation where we can give an answer to some of this questions, from a stochastic point of view, and hope that our findings may help in the general understanding of nature.

At last a short word on the structure of this thesis: the aim is to present published and unpublished results of scientific research in a broader context. Generally a greater physical picture is discussed, and to increase the accessibility for non-experts, important technical details, their advantages and shortcomings are mentioned. Therefore the thesis is structured as follows:

Chapter 2 introduces some basic concepts of QCD. As established theory to describe the strong interaction, it is the subject on which we want to increase our knowledge by theoretical and experimental means. Some relevant aspects on QCD in the vacuum and at high temperature are mentioned, and an overview of the experimentally and theoretically estabilshed facts is given. Lastly, a brief introduction to the lattice regularization of QCD is given. Everything presented here is well established and can be found in any standard textbook on field theory. We will follow the presentations in [21–24] and [25, 26] for the parts on lattice theory.

Chapter 3 reviews chiral symmetry. Starting from a general field theoretical point of view, the exact realization in the spectrum of QCD is explained, the different ways it can be broken, as well as the theoretical expectations for a high temperature phase and its relation to the low-lying eigenmodes of the Dirac operator. Finally, a classification of hadronic operators according to multiplets of the chiral-parity group will be given.

In Chapter 4 first original results are presented. A quenched simulation using Overlap fermions is presented, on which a low-mode truncation of the Dirac operator is performed. This procedure has previoulsy been applied in literature, the results of which we are able to reproduce. In addition to previous results, we present the quark mass dependence of the applied truncation scheme. Next, we discuss lattice QCD in the vacuum by a dynamical simulation using Domain-Wall fermions. This will introduce and discuss the simulation setup for the high temperature study.

Chapter 5 presents a high temperature study, which contains the main results of this thesis. A dynamical simulation applying $n_f = 2$ Domain-Wall fermions is used to probe the hadronic spectrum in a high temperature phase of QCD above the chiral transition. The presented data will cover a temperature range of $2.2T_c - 5.5T_c$.

Chapter 6 analyzes the symmetry properties and emergent phenomena of the previously attained results. We will discuss the effective restoration of $\mathrm{U}(1)_A$ symmetry, as well as chiral symmetry restoration.

Furthermore, an emergent symmetry is identified as chiralspin symmetry, which has previously been conjectured to appear in the high temperature phase of QCD. Including chiral symmetry, a $\mathrm{SU}(2n_f)$ symmetry of the hadronic spectrum can be formulated.

Chapter 7 concludes the findings. The implications of a $\mathrm{SU}(4)$ symmetry and possible applications are discussed, as well as experimental consequences.

The Appendices contain conventions and bits of work, which did not fit into the main body of this thesis, but stem from related projects. This includes work concerning the angular momentum content of low-lying mesons, some ideas on exotic mesons and further unpublished results of the low-mode removal procedure.

Parts of this thesis have already been presented to the scientific community during following international meetings, the proceedings are referred to at the corresponding sections:

- 54th Schladming Winter School of Theoretical Physics
  New Trends in Particle Physics, Quantum Gravity & Cosmology
  Schladming (Austria), February 21–26, 2016
- Mini-Workshop Bled 2016
  Quarks, Hadrons, Matter
  Bled (Slovenia), July 3–10, 2016
- 34th International Symposium on Lattice Field Theory
  University of Southampton (UK), July 24–30, 2016
- 35th International Symposium on Lattice Field Theory
  Granada (Spain), June 18–24, 2017
- 27th International Conference on Ultra-relativistic Nucleus-Nucleus Collisions
  Venezia (Italy), May 13–19, 2018
- 36th International Symposium on Lattice Field Theory
  East Lansing, MI (USA), July 22–28, 2018
- 679th WE-Heraeus-Seminar
  Quantum Chromodynamics and Its Symmetries
  Oberwölz (Austria), September 9–15, 2018

Chapter 2

Quarks, Quantum Chromodynamics and the phase diagram

It is of course important to try to maintain consistency,
but when this effort forces you into a stupendously ugly theory,
you know something is wrong.

— Douglas R. Hofstadter, *Gödel, Escher, Bach*

The role of aesthetics in science might be debatable, but certainly some concepts in fundamental physics carry intrinsic beauty[1] due to their commitment to minimalism. The concept of gauge theories is an example, where minimal assumptions on top of an existing theory lead to great insights. Quantum Electrodynamics (QED) is a working prototype, which reduces the many manifestations of electrodynamics and magnetism in nature to the simplistic set of requirements of a $\mathrm{U}(1)$ gauge theory. The fact that QED is not only a possible model of, but an extremely accurate quantitative description of electromagnetism, reserved gauge theories a prominent place in the toolbox of theoretical physics.

In the 1970's it became clear that also the strong nuclear force can be described as gauge theory, underlying the $\mathrm{SU}(3)$ gauge group and building on the quark model. The resulting theory is QCD [27]. The common origin of QED and QCD also means common terminology, in parts for different phenomena.

Later on it will be important to have a precise description of things; therefore, and to illustrate the concept of a gauge theory, first a brief sketch of the construction of QED is given. Afterwards the basics of QCD are introduced and the concepts of running coupling and asymptotic freedom are discussed. Then an overview of the quark model is given, and how it can be used to structure the multitude of experimentally observed particles. The chapter continues with a short discussion of the phase diagram of QCD and the experimental situation. Finally a short portrait of our method of choice, lattice QCD, will be given.

2.1 Blueprint of a gauge theory

The discussion of gauge theories usually starts with the Lorentz-invariant lagrangian density for non-interacting fermions

$$\mathcal{L} = \bar{\Psi} i\gamma^\mu \partial_\mu \Psi - m\bar{\Psi}\Psi, \tag{1}$$

where $\Psi(x)$ is the matter field for one kind of fermions at space time point x and $\bar{\Psi}(x) \equiv \Psi(x)^\dagger\gamma^0$ its conjugate. This generalizes trivially to k different kinds of fermions Ψ_k with masses m_k. Using the

[1] For completeness the Latin maxim *De gustibus et coloribus non est disputandum* is mentioned.

classical equations of motion for the conjugate field $\bar{\Psi}$

$$\partial_\mu \frac{\partial \mathcal{L}}{\partial(\partial_\mu \bar{\Psi})} - \frac{\partial \mathcal{L}}{\partial \bar{\Psi}} = 0 \tag{2}$$

the Dirac equation[2]

$$(i\gamma^\mu \partial_\mu - m)\Psi(x) = 0 \tag{3}$$

is obtained. It describes the relativistic propagation of fermions without any interaction. Now enforcing $\mathrm{U}(1)$ gauge invariance means that the theory should not change under local $\mathrm{U}(1)$ transformations of the fermion field

$$\Psi'(x) = \exp[-\mathrm{i}\Theta(x)]\Psi(x) \tag{4}$$

with some local rotation parameter $\Theta(x)$. This means one should be allowed to change the complex phase of the fermion field at any space time point without changing the theory. Applying transformation (4) to the fields in (1) it becomes clear that this is not the case, as the derivative depends on different space time points. Changing them separately would render the derivative meaningless, introduce extra terms and violate the requirement for gauge invariance. By introducing a vector field $A_\mu(x)$ with transformation properties

$$A'_\mu(x) = A_\mu(x) + \frac{1}{e}\partial_\mu \Theta(x) \tag{5}$$

an operator

$$D_\mu = \partial_\mu + \mathrm{i}eA_\mu(x) \tag{6}$$

can be defined, which is usually called *covariant* derivative. Using the covariant derivative in (1) results in

$$\mathcal{L} = \bar{\Psi} i\gamma^\mu D_\mu \Psi - m\bar{\Psi}\Psi, \tag{7}$$

which is invariant under transformations (4) and thus the requirement of $\mathrm{U}(1)$ gauge invariance is fulfilled. The equation of motion for (7) is

$$(i\gamma^\mu D_\mu - m)\Psi(x) = 0. \tag{8}$$

The introduction of $A_\mu(x)$ means additional degrees of freedom, for the $\mathrm{U}(1)$ gauge theory of QED the field quanta are identified as photons. One can include a kinetic term for photons by looking for a gauge and Lorentz invariant quadratic term including $A_\mu(x)$. The antisymmetric product of two covariant derivatives $[D_\mu, D_\nu]\Psi$ yields an object called *field strength tensor*

$$F_{\mu\nu}(x) = \partial_\mu A_\nu(x) - \partial_\nu A_\mu(x), \tag{9}$$

which upon multiplication with itself gives the desired object $F^2_{\mu\nu}$. Adding this term to (7) gives the full lagrangian density of a $\mathrm{U}(1)$ gauge theory

$$\mathcal{L} = \bar{\Psi} i\gamma^\mu D_\mu \Psi - m\bar{\Psi}\Psi - \frac{1}{4}F^2_{\mu\nu}. \tag{10}$$

Now since the lagrangian density is invariant under a local $U(1)$ transformation, also Noether's theorem should apply. To illustrate its workings, a brief sketch of its derivation is given. Lets assume the

[2] Unless stated otherwise, the conventions given in appendix A are used.

variation of some general lagrangian density:

$$\begin{aligned}\delta\mathcal{L} &= \frac{\partial\mathcal{L}}{\partial\Phi}\delta\Phi + \frac{\partial\mathcal{L}}{\partial(\partial_\mu\Phi)}\delta(\partial_\mu\Phi) \\ &= \frac{\partial\mathcal{L}}{\partial\Phi}\delta\Phi + \frac{\partial\mathcal{L}}{\partial(\partial_\mu\Phi)}\partial_\mu\delta\Phi \\ &= \frac{\partial\mathcal{L}}{\partial\Phi}\delta\Phi + \partial_\mu\left[\frac{\partial\mathcal{L}}{\partial(\partial_\mu\Phi)}\delta\Phi\right] - \partial_\mu\frac{\partial\mathcal{L}}{\partial(\partial_\mu\Phi)}\delta\Phi\end{aligned} \tag{11}$$

In the last line of (11) the first and third term vanish due to the equations of motion (2), what leaves

$$\partial_\mu\left[\frac{\partial\mathcal{L}}{\partial(\partial_\mu\Phi)}\delta\Phi\right] = \delta\mathcal{L}. \tag{12}$$

Assuming that the variation of the lagrangian density, *i.e.* the effects of the $\mathrm{U}(1)$ gauge transformations, vanishes $\delta\mathcal{L} = 0$ and identifying the term in the square brackets of (12) as a current

$$j_\mu(x) = \frac{\partial\mathcal{L}}{\partial(\partial_\mu\Phi)}\delta\Phi, \tag{13}$$

the conservation law

$$\partial_\mu j^\mu(x) = 0 \tag{14}$$

is derived. A corresponding charge

$$Q = \int \mathrm{d}^3x j_0(x) \tag{15}$$

is also conserved. In the case of a $\mathrm{U}(1)$ gauge theory of electromagnetism, Q is of course the electric charge and the gauge theory naturally explains its conservation.

2.2 QCD as gauge theory

Given the success of QED, it is natural to apply the concept of a gauge theory to other forces of nature. For the strong interaction, which is responsible for binding nuclei together, this led to the developement of QCD. The choice of $\mathrm{SU}(3)$ as gauge group has a few well justified motives, but most prominently probably is the historical 'Delta' argument: The quark model, which is discussed in section 2.3, works quite well in explaining the hadron spectrum in terms of its constituents, quarks. But for the Δ^{++} particle there is a problem: It is composed of 3 up quarks with their spins aligned. The flavor wave function is symmetric, the spin wave function is symmetric, but the particle itself is a fermion, should obey Fermi statistics and thus feature an anti symmetric wave function. A remedy for this situation is to introduce an additional quantum number, *color*, which anti symmetrizes the wave function of the Δ^{++} and saves the quark model. The smallest group offering all requirements for such a color symmetry group is $\mathrm{SU}(3)$. Hence a possible candidate for a gauge symmetry group describing strong interactions has been found. As it has been verified throughout the last 4 decades, this is a good choice.

In analogy to (4) a starting point to derive a few aspects of QCD is to demand invariance of free fermions under continuous transformations of the gauge group, $\mathrm{SU}(3)$,

$$\Psi'(x) = \exp[-\mathrm{i}\Theta^a(x)T^a]\Psi(x). \tag{16}$$

Here the first and most striking difference between QED and QCD can be seen: transformations of $\mathrm{SU}(3)$ as non-abelian group are constructed by non-trivial generators T^a, where a runs from 1 to the number of generators of the group, which is 8 in the case of $\mathrm{SU}(3)$. As generators conventionally the 8 Gell-Mann

matrices $T^a = \lambda^a/2$ are used.

Following the blueprint of a gauge theory, a covariant derivative is constructed by

$$D_\mu = \partial_\mu + A_\mu(x), \quad A_\mu = -\mathrm{i}gA^a_\mu(x)T^a. \tag{17}$$

For QCD also 8 vector fields A^a_μ as gauge particles, called *gluons*, are required. They transform according to

$$A^{a\prime}_\mu(x) = A^a_\mu(x) - \frac{1}{g}\partial_\mu\Theta^a(x) + f^{abc}\Theta^b(x)A^c_\mu(x), \tag{18}$$

with f^{abc} the structure constant of $\mathrm{SU}(3)$. This can be written in the fundamental representation as

$$A'_\mu(x) = A_\mu(x) - \partial_\mu\Theta(x) + [\Theta(x), A_\mu(x)]. \tag{19}$$

In analogy to (9) a field strength tensor $G_{\mu\nu}$ can be constructed

$$G_{\mu\nu}(x) = \partial_\mu A_\nu(x) - \partial_\nu A_\mu(x) + [A_\mu(x), A_\nu(x)], \tag{20}$$

which in terms of group generators gives

$$G_{\mu\nu}(x) = -igG^a_{\mu\nu}T^a, \tag{21}$$

$$G^a_{\mu\nu}(x) = \partial_\mu A_\nu(x) - \partial_\nu A_\mu(x) + [A_\mu(x), A_\nu(x)]. \tag{22}$$

Now the full lagrangian density for QCD can be assembled:

$$\mathcal{L} = \bar{\Psi}i\gamma^\mu D_\mu\Psi - m\bar{\Psi}\Psi + \frac{1}{2g^2}\mathrm{Tr}\left[G_{\mu\nu}G^{\mu\nu}\right]. \tag{23}$$

The commutator in the expression for the field strengh (22) is required for gauge invariance and a direct consequence of the non-abelian nature of $\mathrm{SU}(3)$. In the quadratic term of the lagrangian density the commutator $[A_\mu(x), A_\nu(x)]$ gives rise to gluonic self interaction. This in turn is responsible for some remarkable differences between QCD and QED, and the mathematical complexity of non-abelian gauge theories in general.

One characteristic of describing nature through gauge theories is the highly non-trivial prediction that the vacuum state is not just the state of lowest energy, but becomes a medium itself with a complex structure. Making use of uncertainty and the equivalence of energy and matter, a picture of permanently emerging and annihilating particles in an otherwise empty space can be thought of, so-called *vacuum fluctuations*. Placing an actual particle with some charge into a vacuum state, these virtual particles are allowed to interact with the charge, *i.e.* the vacuum can be polarized. By that, in the vacuum medium the effective charge of the particle and ability to interact is altered, depending on the scale at which the charge is probed. Both theories, QED and QCD, share this effect, known as *running coupling*. The exact way of how this running coupling behaves depends on the gauge group and number of fermions, and is encoded in the β function of a theory.

The β function of QED reads

$$\beta(e) = \frac{e^3}{12\pi^2} + \mathcal{O}(e^5), \tag{24}$$

where e is the electric charge. Due to the positivity of the leading contribution in (24) one speaks of a positive β function and the electric charge being *screened*. The running coupling constant $\alpha = e^2/4\pi$ now depends on the momentum scale Q and its leading contribution is given by

$$\alpha(Q^2) = \frac{\alpha}{1 - (\alpha/3\pi)\log(Q^2/M^2)}. \tag{25}$$

In the infrared region of QED, at low momenta and large distances, α is the well-known fine-structure constant $1/137$. For larger energies also α increases until, theoretically, an ultraviolet divergence is reached, the *Landau pole*. Practically, perturbation theory used for calculating the running coupling is no longer applicable in this regime and the exact behaviour of the β function is unknown.

The β function for a general $\mathrm{SU}(N)$ gauge theory is given by

$$\beta(g) = -\frac{g^3}{(4\pi)^2}\left(\frac{11}{3}N - \frac{2}{3}n_f\right) + \mathcal{O}(g^5), \tag{26}$$

which results in

$$g^2(Q^2) = \frac{g^2}{1 + \frac{g^2}{(4\pi)^2}\left(\frac{11}{3}N - \frac{2}{3}n_f\right)\log(Q^2/M^2)} \tag{27}$$

for the coupling parameter. For QCD with $\mathrm{SU}(3)$ as gauge group the leading term of the β function is

$$\beta(g) = -\frac{b_0 g^3}{(4\pi)^2}, \quad b_0 = 11 - \frac{2}{3}n_f. \tag{28}$$

Introducing α_s as coupling for the strong force $\alpha_s = g^2/4\pi$ the running coupling for QCD can be written as

$$\alpha_s(Q^2) = \frac{\alpha_s}{1 + (b_0\alpha_s/4\pi)\log(Q^2/M^2)}. \tag{29}$$

A negative β function (28) for QCD leads to color *anti*-screening. This in turn is responsible for asymptotic freedom, *i.e.* vanishing coupling α_s for large momenta $Q \to \infty$. These considerations are true as long as coefficient b_0 stays positive, *i.e.* for a maximum number of $n_f = 16$ quark flavors[3]. After introducing a cutoff scale

$$1 = g^2(b_0/8\pi^2)\log(M^2/\Lambda^2) \tag{30}$$

and thus trading a dimensionless coupling constant g in the lagrangian density with a dimensionful parameter Λ, a simplified expression for the running coupling is obtained:

$$\alpha_s(Q) = \frac{2\pi}{b_0\log(Q^2/\Lambda^2)}. \tag{31}$$

Experiments suggest a typical mass scale of $\Lambda \approx 200$ MeV for QCD, and perturbation theory becomes a valid description of physical processes for $Q > 1$ GeV. This is the case *e.g.* for deep inelastic scattering experiments, where Q typically is of the order of 30 GeV.

2.3 The quark model

The quark model is a way to classify the observed spectrum of baryons and mesons in terms of more fundamental constituents – quarks of different flavors. It was proposed by Murray Gell-Mann [28] and, independently, by George Zweig [29, 30]. It was originally formulated for the lightest 3 quarks and arranges the hadrons into multiplest of an approximate $\mathrm{SU}(3)$ flavor symmetry. 3 more quarks have been found since then, each being heavier than the previous. All quarks, which are known today, and their flavor quantum numbers are given in table 2.1. It can be seen that their masses cover 5 orders of magnitude: the *up* quarks are just a few times the electron weight, whereas the *top* quarks are almost as heavy as gold atoms.

The quark model describes hadrons as bound states of quarks. Baryons[4] are according to the quark

[3] Given the 6 known quark flavors, their mass hierarchy and the absence of experimental evidences for more, the assumption that $n_f < 17$ is quite reasonable.

[4] 'Baryon' derives from the greek word for 'heavy'. Baryons are heavy particles in contrast to leptons, 'light' particles.

quark		charge	flavor	mass
up	u	$+\frac{2}{3}$	$I_z = +\frac{1}{2}$	2.2 MeV
down	d	$-\frac{1}{3}$	$I_z = -\frac{1}{2}$	4.7 MeV
strange	s	$-\frac{1}{3}$	$S = -1$	95 MeV
charm	c	$+\frac{2}{3}$	$C = +1$	1.275 GeV
bottom	b	$-\frac{1}{3}$	$B = -1$	4.18 GeV
top	t	$+\frac{2}{3}$	$T = +1$	173.0 GeV

TABLE 2.1: Quantum numbers of quarks. Estimates of masses are taken from [31], for methodology of determination and uncertainties see therein. The flavor quantum numbers are isospin, strangeness, charm, bottomness and topness, respectively.

ℓ	s	J^{PC}
0	0	0^{-+}
0	1	1^{--}
1	0	1^{+-}
1	1	0^{++}
1	1	1^{++}
1	1	2^{++}

TABLE 2.2: Possible combinations of orbital angular momentum and spin.

model composite particles, which contain 3 quarks. Each quark is assigned a baryon number of $\frac{1}{3}$ by the quark model. The composite baryon thus has a baryon number 1. In constrast, mesons[5] are composed of a quark and an anti quark. Due to the baryon number of $-\frac{1}{3}$ for an anti quark, their baryon numbers add up to 0.

In the light of classical, non-relativistic bound states, mesons of the quark model can be assigned quantum numbers based on angular momenta of its constituents:

- the total spin s of a meson can either be 0 or 1, depending on the parallel or anti parallel alignment of its quark spins,
- there can be orbital angular momenta ℓ between the quarks,
- the meson spin J then takes values $|\ell - s| \leq J \leq |\ell + s|$ according to standard addition of angular momenta,
- and parity P and charge parity C can be deduced by $P = (-1)^{\ell+1}$ and $C = (-1)^{\ell+s}$.

A few combinations of possible mesonic J^{PC} states are given in table 2.2. Based on this considerations, there are a few J^{PC} states, which are naturally forbidden by the quark model – so-called *exotic* states:

$$0^{+-}, 1^{-+}, 2^{+-}, \ etc \tag{32}$$

The observed meson spectrum can be structured according to the partial wave classification of $n^{2s+1}\ell_J$ states, where n is the principal quantum number for radial excitation. While this description is useful for mesons including heavier quarks, where a non-relativistic description can somewhat be justified, its validity for light mesons is limited and disputed. An example for this ambiguous description would be the $\rho(1450)$, which is discussed in appendix B.

[5] The name 'meson' derives form the greek word for 'middle', as this particles are 'middle' heavy.

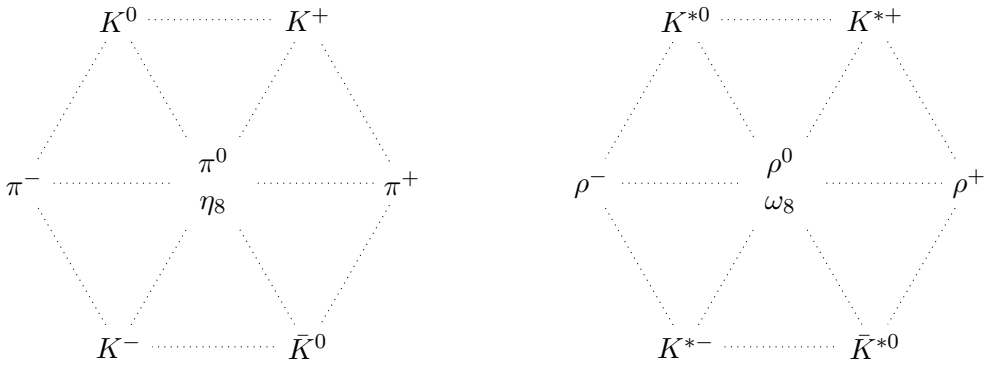

FIGURE 2.1: Octets of spin $J = 0$ mesons (*left side*) and spin $J = 1$ mesons (*right side*) according to the eightfold way. The horizontal and vertical alignment is according to the flavor quantum numbers isospin I_z and strangeness S respectively. The electric charge is conserved along diagonal lines and denoted as superscript.

Now the *Eightfold Way* assumes the lightest 3 quark flavors u, d and y to be mass degenerate and $\mathrm{SU}(3)$ to be an approximate flavor symmetry of the hadronic spectrum. This way mesons can be grouped into following multiplets[6]:

$$\mathbf{3} \otimes \bar{\mathbf{3}} = \mathbf{8} \oplus \mathbf{1}, \tag{33}$$

an octet and a singlet. For $J = 0$ mesons, the octet is depicted on the left side of figure 2.1, the corresponding singlet is the η_1 meson. More on the η mesons and their role in the spectrum will be discussed in section 3.2. The right side of Figure 2.1 shows the meson octet for $J = 1$ mesons, the corresponding singlet is the ω_1. The mesons with zero flavor quantum numbers appearing in the physical spectrum are superpositions of the corresponding octet and singlet states of the $\mathrm{SU}(3)$ multiplets. For baryons a similar decomposition can be done,

$$\mathbf{3} \otimes \mathbf{3} \otimes \mathbf{3} = \mathbf{10}_S \oplus \mathbf{8}_M \oplus \mathbf{8}_M \oplus \mathbf{1}_A. \tag{34}$$

The resulting multiplets now have different symmetry properties under exchange of single quarks: symmetric, mixed and antisymmetric, as indicated by the subscript. To disentangle these states it is useful to consider the structure of a hypothetical baryonic wave function:

$$|qqq\rangle_A = |\mathrm{color}\rangle_A \times |\mathrm{space, spin, flavor}\rangle_S \tag{35}$$

For ground state baryons without orbital angular momenta between its constituents, a symmetric space wave function is assumed. Focusing on spin and flavor of baryons, a flavor–spin $\mathrm{SU}(6)$ group can be constructed by taking all 6 combinations of spin and flavor as basis states. A decomposition of composite $\mathrm{SU}(6)$ states into multiplets gives

$$\mathbf{6} \otimes \mathbf{6} \otimes \mathbf{6} = \mathbf{56}_S \oplus \mathbf{70}_M \oplus \mathbf{70}_M \oplus \mathbf{20}_A, \tag{36}$$

where *e.g.* the symmetric $\mathbf{56}$-plet is made up of the flavor multiplets

$$\mathbf{10} \oplus \mathbf{10} \oplus \mathbf{10} \oplus \mathbf{10} \oplus \mathbf{8} \oplus \mathbf{8}. \tag{37}$$

The four decuplets are nothing else than one $J = 3/2$ decuplet, and the two octets are one $J = 1/2$ octet. The particle identification for octet and decuplet are given in figures 2.2 and 2.3. The familiar nucleons proton P and neutron N, which will be of interest later on, are members of the $J = 1/2$

[6] Boldface numbers represent the multiplicity of a multiplet.

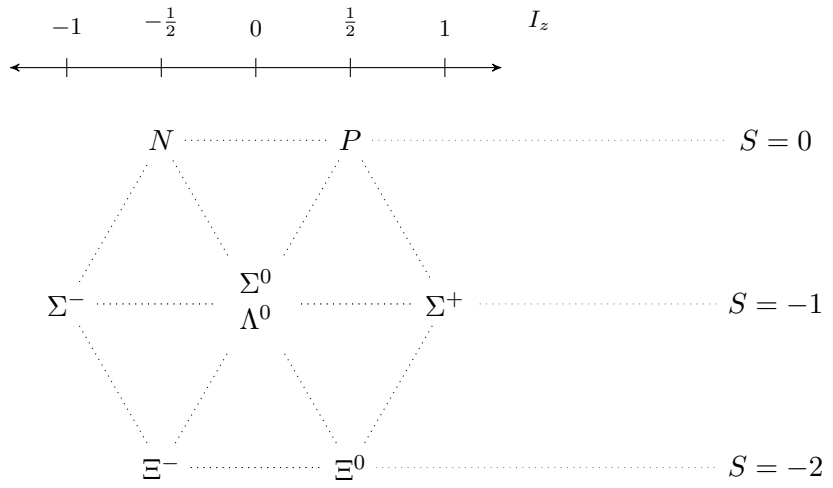

FIGURE 2.2: Octet of spin $J = \frac{1}{2}$ baryons according to the eightfold way. In the first line at zero strangeness the familiar nucleons are found as bound states of *up* and *down* quarks.

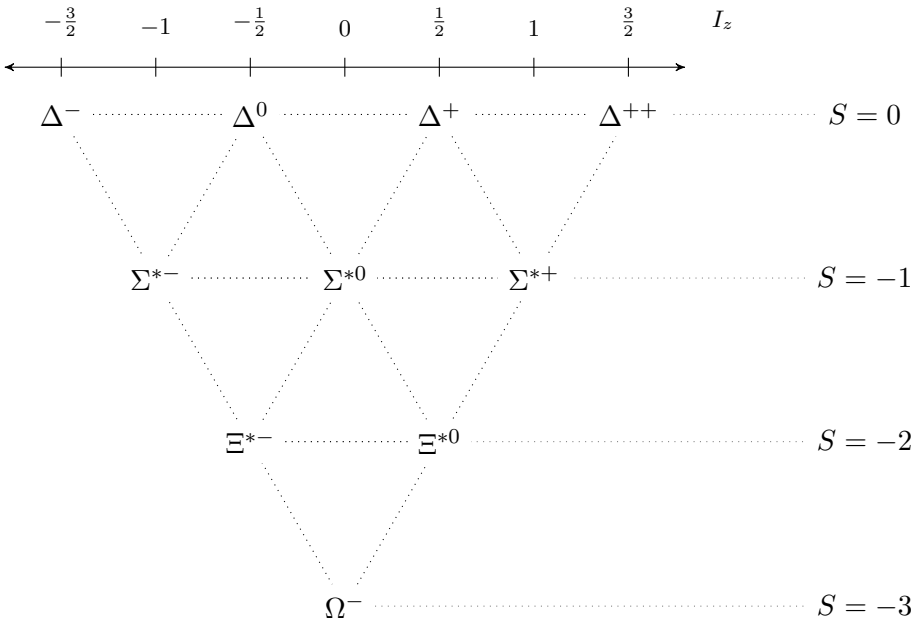

FIGURE 2.3: Decuplet of spin $J = \frac{3}{2}$ baryons according to the eightfold way. The Δ^0 and Δ^+ have the same flavor content as the neutron N and proton P and can be seen as their spin excitation. The Ω^- particle in the last line was predicted by the Eightfold Way and experimentally confirmed the first time in a bubble chamber experiment at BNL in 1964 [32].

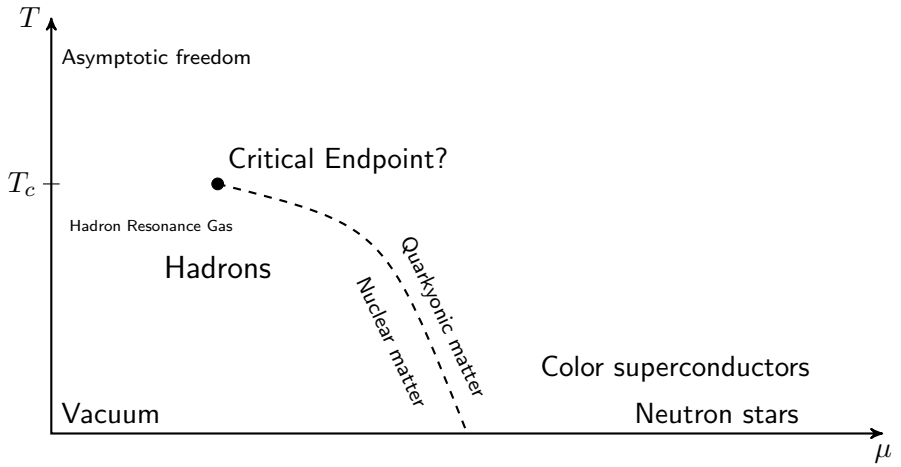

FIGURE 2.4: Conjectured phase diagram of QCD depending on temperature T and the baryon chemical potential μ. In the lower left corner is the vacuum state and regular hadrons. In this domain the chiral condensate breaks chiral symmetry spontaneously. T_c marks the critical temperature, after which the chiral condensate vanishes. The dashed line marks a possible phase transition with a critical endpoint. Regions of high density are expected inside of neutron stars, with a possible phenomenon of color superconducters.

multiplet with zero strangeness. Their spin excitations, the Δ^+ and Δ^0 respectively, are members of the $J = 3/2$ multiplet.

The development of QCD a few years later did not replace the quark model, but builds upon it and extends it by gluons as mediators of the strong force. In principle QCD also allows for exotic states containing 4 and 5 quarks – tetra and penta quarks, respectively – as well as pure gluonic states – called glueballs – and hybrid mesons. These states are allowed to have exotic quantum numbers (32), which cannot be constructed by the naive quark model. More on such states, and why they could be of interest, can be found in appendix C.

2.4 The phase diagram of QCD

2.4.1 Theoretical considerations

In the vacuum, at zero temperature and density, the strong interaction is well described by QCD. Perturbation theory is used to describe hadron collisions, where momenta are high and the coupling is weak, and describes the decay of heavy resonances into lighter particles which cannot decay any more under the strong interaction. On the other hand, properties of QCD bound states have to be calculated by non-perturbative means as the coupling is too strong for low momenta transfers, the *infrared* region of the theory. Detailed predictions have been made so far by *e.g.* lattice QCD. Concerning vacuum properties of QCD, current resereach focuses on precision measurements and description of scattering processes.

A different aspect of QCD, where general understanding is a lot less advanced, are the properties of strongly interacting matter at high temperatures and non-vanishing densities, *i.e.* QCD thermodynamics. Naive expectations, mostly based on the concept of asymptotic freedom presented in section 2.2, conjecture a new phase of matter for quarks interacting through QCD after some temperature, a *quark-gluon plasma* (QGP). While it is certain that properties of quarks change significantly with increasing temperature, the exact nature of this 'new phase' is still an open question. A sketch of the QCD phase diagram with some theoretical ideas is shown in figure 2.4.

A few limited properties of the phase diagram have been established so far. Most notably is the nature

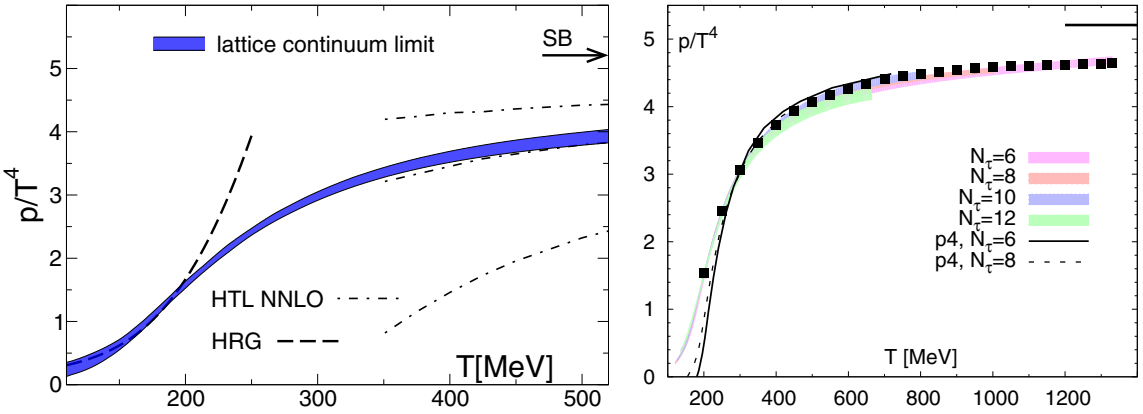

FIGURE 2.5: The pressure for QCD matter calculated by two lattice collaborations (Wuppertal-Budapest [35] on the *left*, HotQCD [36] on the *right* side). The solid lines on the upper right corners represent the Stefan-Boltzmann limit of an ideal gas.

of the chiral transition of QCD: by studying the finite size scaling of the chiral susceptibility it has been found that there is a crossover at some temperature T_c [33]. Further this temperature was calculated in [34] to be

$$T_c = 154 \pm 9\text{MeV}. \tag{38}$$

Since on the lattice it is possible to calculate the partition function exactly – within the systematic errors of the lattice approximation – other thermodynamical observables can be extracted. Two recent results for the pressure p are presented in figure 2.5. It can be seen that shortly after T_c the pressure p (and energy density ϵ, not shown here) rise sharply, which is consistent with a picture where 'liberation of degrees of freedom' is happening. This means that hadrons, which are the effective degrees of freedom in the vacuum and low temperature phase, *i.e.* below T_c, do not accurately describe the physical processes anymore. Accordingly, results for the *hadron resonance gas* model (HRG), which gives a pure kinematic description of thermodynamics in terms of hadrons, start to deviate from lattice results. Thus there is sound theoretical evidence that hadronic bound states start to melt after T_c and should be replaced by new, lighter effective degrees of freedom.

It is tempting to identify this new effective degrees of freedom directly with *deconfined* quarks and gluons. But this picture itself runs into problems: It is a priori not clear at which temperatures the effects of asymptotic freedom become manifest and QCD becomes neglectable. In figure 2.5 the Stefan-Boltzmann limit for the pressure of an ideal gas is given, and the QCD data is still far off at temperatures of $T \approx 1200$ MeV.

2.4.2 Experiments

Of course the experimental verification is an integral part of science and guiding principle of theoretical efforts. Measuring the phase diagram of QCD is moreover an important impulse in the development of current and future experimental facilities. Currently heavy ion collision with significant impact on the understanding of strongly interacting matter at high temperatures have been performed and measured at RHIC and LHC, some characteristic parameters are listed in table 2.3. Future facilities focusing on probing the phase diagram of QCD are the Facility for Antiproton and Ion Research (FAIR) of GSI in Darmstadt, Germany, and the Nuclotron-based Ion Collider fAcility (NICA) of the Joint Institute for Nuclear Research in Dubna, Russia.

Generally the stages of an 'event', *i.e.* the collision of two heavy ions, and the evolution of their product, a 'fireball' can be sketched as follows:

	RHIC	LHC
atoms	Au	Pb
# of nuclei	197	208
$\sqrt{s_{NN}}$	~ 200 GeV	~ 5 TeV
fireball volume	2500fm^3	5000fm^3
fireball lifetime	7fm/c	10fm/c

TABLE 2.3: A few experimental parameters of the two largest colliders probing the phase diagram of QCD. $\sqrt{s_{NN}}$ refers to the center of mass energy per nucleon pair, and 'fireball' is the hot QCD matter after collision.

1. A local equilibrium of strongly interacting matter is reached $0.5 - 1$ fm/c after the collision of the initial ions.

2. The system is now thermalized, has pressure and acts against the surrounding vacuum. The fireball expands.

3. The hot and stronly interacting matter starts to form hadrons. Due to frequent collision and interaction hadrons and their composition still can change.

4. Next, during chemical freeze-out, the final composition of hadrons is determined. This means the flavor content and abundances of hadrons is fixed.

5. During the kinematic freeze-out the thermodynamical description breaks down and the momentum distribution of the final hadrons is determined approximately 10 fm/c after the initial collision.

The timescale of $\sim 10^{-23}$ seconds is enough time for the strong interaction to thermalize, but too short for electroweak processes to take place[7]. Thus electroweak processes can safely be neglected in heavy ion collisions.

Given the short time, small space and abiguity of the state of matter one tries to measure, finding appropriate observables to identify properties of the fireball, some 'new kind of matter', is hard. Possible signatures of a QGP state have been discussed in literatur, most promising are J/Ψ suppression [37], strangeness production [38] and jet quenching [39]. Results of the first runs at RHIC and LHC suggest the elliptic flow of this new kind of matter to be a significant observable [40–42], and the accuracy of a hydrodynamical description of hot, strongly interacting matter seems established. Observables which could hint a proper phase transition and a possible critical endpoint are fluctuations of conserved quantities, *i.e.* electric charge or flavor quantum numbers [43]. None of this flucuations have been observed so far, however there are plans to improve on the quality of these observations at RHIC [44].

Current results of heavy ion collisions at RHIC and LHC and the questions, which they leave open, can be summarized:[8]

- Hydrodynamical description works very well
- What are the underlying dynamics?
- What are the relevant degrees of freedom?
- They are not free quarks and gluons.
- Thermodynamical quantities are below the Stefan-Boltzmann limit.
- The interaction is strong (as required by the hydrodynamical description).
- Effective degrees of freedom are not massless: $\varepsilon \neq 3p$.

[7] This is in contrast to *e.g.* the core of neutron stars, where equilibrium for extremely long times is expected.
[8] Plenary talk by Grosse-Oetringhaus, Quark Matter conference 2018.

2.5 The lattice approach

In this section a few basic considerations of lattice field theory are presented. First the general discretization scheme is discussed, and in subsection 2.5.2 some ideas on color confinement on the lattice are repeated. More details on spectroscopy, scale setting, thermodynamics, *etc.* are discussed along the way in the subsequent chapters.

2.5.1 Discretization

The lattice approach to QCD builds upon the Euclidean path integral formulation of QCD. In the path integral formalism, the expectation value of an observable O is calculated using

$$\langle O \rangle = \frac{1}{Z} \int \mathcal{D}[C] e^{-S_E[C]} O[C], \tag{39}$$

with the partition function $Z = \int \mathcal{D}[C] e^{-S_E[C]}$. The integral $\int \mathcal{D}[C]$ is a sum over all possible field configurations C, the term $S_E[C]$ is the Euclidean action for a given configuration, and the whole expression (39) a weighted sum with the factor

$$\exp(-S_E[C]) \tag{40}$$

as weight function. The path integral is defined in contiuous space time, thus there is an infinite amount of fundamental degrees of freedom, and the evaluation of the path integral (39) becomes hard.

Now the lattice approach[9] discretizes space time to make calculations actually feasible. This has a few implications on the theory and practical evaluation of (39). Firstly, the now discrete, but infinite sum over the configuration space Ω can be calculated by Monte Carlo integration. This is done by replacing the sum over Ω with a finite sum over a representative subset Ω':

$$\frac{1}{Z} \sum_{\Omega} e^{-S_E[C]} O[C] \quad \longrightarrow \quad \frac{1}{N} \sum_{\Omega'} O[C] \tag{41}$$

The configurations in Ω' should get selected according to the weight factor (40). Secondly, the degrees of freedom get mapped onto a finite hypercube. This way, the theory gets regularized in the infrared by a finite number of lattice points, and in the ultraviolet by a finite, non-vanishing distance a ('lattice spacing') between the lattice points. To ensure gauge invariance for any finite lattice spacing, the steps presented in sections 2.1 and 2.2 can be repeated with some slight modifications.

The following considerations assume a $\mathrm{SU}(3)$ gauge group in 4 dimensions, QCD. A discretized fermion field[10] is now represented by $\psi(x)$ with 3 color and 4 Dirac components each. Transformation properties of $\psi(x)$ under gauge transformations $g(x) \in \mathrm{SU}(3)$ are

$$\begin{aligned} \psi(x) &\to g(x)\psi(x) \\ \bar{\psi}(x) &\to \bar{\psi}(x) g(x)^\dagger, \end{aligned} \tag{42}$$

and thus local, as transformations itself depend on the position x in space time. In order to keep gauge invariance of products of fermions at different space time points, *gauge links* $U_\mu(x)$ with transformation properties

$$U_\mu(x) \to g(x) U_\mu(x) g^\dagger(x + \hat{\mu}) \tag{43}$$

are introduced. This way, *e.g.* quark bilinears $\bar{\psi}(x) U_\mu(x) \psi(x + \hat{\mu})$ are gauge invariant and gauge invariant, *i.e.* covariant, derivatives can be constructed. Conventionally, gauge links in backward direction are

[9] Which was introduced by Kennth G. Wilson [45] to investigate the confinement of quarks.

[10] We keep addressing the now discrete, integer-valued space time points by x, while some literature chooses n.

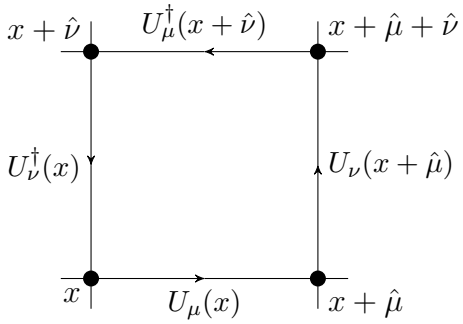

FIGURE 2.6: Graphical representation of a plaquette (46).

defined via

$$U_{-\mu}(x) = U_\mu^\dagger(x-\hat{\mu}), \tag{44}$$

and connect to the continuum gauge fields through

$$U_\mu(x) = \exp(\mathrm{i}aA_\mu(x)). \tag{45}$$

The expression (45) is nothing else than a linear approximation of a corresponding continuum gauge transporter. Of central importance in lattice theory is the shortest, closed and non-trivial gauge invariant loop of link variables, called *Plaqette*,

$$U_{\mu\nu}(x) = U_\mu(x)U_\nu(x+\hat{\mu})U_\mu^\dagger(x+\hat{\nu})U_\nu^\dagger(x), \tag{46}$$

a graphical representation of which is given in figure 2.6.

2.5.2 Confinement, the Polyakov loop and center symmetry

Of crucial importance in lattice field theory is the relation between the path integral and energy eigenstates of the system under consideration, given by

$$\frac{1}{Z}\int \mathcal{D}[C]e^{-S_E[C]}O_1O_2 = \sum_n \langle 0|\hat{O}_1|n\rangle \langle n|\hat{O}_2|0\rangle e^{-tE_n}. \tag{47}$$

On the right hand side, the sum runs over all eigenstates n of the corresponding Hamiltonian, and contains the overlaps of operators $\hat{O}_1$ and $\hat{O}_2$ with n, as well as the energy E_n. This relation is used to extract most quantities in a lattice simulation. Often the leading contributions are of interest, which become dominant at larger times t. Therefore one usually studies the asymptotic behaviour of (47).

Now a *Wilson loop* is defined as

$$W_\mathcal{L}[U] = \mathrm{Tr}\prod_\mathcal{L} U_\mu(x), \tag{48}$$

where the product contains all gauge links belonging to a closed loop $\mathcal{L}$. The loop $\mathcal{L}$ consists of two spatial lines between spatial points $\boldsymbol{x}$ and $\boldsymbol{y}$, and are itself connected through two temporal lines. Its expectation value can be calculated using (47) and written as

$$\langle W_\mathcal{L}\rangle \propto e^{-tE_1}\left(1+\mathcal{O}(e^{-t\Delta E}\right). \tag{49}$$

This is the leading order contribution in (47). The Wilson loop can be identified with the energy of two color charges at positions $\boldsymbol{x}$ and $\boldsymbol{y}$, which propagate for a time t. At asymptotic times, where the

corrections in (49) are suppressed, the energy level can therefore be identified with the static potential $E_1 = V(r = |\boldsymbol{x} - \boldsymbol{y}|)$ between the color charges. A possible parametrization of $V(r)$ is

$$V(r) = V_0 + \frac{1}{r}c + \sigma r, \tag{50}$$

which has proven to accurately describe numerical data for $\mathrm{SU}(3)$ gauge theory. The coulombic part resembles electrodynamics and encodes single gluon exchange, as the gluon self interaction vanishes for small coupling and the field strength of QED is approximated. The linear term in (50) is characterized by the *string tension* σ. It implies growing potential energy between two color charges as the distance between them is increased, which is a strong indication for color confinement.

A *Polyakov loop* is defined as

$$P(\boldsymbol{x}) = \mathrm{Tr} \prod_{t=0}^{N_t-1} U_4(\boldsymbol{x}, t), \tag{51}$$

which is gauge invariant assuming periodic boundary conditions. The expectation value for two Polyakov loops is

$$\langle P(\boldsymbol{x}) P^\dagger(\boldsymbol{y}) \rangle \propto e^{-aN_t V(r)} \left(1 + \mathcal{O}(e^{-aN_t \Delta E}\right). \tag{52}$$

As it is discussed *e.g.* in section 12.1.1 of [26], for large distances r expression (52) can be related to the free energy F_q of an isolated, single color charge at temperature T

$$\langle P \rangle \sim e^{-F_q/T}. \tag{53}$$

Now a *center transformation* multiplies all temporal links in a single timeslice with an element of the center group Z_3 of $\mathrm{SU}(3)$. By definition, any $z \in Z_3$ commutes with all elements in $\mathrm{SU}(3)$. Thus,

$$U_4 \to z U_4 = U_4 z \tag{54}$$

and the expectation value of an Polyakov loop gets modified $\langle P \rangle \to z \langle P \rangle$. On the other hand, transformation (54) leaves all closed gauge loops invariant, and so the basic elements of the gauge action. The path integral measure stays invariant, and the expectation value of a Polyakov loop can be written as

$$\langle P \rangle = \frac{1}{3} \left\langle P + zP + z^2 P \right\rangle = 0. \tag{55}$$

The last step follows due to the property of center elements

$$1 + e^{\mathrm{i}2\pi/3} + e^{-\mathrm{i}2\pi/3} = 0. \tag{56}$$

An interpretation of (53) and (55) is that the free energy F_q of a single color charge is infinite, and that no such objects can be observed, *i.e.* color charges are confined.

It has been verified numerically that after some critical temperature T_c the expectation value of the Polyakov loop gets a non-vanishing value $\langle P \rangle \neq 0$ and Z_3 center symmetry is spontaneously broken. Therefore, with increasing temperature there is some possibility of single, deconfined color charges with finite energy F_q. The expectation value of the Polyakov loop as criterion for Z_3 symmetry can thus be used as order parameter for color-confinement in $\mathrm{SU}(3)$ gauge theory.

Chapter 3

Chiral Symmetry and the Hadron spectrum

In this chapter the global symmetries of QCD are discussed. If not states otherwise, two quark flavors with exact isospin symmetry are assumed, as for the lattice studies later on this will be of relevance. The considerations in principle also hold for higher numbers of mass degenerate flavors, phenomenologically a flavor $\mathrm{SU}(3)$ is somewhat justified. Especially the classification of the hadronic spectrum into multiplets of the chiral-parity group in subsection 3.3 will be important for the interpretation of the lattice data. The presentation follows [46, 47].

3.1 Global symmetries of QCD

The free Dirac equation for spinors Ψ of n_f flavors has the global symmetry structure

$$\mathrm{SU}(n_f)_L \times \mathrm{SU}(n_f)_R \times \mathrm{U}(1)_V \times \mathrm{U}(1)_A. \tag{57}$$

Including QCD interaction – or any vector–like interaction in general – does a priori not change this structure. Hence the fermionic part of the massless lagrangian density of QCD

$$\mathcal{L} = \bar{\Psi} \mathrm{i} \gamma^\mu D_\mu \Psi \tag{58}$$

also shows this symmetries (57). To discuss the different parts in more detail, first the transformations of Dirac spinors will be introduced.

The basic $\mathrm{U}(1)$ flavor singlet, vector–like transformations are given by

$$\mathrm{U}(1)_V \quad \begin{cases} \Psi & \to & e^{-i\theta}\Psi \\ \bar{\Psi} & \to & \bar{\Psi} e^{+i\theta}. \end{cases} \tag{59}$$

Additionally, flavor singlet *axial* transformations can be defined

$$\mathrm{U}(1)_A \quad \begin{cases} \Psi & \to & e^{-\mathrm{i}\gamma_5\theta}\Psi \\ \bar{\Psi} & \to & \bar{\Psi} e^{-\mathrm{i}\gamma_5\theta}. \end{cases} \tag{60}$$

For the flavor non-singlet case the vector–like transformations read

$$\mathrm{SU}(n_f)_V \quad \begin{cases} \Psi & \to & e^{-\mathrm{i}(\mathbb{1}\otimes\vec{\tau}/2)\vec{\theta}}\Psi \\ \bar{\Psi} & \to & \bar{\Psi} e^{+\mathrm{i}(\mathbb{1}\otimes\vec{\tau}/2)\vec{\theta}}, \end{cases} \tag{61}$$

and the corresponding axial transformations

$$\mathrm{SU}(n_f)_A \quad \begin{cases} \Psi & \to & e^{-\mathrm{i}(\gamma_5 \otimes \vec{\tau}/2)\vec{\theta}}\Psi \\ \bar{\Psi} & \to & \bar{\Psi}e^{-\mathrm{i}(\gamma_5 \otimes \vec{\tau}/2)\vec{\theta}}. \end{cases} \tag{62}$$

The transformations (61) and (62) contain group generators of the flavor symmetry group in the exponent. For $\mathrm{SU}(2)$ isospin symmetry they are given by the Pauli matrices $\vec{\tau}$. Each of the transformations (59)–(61) form closed groups, as indicated by their labeling. Operations (62) do not[1]. In a mathematical strict sense $\mathrm{SU}(n_f)_V \times \mathrm{SU}(n_f)_A$ is a group containing transformations (62). However, to avoid unnecessary confusion we will use the language of group theory for (62) alone.

Now it is useful to define projection operators

$$P_{R/L} = \frac{1}{2}\left(\mathbb{1} \pm \gamma_5\right), \tag{63}$$

which obey

$$\begin{aligned} P_L + P_R &= 1 \qquad \text{(completeness)}, \\ P_{R/L}^2 &= P_{R/L} \quad \text{(idempotence)}, \\ P_L P_R &= 0 \qquad \text{(orthogonality)}. \end{aligned} \tag{64}$$

Their action on Dirac spinors is defined as

$$P_{R/L}\Psi = \Psi_{R/L}, \tag{65}$$

$$\bar{\Psi}P_{R/L} = \bar{\Psi}_{L/R}. \tag{66}$$

Using this projection operators, the massless QCD lagrangian (58) and thus the theory can be split into two separate parts

$$\bar{\Psi}\mathrm{i}\gamma^\mu D_\mu \Psi = \bar{\Psi}_L \mathrm{i}\gamma^\mu D_\mu \Psi_L + \bar{\Psi}_R \mathrm{i}\gamma^\mu D_\mu \Psi_R. \tag{67}$$

A mass term in the lagrangian density – or generally any term which does not commute with γ_5 – would mix the two separate parts. Now both terms in (67) are separately invariant under $\mathrm{SU}(n_f)_V$ rotations, as well as both flavor singlet transformations (59) and (60), and the symmetry structure (57) is shown.

3.2 Chiral symmetry breaking

The considerations in section 3.1 follow mostly classical arguments. In a quantum field theory there are 3 sources of breaking for classical chiral symmetry, which will be discussed in the following.

As already mentioned, the splitting of a theory (67) and thus the symmetry structure (57) hold for vanishing quark masses. In nature, the fundamental fermions of the standard model have masses and the assumptions of section 3.1 are violated *explicitly*. However, the masses of *up* and *down* quarks are of the order of 5 MeV, whereas the mass scale of QCD is a few hundred MeV. Hence the assumption of massless quarks is for the $n_f = 2$ isospin case reasonable. The mass of *strange* quarks is of the order of 100 MeV, and some arguments may also apply for flavor $\mathrm{SU}(3)$ chiral symmetry.

3.2.1 $\mathrm{U}(1)_A$ anomaly

As it was mentioned, the lagrangian density of QCD is invariant under axial flavor singlet transformations (60). The integration measure of the path integral, however, is not. This is known as *Adler-*

[1] This can be seen *e.g.* by the *Baker–Campbell–Hausdorff* formula $e^X e^Y = e^{X+Y+1/2[X,Y]+\cdots}$ for linear operators X and Y. The commutator for two (62) transformations does neither vanish, nor is it a 'group element'.

Bell-Jackiw anomaly (ABJ) and a genuine effect of quantum field theories [48]. It was shown by Fujikawa [49, 50] that the integration variables transform non-trivially under axial flavor singlet transformations, and therefore give rise to an *anomalous* contribution

$$\mathcal{A}(x) = \frac{1}{32\pi^2}\epsilon_{\mu\nu\rho\sigma}\mathrm{Tr}G_{\mu\nu}(x)G_{\rho\sigma}(x) \tag{68}$$

to the axial flavor singlet current.

The axial anomaly is also strongly linked to the topology of a gauge field by the following considerations. The Atiyah–Singer theorem [51, 52] links the number of left- and righthanded zero modes n_- and n_+ of the Dirac operator with the topological charge Q_{top} of a certain gaugefield configuration in the following way:

$$Q_{top} = n_- - n_+. \tag{69}$$

The topological charge on the other hand can be calculated by integrating the topological density of the gaugefield

$$Q_{top} = \int \mathrm{d}^4x q(x), \quad q(x) = \frac{1}{32\pi^2}\epsilon_{\mu\nu\rho\sigma}\mathrm{Tr}G_{\mu\nu}(x)G_{\rho\sigma}(x). \tag{70}$$

Due to (69) it is clear that Q_{top} is integer-valued and an invariant property of this realization of the gaugefield. One interpretation of the topological charge are *instanton* quasiparticles, which can be shown to effectively break $\mathrm{U}(1)_A$ symmetry [53].

To summarize this second mechanism of symmetry breaking one can note that in a quantum field theory the $\mathrm{U}(1)_A$ symmetry of fermions in (57) is *anomalously* broken through the non-trivial topology of the gauge field.

3.2.2 Spontaneous breaking

The third mechanism of symmetry breaking is due to the fluctuations of the quark fields in the vacuum. Thereby the chiral condensate $\langle\bar{\Psi}\Psi\rangle$ is allowed to take on a non-vanishing value. Now any transformation U of a 'would-be' symmetry G of the theory can act on this state, *e.g.* transformations (59)–(62). If the vacuum state stays invariant under this operation $U \in G$,

$$U\left|0\right\rangle = \left|0\right\rangle, \tag{71}$$

the symmetry is considered to be realized in the *Wigner-Weyl* mode. The symmetry is exact and the spectrum forms degenerate multiplets of this symmetry. The second possibility for the response of the vacuum to the group transformation U is a non-trivial transformation

$$U\left|0\right\rangle \neq \left|0\right\rangle. \tag{72}$$

In this case the symmetry is said to be realized in the *Nambu–Goldstone* mode and spontaneously broken. Furthermore, the Goldstone theorem [54] states that for every broken symmetry generator in the Nambu–Goldstone mode there has to be a massless 'Goldstone' boson in the spectrum. This is the case for the axial transformations (60) and (62). As an illustration we study the latter $n_f = 2$ axial transformation for the chiral condensate of the vacuum. A term $\bar{\Psi}\Psi$ transforms

$$\bar{\Psi}\Psi \xrightarrow{\mathrm{SU}(2)_A} \cos\theta\left(\bar{\Psi}\Psi\right) + \mathrm{i}\sin\theta\frac{\vec{\theta}}{\theta}\left(\bar{\Psi}\left(\gamma_5 \otimes \vec{\tau}\right)\Psi\right). \tag{73}$$

The vacuum expectation value of the chiral condensate $\langle\bar{\Psi}\Psi\rangle$ thus would modify the parity of the vacuum. This is not realized in nature, and the symmetry is in a Nambu-Goldstone mode. The extra term in (73) has negative parity and isospin $I = 1$, hence the corresponding Goldstone boson can be identi-

fied with the pion. For QCD the chiral condensate $\langle\bar{\Psi}\Psi\rangle$ is the source of the spontaneous breaking of chiral symmetry and thus usually identified as order parameter.

The vector transformations (59) and (61) not only leave the vacuum invariant in QCD, but the *Vafa-Witten* theorem [55] states that these symmetries cannot be broken spontaneously in local vector-like gauge theories. For a non-vanishing value of $\langle\bar{\Psi}\Psi\rangle$ the flavor non-singlet symmetries of massless QCD are therefore broken down to the vector subgroup

$$\mathrm{SU}(n_f)_L \times \mathrm{SU}(n_f)_R \xrightarrow{\langle\bar{\Psi}\Psi\neq 0\rangle} \mathrm{SU}(n_f)_V. \tag{74}$$

3.2.3 Phenomenology

The Goldstone theorem has remarkable consequences for the meson spectrum of QCD. In principle the $J = 0$ pseudoscalar mesons of the quark model can be identified with the Goldstone bosons of chiral symmetry and should therefore be massless. In nature they are found massive, which is a consequence of the explicit breaking due to non-vanishing quark masses. This is supported by the mass difference of 'isospin' pions and '$\mathrm{SU}(3)$' kaons, as the *strange* mass of $\mathrm{SU}(3)$ is an order of magnitude larger than the *up* and *down* masses and the explicit breaking a lot more severe.

There is a peculiarity concerning the flavorless mesons π^0, η and η', which are according to the quark model described by

$$\pi^0 = \frac{1}{\sqrt{2}}\left(\bar{u}u - \bar{d}d\right), \tag{75}$$

$$\eta_8 = \frac{1}{\sqrt{6}}\left(\bar{u}u + \bar{d}d - 2\bar{s}s\right), \tag{76}$$

$$\eta_1 = \frac{1}{\sqrt{3}}\left(\bar{u}u + \bar{d}d + \bar{s}s\right), \tag{77}$$

where the π^0 belongs to the $I = 1$ triplet, and the η's to the $\mathrm{SU}(3)$ octet and singlet[2]. They can be identified as Goldstones of the corresponding chiral transformations, with the aforementioned considerations of explicit symmetry breaking. The $\eta_1 \sim \eta'$ however features an even higher mass than an explicitly broken Goldstone mode would suggest. This is due to the corresponding $\mathrm{U}(1)_A$ symmetry, which is not only broken explicitly and spontaneously, but in addition by the axial anomaly. Hence the η' almost does not 'feel' any consequences from its nature as Goldstone boson and its mass falls into the range of ordinary hadrons.

On top of these findings *chiral perturbation theory* was developed as an effective theory to describe the low-energy dynamics of QCD. An important relation therein is the *Gell-Mann–Oakes–Renner* relation [56] , which encodes and summarizes the topics of this section by quantitatively relating the pion mass to the quark masses and chiral condensate. For two flavors its leading order contribution reads

$$m_\pi^2 = -\frac{1}{F_\pi^2}\frac{m_u + m_d}{2}\left(\langle\bar{u}u\rangle + \langle\bar{d}d\rangle\right). \tag{80}$$

[2] The physical η and $\eta'(958)$ are mixtures of the octet and singlet states

$$\eta = \eta_8 \cos\theta_P - \eta_1 \sin\theta_P \tag{78}$$

$$\eta' = \eta_8 \sin\theta_P + \eta_1 \cos\theta_P \tag{79}$$

characterized by the pseudoscalar mixing angle θ_P, which has empirically been found to be $-20° < \theta_P < -10°$.

3.3 Hadron multiplets

In the following we study the chiral-parity group, and how its representations structure the hadronic states composed of quarks and antiquarks. We will use the method of *Young tableaux*, a short introduction to this method can be found *e.g.* in chapter 46 of [31]. A more detailed discussion on the multipelts itself is given in *e.g.* [47, 57]. This can be done for $\mathrm{SU}(3)$ or generally any number of flavors, but here we focus on two flavors and identify the representations of the $\mathrm{SU}(2)$ isospin group.

3.3.1 Meson multiplets

Using the language of Young tableaux, a single quark as combination of left and right handed components is represented by

$$\square = (\square_L \oplus \square_R). \tag{81}$$

The combination of two such quarks gives

$$\Big(\square_L \oplus \square_R\Big) \otimes \Big(\square_L \oplus \square_R\Big) = \square\square_L \oplus \begin{array}{|c|}\hline\\\hline\end{array}_L \oplus \square_L\square_R \oplus \square_R\square_L \oplus \square\square_R \oplus \begin{array}{|c|}\hline\\\hline\end{array}_R. \tag{82}$$

Applying a notation (I_L, I_R) with $I_{L/R}$ the left and right handed isospin of a state this translates to

$$\Big((\tfrac{1}{2},0) \oplus (0,\tfrac{1}{2})\Big) \otimes \Big((\tfrac{1}{2},0) \oplus (0,\tfrac{1}{2})\Big) = (1,0) \oplus (\tilde{0},0) \oplus (\tfrac{1}{2},\tfrac{1}{2}) \oplus (\tfrac{1}{2},\tfrac{1}{2}) \oplus (0,1) \oplus (0,\tilde{0}), \tag{83}$$

where $\tilde{0}$ denotes two quarks which couple to 0 isospin, in contrast to a plain 0 which means total absence of isospin carrying quarks. In terms of multiplicities of the group representations this corresponds to

$$\mathbf{3} \oplus \mathbf{1} \oplus \mathbf{4} \oplus \mathbf{4} \oplus \mathbf{3} \oplus \mathbf{1}. \tag{84}$$

Considering parity as good quantum number and combining this representations of the chiral group to irreducible representations of the chiral-parity group, we can write

$$\Big[(1,0) \oplus (0,1)\Big] \oplus (\tfrac{1}{2},\tfrac{1}{2}) \oplus (\tfrac{1}{2},\tfrac{1}{2}) \oplus \Big[(\tilde{0},0) \oplus (0,\tilde{0})\Big] \tag{85}$$

with multiplicities

$$\mathbf{6} \oplus \mathbf{4} \oplus \mathbf{4} \oplus \mathbf{2}. \tag{86}$$

This way also parity transformations, which exchange left and right isospin, are valid group operations.

3.3.2 Baryon multiplets

Extending this considerations to baryonic bound states of three quarks

$$\Big(\square_L \oplus \square_R\Big) \otimes \Big(\square_L \oplus \square_R\Big) \otimes \Big(\square_L \oplus \square_R\Big), \tag{87}$$

the following multiplet structure is calculated:

$$\begin{aligned}\Big(\square\square_L \oplus \begin{array}{|c|}\hline\\\hline\end{array}_L \oplus \square_L\square_R \oplus \square_R\square_L \oplus \square\square_R \oplus \begin{array}{|c|}\hline\\\hline\end{array}_R\Big) \times \Big(\square_L \oplus \square_R\Big) = \\ \Big(\square\square\square_L \oplus \begin{array}{|cc|}\hline\\\hline\end{array}_L\Big) \oplus \Big(\begin{array}{|cc|}\hline\\\hline\end{array}_L\Big) \oplus \Big(\square\square_L\square_R \oplus \begin{array}{|c|}\hline\\\hline\end{array}_L\square_R\Big) \oplus \\ \Big(\square_R\square\square_L \oplus \square_R\begin{array}{|c|}\hline\\\hline\end{array}_L\Big) \oplus \Big(\square\square_R\square_L\Big) \oplus \Big(\begin{array}{|c|}\hline\\\hline\end{array}_R\square_L\Big) \oplus\end{aligned}$$

$$\Big(\square\square_L\square_R\Big) \oplus \Big(\begin{array}{l}\square\\\square\end{array}_L\square_R\Big) \oplus \Big(\square_L\square\square_R \oplus \square_L\begin{array}{l}\square\\\square\end{array}_R\Big)\oplus$$
$$\Big(\square\square_R\square_L \oplus \begin{array}{l}\square\\\square\end{array}_R\square_L\Big) \oplus \Big(\square\square\square_R \oplus \begin{array}{ll}\square&\square\\\square&\end{array}_R\Big) \oplus \Big(\begin{array}{ll}\square&\square\\\square&\end{array}_R\Big), \quad (88)$$

which in terms of isospin corresponds to

$$(\frac{3}{2},0)\oplus(\frac{\tilde{1}}{2},0)\oplus(\frac{\tilde{1}}{2},0)\oplus(1,\frac{1}{2})\oplus(\tilde{0},\frac{1}{2})\oplus(1,\frac{1}{2})\oplus(\tilde{0},\frac{1}{2})\oplus$$
$$(\frac{1}{2},1)\oplus(\frac{1}{2},\tilde{0})\oplus(1,\frac{1}{2})\oplus(\tilde{0},\frac{1}{2})\oplus(\frac{1}{2},1)\oplus(\frac{1}{2},\tilde{0})\oplus$$
$$(\frac{1}{2},1)\oplus(\frac{1}{2},\tilde{0})\oplus(0,\frac{3}{2})\oplus(0,\frac{\tilde{1}}{2})\oplus(0,\frac{\tilde{1}}{2}), \quad (89)$$

with $\frac{\tilde{1}}{2}$ standing for three quarks coupled to an isospin $\frac{1}{2}$ state. Again, combining this multiplets to irreducible representations of the chiral-parity group we arrive at

$$\Big[(\frac{3}{2},0)\oplus(0,\frac{3}{2})\Big]+3\cdot\Big[(1,\frac{1}{2})\oplus(\frac{1}{2},1)\Big]+3\cdot\Big[(\tilde{0},\frac{1}{2})\oplus(\frac{1}{2},\tilde{0})\Big]+2\cdot\Big[(0,\frac{\tilde{1}}{2})\oplus(\frac{\tilde{1}}{2},0)\Big]. \quad (90)$$

In more detail this irreducible representations of the chiral-parity group consist of:

- $(0,1/2)\oplus(1/2,0)$: A single $(0,1/2)$ representation has multiplicity of **2** due to the interchangeability of u and d quarks. Combining $(0,1/2)$ and $(1/2,0)$ for definite parity adds to a total multiplicity of **4**. There are five such irreducible representations, which are independent from each other. The maximal isospin in this kind of representation is $I=1/2$, which allows only for nucleons.

- $(1,1/2)\oplus(1/2,1)$: Applying the same reasoning as above we add two **6**-fold representations to a representation of total multiplicity of **12**. There are three such representations. Possible isospin values are $I=1/2$ and $3/2$, which corresponds to nucleons and deltas.

- $(0,3/2)\oplus(3/2,0)$: These irreducible representations are constructed by combining two **4**-fold representations to one **8**-fold irreducible representation. The isospin value is $I=3/2$ and thus only deltas fall into this representation.

3.4 Chiral symmetry on the lattice

The constraints necessary for the fermionic part of QCD (58) to be invariant under symmetries (57) can be summarized very concisely by

$$\{D,\gamma_5\}=0, \quad (91)$$

with the Dirac operator $D=\mathrm{i}\gamma^\mu D_\mu$. Now on the lattice, a naive discretization of the Dirac operator $D(x|y)$ connecting lattice points x and y reads

$$D(x|y)=\sum_{\mu=1}^{4}\gamma_\mu\frac{U_\mu(x)\delta_{x+\hat{\mu},y}-U_{-\mu}(x)\delta_{x-\hat{\mu},y}}{2a}. \quad (92)$$

By a lattice Fourier transformation the discretized Dirac operator in momentum space is obtained

$$\tilde{D}(p)=\frac{\mathrm{i}}{a}\sum_{\mu=1}^{4}\gamma_\mu\sin(p_\mu a). \quad (93)$$

Inverting the Dirac operator gives the naive quark propagator on the lattice

$$\tilde{D}^{-1}(p) = -\mathrm{i}a\frac{\sum_\mu \gamma_\mu \sin(p_\mu a)}{\sum_\mu \sin^2(p_\mu a)}, \tag{94}$$

where

$$p = (p_1, p_2, p_3, p_4) \tag{95}$$

is the discretized quark momentum. Here a problem becomes apparent: whereas in the continuum the quark propagator has a single pole at $p = 0$, the lattice version (94) has a pole every time the components of (95) occur in a combination of 0 and π/a, *i.e.* $2^4 = 16$ times. 15 of these poles are unwanted lattice artifacts and known as *doublers*, which spoil the theory.

One way out is to define a slightly modified lattice Dirac operator

$$\tilde{D}(p) = \frac{\mathrm{i}}{a}\sum_{\mu=1}^{4}\gamma_\mu \sin(p_\mu a) + \frac{1}{a}\sum_{\mu=1}^{4}(1-\cos(p_\mu a))\,. \tag{96}$$

The extra term in (96) acts as mass for the unwanted doublers, effectively decoupling them from the spectrum as the lattice spacing decreases $a \to 0$. This lattice discretization of fermions is called *Wilson* fermions. Wilson fermions might seem to solve the 'doubling' problem, but as byproduct trade it for chiral symmetry: with the extra term in (96) acting as mass, the starting point for the discussion of chiral symmetry (91) is not fulfilled anymore.

It is shown quite generally by the *Nielsen–Ninomiya* theorem [58–60] that it is not possible to remove doublers of a fermion discretization for a local definition of chiral symmetry as given in (91).

Instead, an alternative way to treat chiral symmetry on the lattice is by replacing (91) with the *Ginsparg–Wilson* equation [61]

$$\{D, \gamma_5\} = aD\gamma_5 D \tag{97}$$

as starting point. As it can be seen from a on the right side of (97), this term vanishes in the continuum limit $a \to 0$ and the original condition (91) is restored. Rewriting (97) as

$$D\gamma_5 + \gamma_5 D = aD\gamma_5 D \tag{98}$$

$$D\gamma_5 + \gamma_5 D - aD\gamma_5 D = 0 \tag{99}$$

$$D\gamma_5\left(1 - \frac{a}{2}D\right) + (1 - \frac{a}{2}D)\gamma_5 D = 0 \tag{100}$$

suggests the definition of

$$\hat{\gamma}_5 = \gamma_5\,(1 - aD)\,. \tag{101}$$

Modified projection operators can be defined in analogy to the continuum operators (63)

$$\hat{P}_{R/L} = \frac{1}{2}\,(\mathbb{1} \pm \hat{\gamma}_5)\,, \tag{102}$$

which again obey

$$\begin{aligned} \hat{P}_L + \hat{P}_R &= 1 \qquad \text{(completeness)}, \\ \hat{P}^2_{R/L} &= \hat{P}_{R/L} \quad \text{(idempotence)}, \\ \hat{P}_L\hat{P}_R &= 0 \qquad \text{(orthogonality)}. \end{aligned} \tag{103}$$

Thus a modified theory of chiral symmetry can be constructed on the lattice, which offers the possibility for chirally symmetric Dirac operators free of doublers. The obvious tradeoff for this kind of chiral symmetry is the non-locality: chiral properties at each space time point depend on the Dirac operator and

thereby on neighboring lattice sites, as it can be seen in (101).

Two such fermion discretizations obeying (97), the *Overlap* as well as *domain wall* fermions, will be discussed in section 4.2.

Chapter 4

Vacuum QCD on the lattice: operators, eigenmodes and a truncation study

In this chapter numerical results for vacuum QCD will be presented. First a previous truncation study from literature will be discussed, which serves as motivation to study symmetry properties of high temperature QCD later on. Afterwards follows a short presentation of the Dirac operators in use and their chiral properties. Section 4.3 is a technical account on how to extract the relevant correlation functions necessary for spectroscopy from quark propagators on the lattice.

In section 4.4 a quenched $n_f = 2$ simulation using the Overlap operator is presented. The low-mode truncation procedure is applied to this system at various quark masses, which allows to study its effects for different pion masses. Section 4.5 introduces a $n_f = 2$ domain wall fermion simulation and shows first results for correlation functions of mesons and nucleons as reference for the high temperature study.

4.1 A truncation study

In a set of numerical experiments [4–16] — henceforth referred to as *truncation study* — the spectrum of light hadrons was investigated under certain modifications of the Dirac spectrum. Prior to that, a study [1–3] was done in which the lowest modes of the Overlap Dirac operator have been calculated explicitly on the lattice, and its chiral properties been investigated. The truncation studies aim was to look at the hadron spectrum by excluding a certain number of low modes of the Dirac operator. Due to the relation of *Banks–Casher* [62], which links the chiral condensate

$$\langle \bar{\Psi}\Psi \rangle \propto \rho(0) \tag{104}$$

to the density of Dirac eigenmodes $\rho(0)$ close to the origin, also the mechanism of spontaneous chiral symmetry breaking is expected to be located in this region of the eigenmode spectrum. The question was if chiral symmetry gets restored upon exclusion of this part of the theory. The results of this study are shown in figure 4.1. While the ground state pion does not survive this procedure, the remaining spectrum indeed becomes symmetric under chiral symmetry transformations. Even more, an emergent $\mathrm{SU}(4)$ symmetry is observed for $J = 1, 2$ mesons and $J = 1/2$ baryons. Its implications on the fundamental degrees of freedom, quark confinement and high temperature QCD are discussed *e.g.* in [63–65].

However, due to the limited statistics, the numerical data in these studies does not exclude an even larger degeneracy of the $J = 1$ meson $\mathbf{15}$-plet and f_1 singlet of $\mathrm{SU}(4)$. In [66] it is shown that there exists no such standard symmetry, *i.e.* generated by spatial integrals of local operators, which could account for the observed degeneracy pattern. Therefore it is concluded, that either the apparent coincidence of masses in the $\mathbf{15}$-plet and singlet channels is accidental, or requires for a larger non-standard symmetry. A bilocal $\mathrm{SU}(4) \times \mathrm{SU}(4)$ symmetry is proposed for mesons in [67], which naturally explains degeneracies

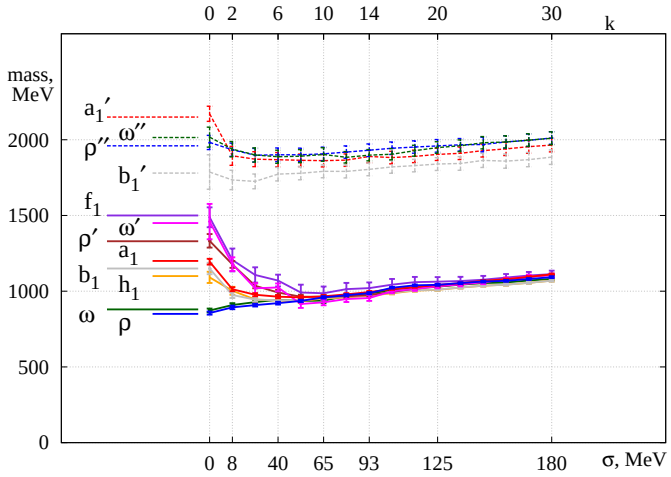

FIGURE 4.1: Light meson spectrum *vs.* number of removed low modes of the Dirac operator. For the unmodified theory ($k = 0$) the mass hierachy found in nature is reproduced, at higher levels of truncation a $\mathrm{SU}(4)$ symmetry emerges in the $n_f = 2$ case. The plot is taken from [12].

of different irreducible representations of a global $\mathrm{SU}(4)$ symmetry. In [68] it is shown how chiral symmetry restoration in a confining theory could generate dynamical quark flavors in color-singlet particle spectrum.

4.2 Dirac operators

When studying the symmetry properties of hadronic matter, a proper fermion discretization is required as well as good control over the parameters of the simulation. The truncatin study 4.1 made use of a chirally improved (CI) Dirac operator, which approximates the Ginsparg–Wilson equation (97), as well as Overlap fermions. Here we use the exact Overlap formalism for the quenched study in 4.4, and the domain wall approximation to Overlap fermions for the main high temperature study.

4.2.1 Overlap operator

The Overlap operator of Neuberger [69,70] is given by

$$D_{\mathrm{ov}} = \frac{1}{2}\left[1 + \gamma_5 \mathrm{sgn}(H_K(M))\right], \tag{105}$$

with some hermitian Wilson-like kernel operator

$$H_K = \gamma_5 (D_K - M). \tag{106}$$

The operator fulfills the Ginsparg–Wilson equation (97) by construction and is chirally symmetric. M is a mass-like parameter which can be used to tune convergence and locality properties. An few interesting properties follow now from the γ_5-hermiticity of the Overlap operator

$$\gamma_5 D_{ov} \gamma_5 = D_{ov}^\dagger \tag{107}$$

and its chirality. Multiplying (97) with γ_5 gives

$$D_{ov}^\dagger + D_{ov} = a D_{ov}^\dagger D_{ov}, \tag{108}$$

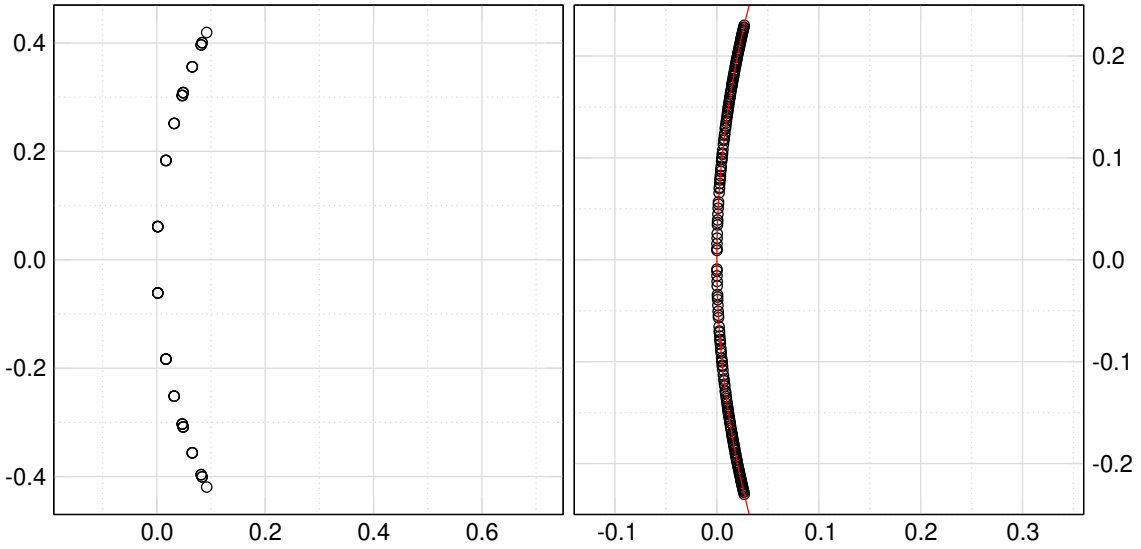

FIGURE 4.2: Lowest eigenvalues of the Overlap operator (105). The left panel shows 50 partly degenerate eigenvalues for a trivial gauge configuration, the right panel shows 200 eigenvalues for an interacting $16^3 \times 32$ gauge configuration. It can be seen that γ_5-hermiticity requires the eigenvalues to appear in complex conjugate pairs, as well as the 'circle' implied by the Ginsparg-Wilson equation.

which in terms of eigenvalues reads

$$\lambda^* + \lambda = a\lambda^*\lambda. \tag{109}$$

Writing the complex eigenvalues as $\lambda = x + \mathrm{i}y$ this can be parametrized as

$$\frac{1}{a^2} = \left(x - \frac{1}{a}\right)^2 + y^2. \tag{110}$$

The eigenvalues of the Overlap operator therefore describe a circle with radius $1/a$ in the complex plane, with the center at $1/a$ on the real axis. A few eigenvalues of an actual numerical calculation are plotted in 4.2. In the continuum limit $a \to 0$ the radius $1/a$ gets infinite and the circular shape approximates the imaginary axis around the origin, *i.e.* the eigenvalues lie on the imagniary axis.

4.2.2 Domain wall approximation

In practice, the evaluation of the sign function in (105) is numerically expensive, which makes large scale simulations with dynamical fermions costly. Depending on the problem one is interested in, exact chiral symmetry might not be necessary, and certain approximations can be used.

One elegant way of approximating exact Overlap fermions is the *domain wall* formalism [71,72]. The general idea is to introduce an auxiliary 5th dimension for fermions with special boundary condition, such that the 4-dimensional boundary contains chiral fermion modes. This way a 5D operator can be constructed, which corresponds to an effective 4D operator

$$D_{DW}(m) = \frac{1+m}{2} + \frac{1-m}{2}\gamma_5 \mathrm{sgn}(H_K). \tag{111}$$

Generally different implementations of domain wall fermions are characterized by their approximation of the sign function, as well as the kernel operator H_K. In this work the sign function is approximated

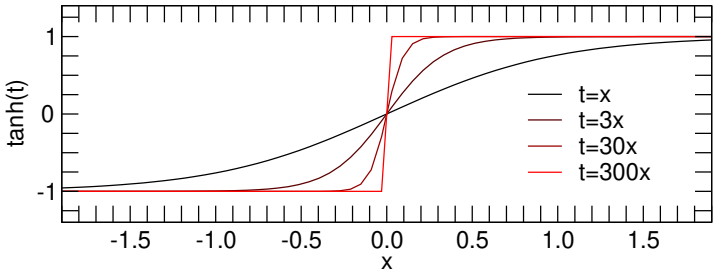

FIGURE 4.3: Tangens hyperbolicus as appriximation for the sign function.

by

$$\mathrm{sgn}(H_K) = \frac{1-(T(H_K))^{L_s}}{1+(T(H_K))^{L_s}}, \tag{112}$$

with

$$T(H_K) = \frac{1-H_K}{1+H_K}. \tag{113}$$

The approximation (112) is called *polar* approximation [19], is equivalent to

$$\tanh\left(L_s \tanh^{-1}(H_K)\right), \tag{114}$$

and becomes more accurate for higher L_s. The kernel operator in this work corresponds to *Möbius domain wall* fermions and is given by

$$H_K(M_5) = \gamma_5 \frac{(b+c)D_W(M_5)}{2+(b-c)D_W(M_5)}, \tag{115}$$

where D_W is the regular Wilson operator and M_5 the mass of the 5-dimensional quarks. The choice of b and c gives different kernel operators, *e.g.* $(b-c)=1$ and $b+c=\alpha$ defines the *scaled Shamir* kernel.

4.3 Operators and Contractions

In the following we will be interested in expectation values of diagonal correlation functions

$$\langle O(x)\bar{O}(y)\rangle, \tag{116}$$

where $O(x)$ and $\bar{O}(y)$ are creation and annihilation operators for hadronic states of fixed quantum numbers. On the lattice, the calculation of this expectation value is split,

$$\langle\langle O(x)\bar{O}(y)\rangle_F\rangle_G, \tag{117}$$

where the subscripts stand for *fermionic* and *gluonic* expectation value, respectively. The latter is done by Monte Carlo averaging over gauge configurations. Given a set of configurations, this is trivial and will not be discussed further. The fermionic expectation value on the other hand is done by applying *Wick's* theorem, which we will show for the operators of interest.

4.3.1 Isovector mesons

A local operator for an isovector meson is given by

$$O_M(x) = \bar{d}(x)\Gamma u(x), \tag{118}$$

where the gamma structure Γ determines the quantum numbers of the state, *e.g.* $\Gamma = \gamma_5$ gives the pion[1]. Its conjugate operator is

$$\bar{O}_M(x) = \bar{u}(x)\Gamma d(x), \tag{119}$$

and the fermionic expecation value of a meson created at space time point x and annihilated at y can be calculated by

$$\begin{aligned}\langle O_M(x)\bar{O}_M(y)\rangle_F &= \langle \bar{d}(x)\Gamma u(x)\bar{u}(y)\Gamma d(y)\rangle_F &(120)\\ &= \Gamma_{\alpha_1\beta_1}\Gamma_{\alpha_2\beta_2}\Big\langle \bar{d}(x)^{\alpha_1}_{c_1} u(x)^{\beta_1}_{c_1}\bar{u}(y)^{\alpha_2}_{c_2} d(y)^{\beta_2}_{c_2}\Big\rangle_F &(121)\\ &= -\Gamma_{\alpha_1\beta_1}\Gamma_{\alpha_2\beta_2}\Big\langle u(x)^{\beta_1}_{c_1}\bar{u}(y)^{\alpha_2}_{c_2}\Big\rangle_u\Big\langle d(y)^{\beta_2}_{c_2}\bar{d}(x)^{\alpha_1}_{c_1}\Big\rangle_d &(122)\end{aligned}$$

Now the quarks have been factorized according to their flavor, as only *up* quarks can annihilate *up* quarks, etc. Now Wick's theorem

$$\Big\langle u(x)^{\beta_1}_{c_1}\bar{u}(y)^{\alpha_2}_{c_2}\Big\rangle_d = D_u^{-1}(x|y)^{\beta_1\alpha_2}_{c_1c_2} \tag{123}$$

can be applied to (122), which gives

$$-\Gamma_{\alpha_1\beta_1}\Gamma_{\alpha_2\beta_2}D^{-1}(x|y)^{\beta_1\alpha_2}_{c_1c_2}D^{-1}(y|x)^{\beta_2\alpha_1}_{c_2c_1}. \tag{124}$$

As we assume isospin symmetry and neglect electromagnetic interactions, the propagators for *up* and *down* quarks are them same, therefore the flavor indices of propagators are neglected from now on. In vector/matrix notation this reads

$$\mathrm{Tr}\left[D^{-1}(x|y)\Gamma D^{-1}(y|x)\Gamma\right]. \tag{125}$$

Equation (125) would require quark propagators from all lattice points to all lattice points, which could amount for large objects in practical implementations. Here the γ_5-hermiticity of quark propagators can be utilized, which is given by

$$D^{-1}(x|y)^*_{dc}{}^{\beta\alpha} = (\gamma_5)_{\alpha\alpha'}D^{-1}(y|x)^{\alpha'\beta'}_{c\,d}(\gamma_5)_{\beta'\beta}. \tag{126}$$

Using (126) in (124) to get the backward running quark propagator from the forward propagator, the expression

$$-D^{-1}(x|y)^{\beta_1\alpha_2}_{c_1c_2}\Gamma_{\alpha_2\beta_2}(\gamma_5)_{\beta_2\beta_2'}D^{-1}(x|y)^*_{\alpha_1'\beta_2'}{}^{\alpha_1'\beta_2'}_{c_1c_2}(\gamma_5)_{\alpha_1'\alpha_1}\Gamma_{\alpha_1\beta_1} \tag{127}$$

is obtained. After absorbing the gamma structures into Γ', this reads

$$D^{-1}(x|y)^{\beta_1\alpha_2}_{c_1c_2}\Gamma'_{\alpha_2\beta_2}D^{-1}(x|y)^*_{\alpha_1\beta_2}{}^{\alpha_1\beta_2}_{c_1c_2}\Gamma'_{\alpha_1\beta_1} \tag{128}$$

and is ready for numeric evaluation.

4.3.2 Light baryons

An interpolator for the nucleon particle is given by

$$O_N^{\pm}(x) = \epsilon_{abc}\mathcal{P}_{\pm}u(x)_a\left[u(x)_b^T C\gamma_5 d(x)_c\right], \tag{129a}$$

[1] A more detailed account on how to construct operators is given *e.g.* in chapter 6 of [26].

where $\mathcal{P}_\pm$ is a parity projector. The term in square brackets is called *diquark*, C is the charge conjugation matrix and the diquark's quantum numbers determined by the gamma structure $C\gamma_5$. Using its conjugate

$$\bar{O}_N^\pm(x) = \epsilon_{abc}\left[\bar{u}(x)_a C\gamma_5 \bar{d}(x)_b^T\right]\bar{u}(x)_c\mathcal{P}_\pm \tag{129b}$$

we can write the fermionic expectation value for the creation and annihilation of a nucleon as

$$\begin{aligned}\langle \bar{O}_N^\pm(y) O_N^\pm(x)\rangle_F = \\ \Big\langle \epsilon_{abc}\epsilon_{a'b'c'}\big[\bar{u}(y)^{\alpha}_{a}(C\gamma_5)_{\alpha\beta}\bar{d}(y)^{\beta}_{b}\big]\bar{u}(y)^{\gamma}_{c}(\mathcal{P}_\pm)_{\gamma\gamma'}u(x)^{\gamma'}_{c'}\big[u(x)^{\alpha'}_{a'}(C\gamma_5)_{\alpha'\beta'}d(x)^{\beta'}_{b'}\big]\Big\rangle_F = \\ \epsilon_{abc}\epsilon_{a'b'c'}(C\gamma_5)_{\alpha\beta}(\mathcal{P}_\pm)_{\gamma\gamma'}(C\gamma_5)_{\alpha'\beta'}\Big\langle\big[\bar{u}(y)^{\alpha}_{a}\bar{d}(y)^{\beta}_{b}\big]\bar{u}(y)^{\gamma}_{c}u(x)^{\gamma'}_{c'}\big[u(x)^{\alpha'}_{a'}d(x)^{\beta'}_{b'}\big]\Big\rangle_F.\end{aligned} \tag{130}$$

The term in angle brackets can be reordered and factorized according to quark flavors

$$\Big\langle u(x)^{\alpha'}_{a'}\bar{u}(y)^{\alpha}_{a}u(x)^{\gamma'}_{c'}\bar{u}(y)^{\gamma}_{c}\Big\rangle_u\Big\langle d(x)^{\beta'}_{b'}\bar{d}(y)^{\beta}_{b}\Big\rangle_d. \tag{131}$$

For the down quarks there is only one possible contraction. After applying Wick's theorem this gives the propagator

$$\Big\langle d(x)^{\beta'}_{b'}\bar{d}(y)^{\beta}_{b}\Big\rangle_d = D_d^{-1}(x|y)^{\beta'\beta}_{b'b}. \tag{132}$$

For the up quarks the situation is a little more interesting: a quark can contract with each one of the anti quarks, the second quark with the remaining anti quark. In this situation there are two possible outcomes. For k quark–anti quark pairs of the same flavor there are generally $k!$ possible contractions. The up quarks contract accordingly

$$\begin{aligned}\Big\langle u(x)^{\alpha'}_{a'}\bar{u}(y)^{\alpha}_{a}u(x)^{\gamma'}_{c'}\bar{u}(y)^{\gamma}_{c}\Big\rangle_u = \\ D_u^{-1}(x|y)^{\alpha'\alpha}_{a'a}D_u^{-1}(x|y)^{\gamma'\gamma}_{c'c} - D_u^{-1}(x|y)^{\alpha'\gamma}_{a'c}D_u^{-1}(x|y)^{\gamma'\alpha}_{c'a},\end{aligned} \tag{133}$$

where the minus sign appears due to the necessary reordering of the Grassmann valued quark fields for the second possible contraction. Collecting all steps we end up with

$$\begin{aligned}\langle \bar{O}_N^\pm(y) O_N^\pm(x)\rangle_F = \epsilon_{abc}\epsilon_{a'b'c'}(C\gamma_5)_{\alpha\beta}(\mathcal{P}_\pm)_{\gamma\gamma'}(C\gamma_5)_{\alpha'\beta'}\times \\ D_d^{-1}(x|y)^{\beta'\beta}_{b'b}\Big(D_u^{-1}(x|y)^{\alpha'\alpha}_{a'a}D_u^{-1}(x|y)^{\gamma'\gamma}_{c'c} - D_u^{-1}(x|y)^{\alpha'\gamma}_{a'c}D_u^{-1}(x|y)^{\gamma'\alpha}_{c'a}\Big).\end{aligned} \tag{134}$$

It can be seen that the first term in the second line of (134) gives two separate traces, whereas the second term results in just one trace connecting all three propagators. The derivation holds for any gamma structure in the diquark and $C\gamma_5$ can easily be replaced in (134).

The corresponding formula for the creation and annihilation of a delta particle can be derived in a similar fashion. Starting from the general isospin $I = 3/2$ valued interpolators

$$O_\Delta^\pm(x) = \epsilon_{abc}\mathcal{P}_\pm\Gamma_1^i u(x)_a\left[u(x)_b^T\Gamma_2^i u(x)_c\right], \tag{135a}$$

$$\bar{O}_\Delta^\pm(x) = \epsilon_{abc}\left[\bar{u}(x)_a\Gamma_2^i\bar{u}(x)_b^T\right]\bar{u}(x)_c\Gamma_1^i\mathcal{P}_\pm \tag{135b}$$

$m_{ud}[a]$	m_π[MeV]
0.319	(961 ± 2) MeV
0.155	(667 ± 4) MeV
0.076	(473 ± 3) MeV
0.038	(339 ± 3) MeV
0.030	(305 ± 3) MeV
0.023	(268 ± 4) MeV

TABLE 4.1: Input quark mass parameters and resulting effective masses of the pion for the quenched Overlap study.

the fermionic expectation value for creation and annihilation is

$$\langle \bar{O}^{\pm}_{\Delta}(y) O^{\pm}_{\Delta}(x) \rangle_F = \epsilon_{abc}\epsilon_{a'b'c'} (\Gamma^i_2)_{\alpha\beta} (\Gamma^i_1)_{\gamma\delta} (\mathcal{P}_{\pm})_{\delta\delta'} (\Gamma^i_1)_{\delta'\gamma'} (\Gamma^i_2)_{\alpha'\beta'} \times \left\langle \left[\bar{u}(y)_{\substack{\alpha\\ a}} \bar{u}(y)_{\substack{\beta\\ b}}\right] \bar{u}(y)_{\substack{\gamma\\ c}} u(x)_{\substack{\gamma'\\ c'}} \left[u(x)_{\substack{\alpha'\\ a'}} u(x)_{\substack{\beta'\\ b'}}\right] \right\rangle_F . \quad (136)$$

Now there are three quark-anti quark pairs of the same flavor and six possible ways to contract them. This gives

$$\begin{aligned} \langle \bar{O}^{\pm}_{\Delta}(y) O^{\pm}_{\Delta}(x) \rangle_F &= \epsilon_{abc}\epsilon_{a'b'c'} (\Gamma^i_2)_{\alpha\beta} (\Gamma^i_1)_{\gamma\delta} (\mathcal{P}_{\pm})_{\delta\delta'} (\Gamma^i_1)_{\delta'\gamma'} (\Gamma^i_2)_{\alpha'\beta'} \times \\ &\Big(D_u^{-1}(x|y)_{\substack{\alpha'\alpha\\ a'a}} D_u^{-1}(x|y)_{\substack{\beta'\beta\\ b'b}} D_u^{-1}(x|y)_{\substack{\gamma'\gamma\\ c'c}} - D_u^{-1}(x|y)_{\substack{\alpha'\alpha\\ a'a}} D_u^{-1}(x|y)_{\substack{\beta'\gamma\\ b'c}} D_u^{-1}(x|y)_{\substack{\gamma'\beta\\ c'b}} \\ &+ D_u^{-1}(x|y)_{\substack{\alpha'\beta\\ a'b}} D_u^{-1}(x|y)_{\substack{\beta'\gamma\\ b'c}} D_u^{-1}(x|y)_{\substack{\gamma'\alpha\\ c'a}} - D_u^{-1}(x|y)_{\substack{\alpha'\beta\\ a'b}} D_u^{-1}(x|y)_{\substack{\beta'\alpha\\ b'a}} D_u^{-1}(x|y)_{\substack{\gamma'\gamma\\ c'c}} \\ &+ D_u^{-1}(x|y)_{\substack{\alpha'\gamma\\ a'c}} D_u^{-1}(x|y)_{\substack{\beta'\alpha\\ b'a}} D_u^{-1}(x|y)_{\substack{\gamma'\beta\\ c'b}} - D_u^{-1}(x|y)_{\substack{\alpha'\gamma\\ a'c}} D_u^{-1}(x|y)_{\substack{\beta'\beta\\ b'b}} D_u^{-1}(x|y)_{\substack{\gamma'\alpha\\ c'a}} \Big). \end{aligned} \quad (137)$$

Out of these six terms, two result in two separate traces. The remaining four terms contribute as a single trace connecting all propagators.

4.4 Quenched simulation

In this section a $n_f = 2$ flavor simulation of QCD on a $12^3 \times 24$ lattice is presented. The valence quarks are Overlap fermions with an polynomial approximation for the sign function. The Dirac sea is quenched, *i.e.* the fermion determinant is set to 1

$$\det[D_u] = \det[D_d] = 1. \quad (138)$$

As gauge action the Lüscher–Weisz action [73, 74] is applied. The simulation is done for a single value of $\beta = 7.7$, and setting the scale according to [75] results in a lattice spacing $a = (0.175 \pm 0.01)$ fm. This gives a total box length of 2.1 fm and a lattice cutoff $1/a = (1120 \pm 80)$ MeV. The gauge configurations are stout smeared once[2]. A total number of 1100 configurations have been accumulated, and thermalization was reached after 110 configurations.

This set of parameters may seem quite modest compared to todays standards. The aim however is not to extract high precision data, but to qualitatively study the truncation method introduced in section 4.1, its effects and dependence on the pion mass. Therefore the quark propagators are calculated for six different masses, the resulting pion masses are given in table 4.1.

[2] The procedure of stout smearing is discussed in appendix C.2

meson	J^{PC}	interpolator
π	0^{-+}	$\bar{q}_n\gamma_5 q_n$
		$\bar{q}_w\gamma_5 q_w$
a_0	0^{++}	$\bar{q}_n\mathbb{1} q_n$
		$\bar{q}_w\mathbb{1} q_w$
ρ	1^{--}	$\bar{q}_n\gamma_k q_n$
		$\bar{q}_w\gamma_k q_w$
		$\bar{q}_n\gamma_k\gamma_4 q_n$
		$\bar{q}_w\gamma_k\gamma_4 q_w$
a_1	1^{++}	$\bar{q}_n\gamma_k\gamma_5 q_n$
		$\bar{q}_w\gamma_k\gamma_5 q_w$
b_1	1^{+-}	$\bar{q}_n\gamma_k\gamma_4\gamma_5 q_n$
		$\bar{q}_w\gamma_k\gamma_4\gamma_5 q_w$

TABLE 4.2: Interpolator basis of isovector mesons for variational analysis. Subscripts of quark fields give the smearing level.

Spectroscopy is done using the *variational analysis* method, described *e.g.* in [76]. To extend the operator basis, the quark sources are smeared before inverting the Dirac operator and thus improve the overlap of interpolating fields with physical states. Thereby the coupling to lower lying states should be improved and the ground state in a given channel extracted more reliably.

Specifically, we use *Jacobi* smearing as described in [77]. An initial point source is given by $s_0^{(\alpha,a)}$. Applying the smearing operator

$$M = \sum_{n=0}^{N} (\kappa H)^n \tag{139}$$

gives the smeared source $s^{(\alpha,a)} = M s_0^{(\alpha,a)}$, where H is given by

$$H(\vec{x},\vec{y}) = \sum_{j=1}^{3} \left[U_j(\vec{x},0)\delta(\vec{x}+\hat{j},\vec{y}) + U_j(\vec{x}-\hat{j},0)^\dagger \delta(\vec{x}-\hat{j},\vec{y}) \right]. \tag{140}$$

In (139) there are two free parameters to choose: the number of smearing steps N, as well as the coefficient κ. Both can be tuned to maximize the physical overlap of the initial field excitation to the state one intents to probe. The data presented in this section uses two levels of smearing, denoted by the tuple (κ, N):

$$narrow \quad (0.335/4) \tag{141a}$$
$$wide \quad (0.191/41) \tag{141b}$$

The level of smearing will be denoted by a subscript n or w of the quark fields, for *narrow* and *wide* respectively[3]. Next we assemble a matrix for a given J^{PC} channel by calculating the cross correlations

$$C(t)_{kl} = \left\langle O_k(t) O_l^\dagger(0) \right\rangle, \tag{142}$$

where the operators are listed in 4.2. Now calculating the eigenvalues of (144) with the generalized eigenvalue problem (GEVP)

$$\lambda^{(k)}(t) \propto e^{-tM_k} \left[1 + \mathcal{O}(e^{-t\Delta M_k}) \right], \tag{143}$$

[3] We use the same labels as in [77], but the parameters have been adjusted to our lattice setup.

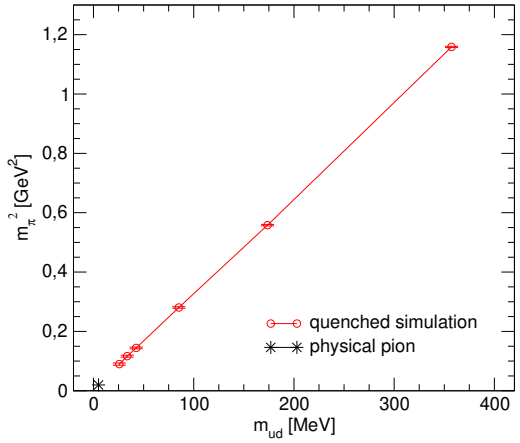

FIGURE 4.4: Gell-Mann–Oaks–Renner relation: The linear dependence of m_π^2 on the quark masses is realized with high precision. This is a manifestation of the exact chiral symmetry of the Overlap operator in use.

a diagonal matrix with entries $\lambda^{(1)}, \lambda^{(2)}, ..$ is obtained. The entries of the diagonalized matrix can be interpreted as diagonal correlators of 'optimal' operators $\tilde{O}$ to probe the ground state of the channel, first excited state, etc. Imposing the vacuum interpretation of QCD as described in 2.5 and using (47), the diagonal entries of this matrix read

$$C(t)_{kk} = \sum_n \langle 0|\tilde{O}_k|n\rangle\langle n|\tilde{O}_k^\dagger|0\rangle e^{-tM_n} \tag{144}$$

with $\langle 0|\tilde{O}_k|n\rangle$ being the overlap of operator $\tilde{O}_k$ with physical state $|n\rangle$. effective masses of corresponding states can be extracted by fitting the logarithmic derivative

$$m^k(t+\frac{1}{2}) = \ln\left[\frac{\lambda^{(k)}(t)}{\lambda^{(k)}(t+1)}\right]. \tag{145}$$

In order for the energy level to be a real physical bound state according to (143), the effective mass (145) should show a consistent plateau in the asymptotic regime, before statistical noise starts to dominate the signal.

The truncation procedure, which is described in detail *e.g.* in [4], consists of calculating the lowest eigenmodes λ_i of the operator $D_5 = \gamma_5 D$, and constructing the reduced quark propagator

$$D_{red}^{-1} = D^{-1} - \sum_{i\leq k} \frac{1}{\lambda_i} |\lambda_i\rangle \langle\lambda_i| \gamma_5. \tag{146}$$

Now for the fermionic contractions D_{red}^{-1} is used, and the extraction of effective masses is done for various stages of truncation, denoted by the number of removed eigenmodes k.

The reliability of the simulation is first checked by evaluating the Gell-Mann–Oakes–Renner relation in figure 4.4 and trying to find the notoriously hard a_0 state in figure 4.5. The signal for the pion looses its exponential decay upon truncating a few low modes and thus vanishes from the spectrum. This is in accordance with its nature as Goldstone boson, as the truncation supposedly removes the spontaneous breaking of chiral symmetry. Figure 4.6 finally shows the isovector vector mesons for different levels of truncation and pion masses. Parity doubling is observed, as well as an additional symmetry consistent with $\mathrm{SU}(2)_{CS}$ and $\mathrm{SU}(4)$. Overall this data shows agreement with previous studies presented in section 4.1.

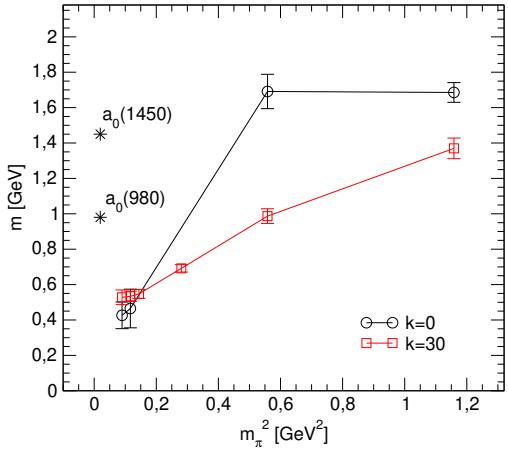

FIGURE 4.5: Effective masses in the a_0 channel. The scalar meson suffers from a particular heavy quenching artifact, see *e.g.* [78–80]. A negative ghost term becomes dominant at lower quark masses and spoils the signal of $\bar{q}q$ states in this channel.

4.5 Vacuum DWF

In this section the simulation setup using dynamical domain wall fermions is introduced, which will be used later in the high temperature study.

The fermion discretization for sea and valence quarks is the Möbius domain wall fermion with a scaled $\alpha = 2$ Shamir kernel, as described in section 4.2.2. For the gauge sector, tree-level improved Symanzik action is used, and the gauge fields are smeared three times using stout smearing.

The setup of our implementation has been tested extensively in literature. The motivation to use domain wall fermions instead of exact Overlap fermions is a significant reduction in computational cost. The domain wall approximation is controlled by varying L_s, and implies a non-vanishing violation of the Ginsparg–Wilson equation (97), which can be quantified by a *residual mass* m_{res}. This violation for the given setup has been tested in [81] and [82]. The pion mass for different parameters is determined in [83], most notably it has been verified that the pion mass essentially is the same for different topological sectors. The autocorrelation properties of the setup are discussed *e.g.* in [84].

The scale in this simulation is set [19] through

$$a = c_0 f(g^2) \left(1 + c_2 f(g^2)^2\right) \tag{147}$$

with

$$f(g^2) = (b_0 g^2)^{-b_1/2b_0^2} \exp\left(-\frac{1}{2b_0 g^2}\right). \tag{148}$$

The parameters are

$$b_0 = \frac{1}{(4\pi)^2}\left(11 - \frac{2}{3}N_f\right), \quad b_1 = \frac{1}{(4\pi)^2}\left(102 - \frac{38}{3}N_f\right), \tag{149}$$

where $g^2 = 6/\beta$, the number of flavors $N_f = 2$ and c_0 and c_2 are fitted as $6.9(2)$ and $6.1(6) \times 10^3$ respectively. A graphical representation of the lattice spacing in dependence of β is shown in figure 4.7. A list of β values and corresponding lattice spacings a and cutoffs $1/a$ is given in table 4.3. Most measurements in the following are done using the 'IroIro' software [85].

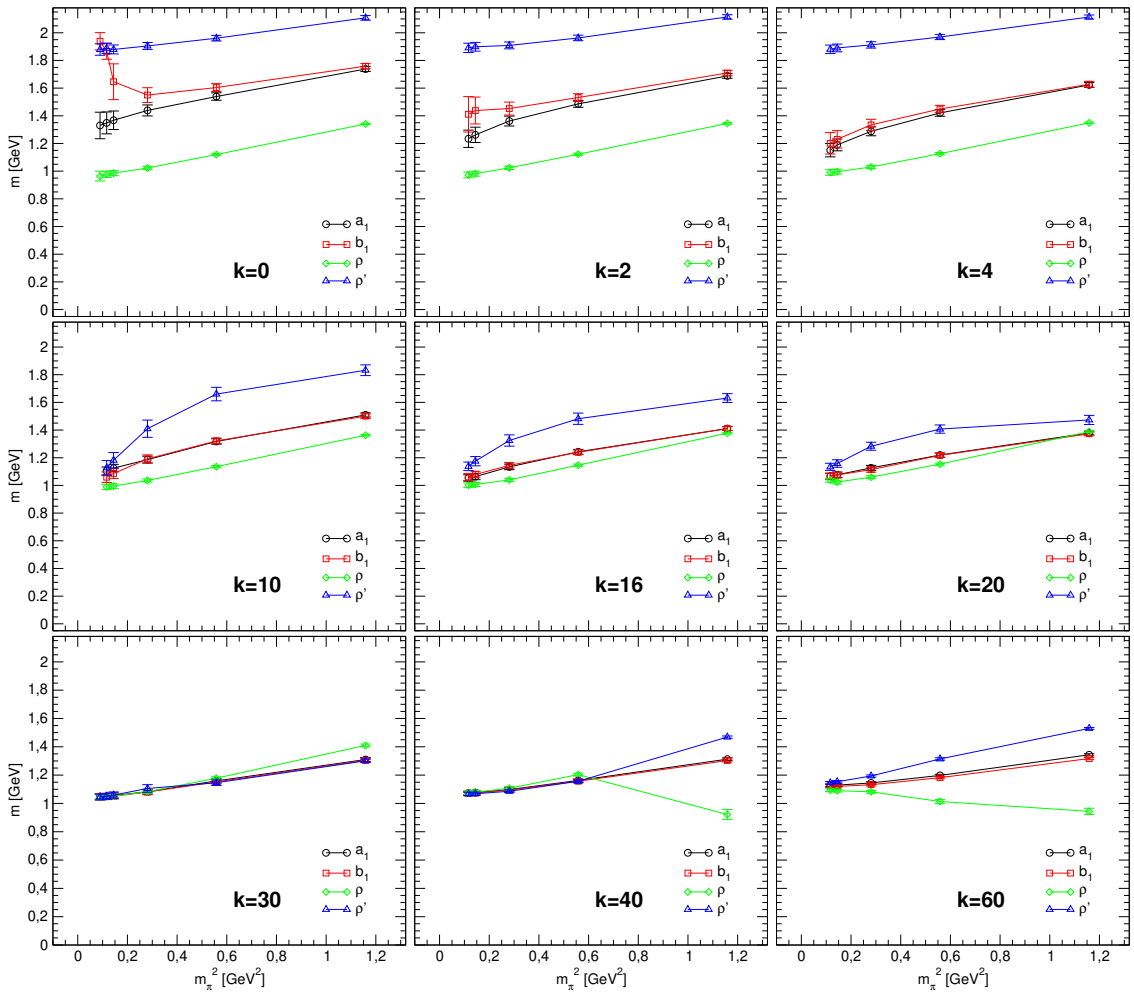

FIGURE 4.6: Isovector $J = 1$ mesons for various levels of truncation, k denotes the number of removed eigenmodes. For the ρ channel, the first two energy levels are extracted, which correspond to ground state and first excited state. For the 'full' theory in the upper left panel a well pronounced mass splitting is seen for all three vector states. Upon truncation, the pseudovectors 'loose' mass and approach the ρ ground state. The effects of truncation are more pronounced for lower pion masses.

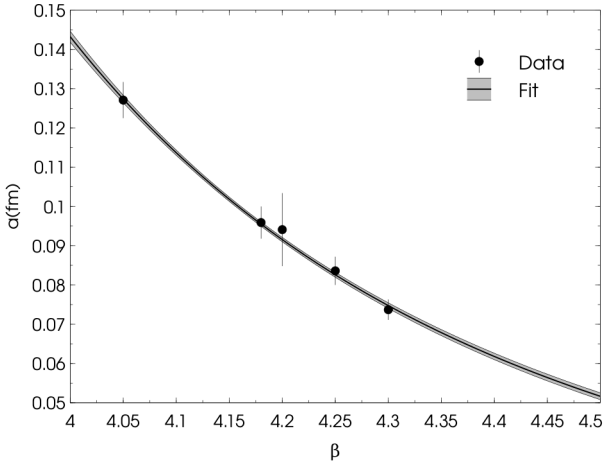

FIGURE 4.7: Lattice spacing in dependence of β. The plot is taken from [19].

β	a [fm]	1/a [MeV]
4.00	0.143 ± 0.014	1378 ± 141
4.10	0.113 ± 0.011	1739 ± 177
4.18	0.0957 ± 0.009	2062 ± 210
4.30	0.0747 ± 0.007	2642 ± 270
4.37	0.0649 ± 0.006	3042 ± 310
4.50	0.0511 ± 0.005	3863 ± 394

TABLE 4.3: Lattice spacing and cutoff for given values of β.

$N_s^3 \times N_t$	β	m_{ud}	L_s	# of trajectories
$8^3 \times 16$	4.00	0.01	4	6380
$8^3 \times 16$	4.00	0.01	8	5000
$8^3 \times 16$	4.00	0.01	16	2570
$8^3 \times 16$	4.00	0.025	4	5000
$8^3 \times 16$	4.00	0.05	4	6620
$10^3 \times 24$	4.00	0.01	4	1030
$10^3 \times 24$	4.00	0.01	12	1480
$10^3 \times 24$	4.00	0.025	4	900
$10^3 \times 24$	4.00	0.05	4	1870
$16^3 \times 32$	4.00	0.01	4	800

TABLE 4.4: Ensembles for vacuum QCD spectroscopy. The last row gives the total number of trajectories. Actual measurements start at trajectory #200, with a spacing of 20 trajectories in between measurements.

4.5.1 Configuration generation

Table 4.4 lists the various ensembles for vacuum QCD, which have been generated to verify our simulation setup. The length of the 5th dimension L_s for the domain wall fermions is short, which implies a rather large violation of chirality. In this section the main focus is to setup the simulation and verify a few known properties, the violation of chirality can therefore be neglected. Figure 4.8 shows the Monte Carlo history for the plaquette expectation value

$$\langle U \rangle = \frac{1}{6|\Lambda|} \sum_{x \in \Lambda} \sum_{\nu < \mu} U_{\mu\nu}(x), \tag{150}$$

where $|\Lambda|$ is the number of lattice points in lattice Λ, as well as the iteration count of the conjugate gradient algorithm. From these quantities a sufficient thermalization after ~ 150 trajectories is deduced.

Figure 4.9 shows the topological charge of the gauge field

$$Q = \frac{1}{32\pi^2} \sum_x \epsilon^{\mu\nu\rho\sigma} \mathrm{Tr} G_{\mu\nu}(x) G_{\rho\sigma}(x). \tag{151}$$

Q is measured after removing UV fluctuations by smoothing the gauge field through Wilson flow [86] for a time $ta^2 = 5$. The Wilson flow is generated by infinitesimal steps of stout smearing and keeps local observables gauge invariant. Stout smearing itself can be used as an alternative to smooth the gauge field, as it is described in C.2.

Figures 4.10 and 4.11 show the eigenvalue distribution for different $8^3 \times 16$ lattices.

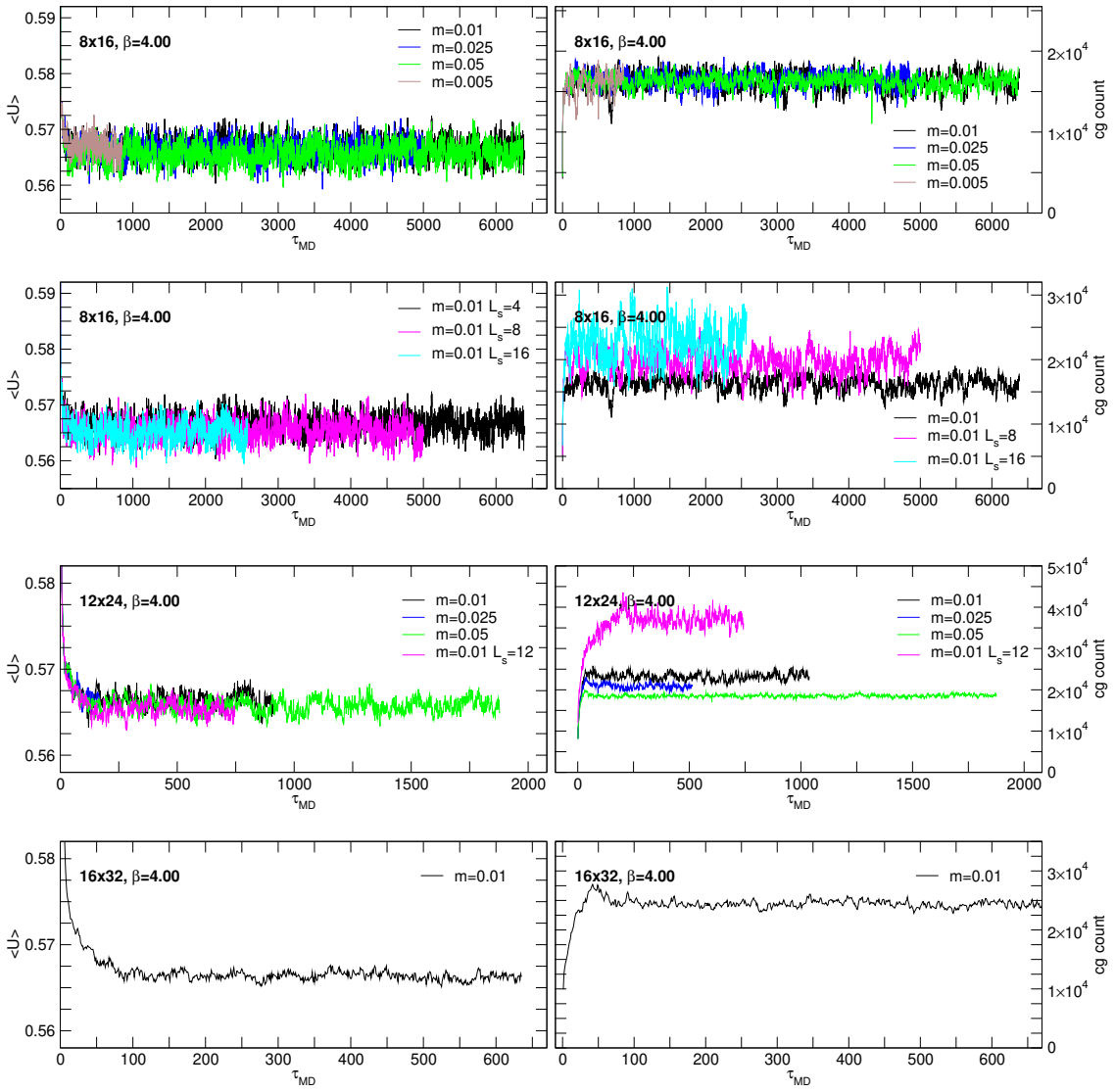

FIGURE 4.8: Monte Carlo history of the plaquette expectation value $\langle U \rangle$ and conjugate gradient iteration (CG) count. The ensembles seem to thermalize after $100 - 150$ trajectories. The CG count of the $12^2 \times 24$ ensemble with higher accuracy of chiral symmetry $L_s = 12$ suggests a slower thermalization.

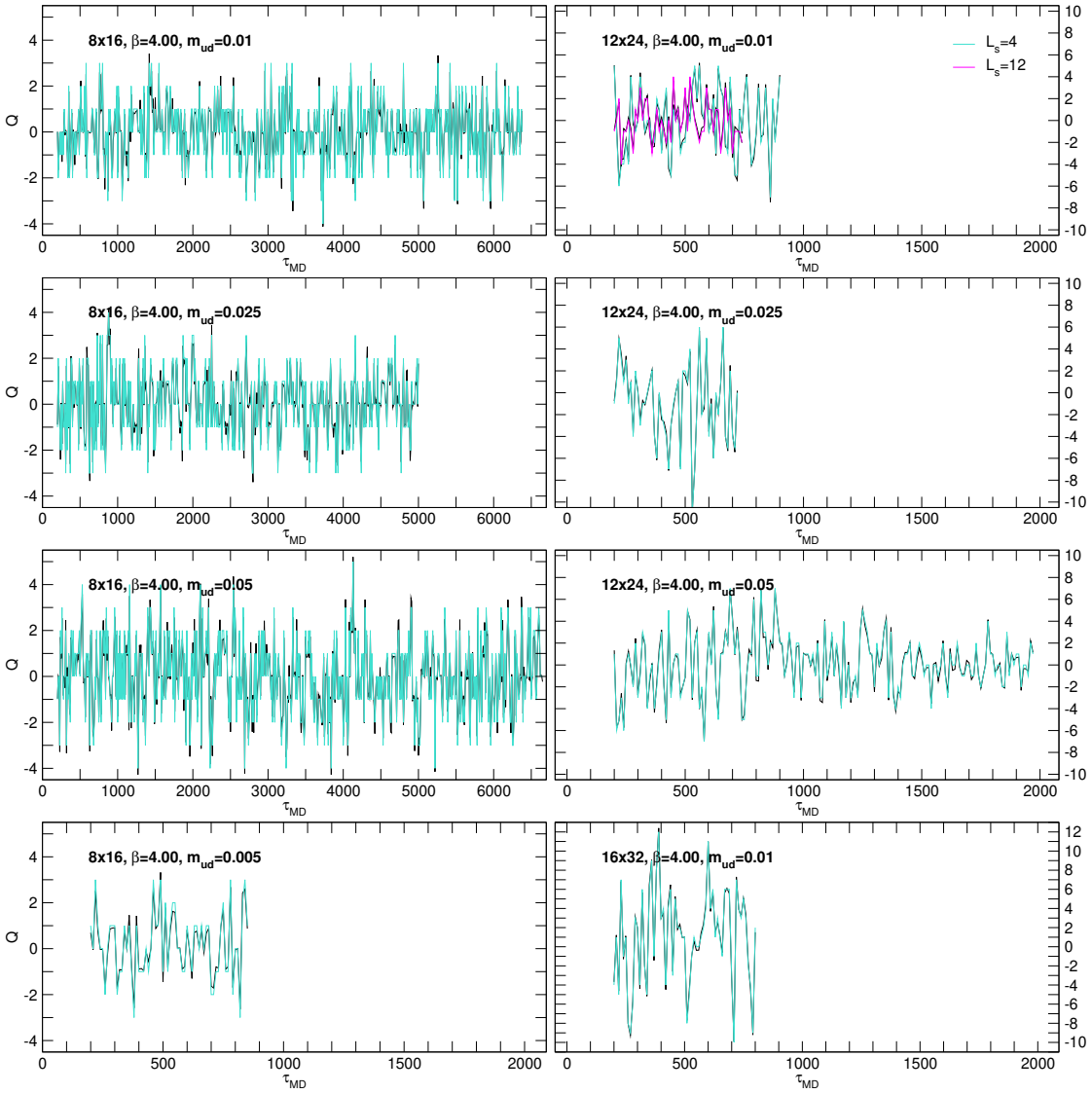

FIGURE 4.9: Monte Carlo history of the topological charge Q. Frequent topological tunneling is observed for all ensembles.

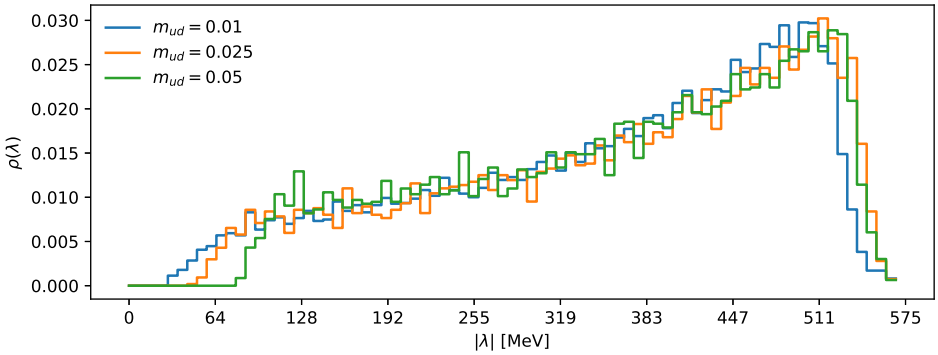

FIGURE 4.10: 40 lowest eigenmodes for $\mathcal{O}(100)$ configurations of 8×16 ensembles, comparing different quark masses.

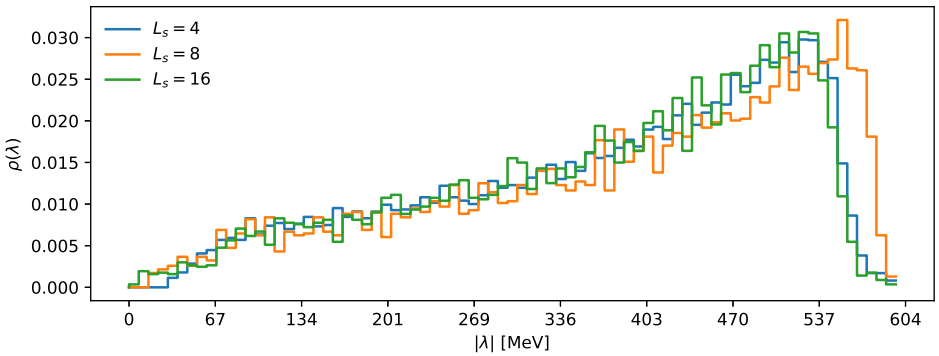

FIGURE 4.11: 40 lowest eigenmodes for $\mathcal{O}(100)$ configurations of 8×16 ensembles, comparing different levels of the domain wall approximation L_s.

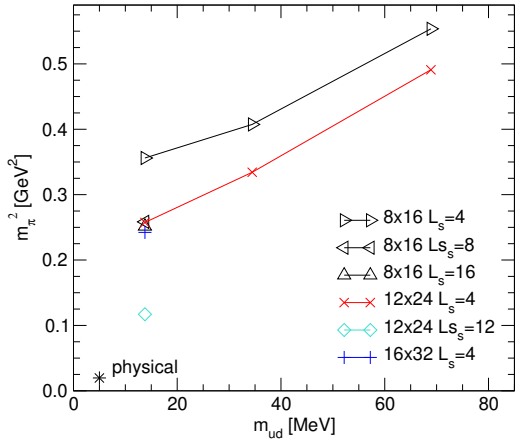

FIGURE 4.12: Gell-Mann–Oaks–Renner relation for the ensembles listed in table 4.4. By comparing the black triangles and red crosses, effects of the finite lattice size are visible. The pion mass for the $16^3 \times 32$ ensemble on the other hand is close to the corresponding $12^2 \times 24$ value, which indicates decreasing finite size errors, *i.e.* the box 'is big enough'. At the same point, increasing L_s and thus improving the approximation of the Ginsparg-Wilson equation, lowers the pion mass substantially.

4.5.2 Meson spectroscopy

For a starting point of hadron spectroscopy, it is instructive to investigate pion masses for the different ensembles, which is done in figure 4.12. The main observables of interest however are correlation functions of local hadronic operators. For isovector mesons they are given by (118), where Γ can be any element of the Clifford algebra. To extract energy levels which correspond to physical states of definite momentum, a *momentum projection*

$$\tilde{O}(\boldsymbol{p}, t) = \frac{1}{\sqrt{|\Lambda_3|}} \sum_{\boldsymbol{x} \in \Lambda_3} O(\boldsymbol{x}, t) e^{-\mathrm{i}a\boldsymbol{x}\boldsymbol{p}} \tag{152}$$

to momentum $\boldsymbol{p}$ has to be done. Due to orthogonality it is sufficient to project one operator of a diagonal correlation function, the second operator can be placed anywhere on the lattice, *e.g.* at the origin $(\mathbf{0}, 0)$. After the momentum projection, a correlation function (116) for a meson of momentum $\boldsymbol{p}$ at time t is given by

$$\langle \tilde{O}(\boldsymbol{p}, t) \bar{O}(\mathbf{0}, 0) \rangle = \frac{1}{\sqrt{|\Lambda_3|}} \sum_{\boldsymbol{x} \in \Lambda_3} e^{-\mathrm{i}a\boldsymbol{x}\boldsymbol{p}} \langle O(\boldsymbol{x}, t) \bar{O}(\mathbf{0}, 0) \rangle \tag{153}$$

and can be evaluated numerically by applying (128).

For the correlation functions of mesons, local currents are essential building blocks. Due to the global symmetries of QCD, a few relations hold for them. They are known as *Ward identities*, a derivation on the lattice can be found *e.g.* in section 11.1.2 of [26]. For a general theory of n_f flavors with τ^a generators in flavor space, they are

$$\partial_\mu \left(\bar{\psi}\gamma_\mu\psi\right) = 0, \tag{154a}$$
$$\partial_\mu \left(\bar{\psi}\gamma_\mu\tau^a\psi\right) = \bar{\psi}[\mathcal{M}, \tau^a]\psi, \tag{154b}$$
$$\partial_\mu \left(\bar{\psi}\gamma_\mu\gamma_5\psi\right) = 2\bar{\psi}\mathcal{M}\gamma_5\psi, \tag{154c}$$
$$\partial_\mu \left(\bar{\psi}\gamma_\mu\gamma_5\tau^a\psi\right) = \bar{\psi}\{\mathcal{M}, \tau^a\}\gamma_5\psi. \tag{154d}$$

Here $\mathcal{M}$ is the mass matrix in flavor space, and for mass degenerate quarks $[\mathcal{M}, \tau^a] = 0$ holds. (154d) is the non-singlet axial Ward identity (AWI), and the axial current (154c) picks up an anomalous term $\mathcal{A}$ due to the axial anomaly:

$$\partial_\mu \left(\bar{\psi}\gamma_\mu\gamma_5\psi\right) = 2\bar{\psi}\mathcal{M}\gamma_5\psi + \mathcal{A}, \quad \mathcal{A} = \frac{1}{32\pi^2}\epsilon^{\mu\nu\rho\sigma}\mathrm{Tr}G_{\mu\nu}G_{\rho\sigma}. \tag{155}$$

Now abbreviating the current in parenthesis of (154a) with V_μ, the following steps can be made

$$\begin{aligned} \partial_t V_t &= -\partial_i V_i \\ \int_\Omega \mathrm{d}^3x \partial_t V_t &= -\int_\Omega \mathrm{d}^3x \partial_i V_i \\ \partial_t \int_\Omega \mathrm{d}^3x V_t &= -\int_{\partial\Omega} \mathrm{d}^2x V_i, \end{aligned} \tag{156}$$

where in the last step *Gauss's theorem* was used to rewrite the volume integral on the right side as surface integral. If we perform this integration over the whole lattice, the flux through the surface is zero and the whole expression vanishes. Therefore,

$$\partial_t \int_\Omega \mathrm{d}^3x V_t = 0. \tag{157}$$

This holds in principle for any (154a)–(154d) as long as the divergence vanishes. Result (157) has implications on the propagating components of corresponding vector mesons, as the integral is usually done during projection to zero momentum. As a consequence, the component orthogonal to the integrated 3-volume, *i.e.* the measurement direction, is constant. Equations (154a)–(154d) hold as expectation values after Monte Carlo averaging, so do these deduced considerations.

Collecting all the methods presented, the zero momentum projected correlation functions at time step t are given by

$$C(t) = \left\langle \tilde{O}_\Gamma(\mathbf{0}, t)\bar{O}_\Gamma(\mathbf{0}, 0)\right\rangle, \tag{158}$$

where the operators are given by

$$O_\Gamma = \bar{d}(x)\Gamma u(x) \tag{159}$$

with gamma structures from table 4.5. The numerical results are given in figure 4.13.

4.5.3 Light baryon spectroscopy

Baryons composed of the light quark flavors *up* and *down* are nucleons and deltas, *cf.* section 2.3. As members of the isospin doublet and quadruplet, respectively, their flavor content differs slightly, which requires for a different treatment on the lattice as it is explained in section 4.3. In the following we focus

abbreviation	Γ	
PS	γ_5	pseudo scalar
S	$\mathbb{1}$	scalar
V	γ_i	vector
A	$\gamma_i\gamma_5$	axial vector
T	$\gamma_i\gamma_4$	tensor vector
X	$\gamma_i\gamma_5\gamma_4$	axial tensor
A_t	$\gamma_5\gamma_4$	
V_t	γ_5	

TABLE 4.5: Gamma structures for local isovector meson operators $O(x) = \bar{d}(x)\Gamma u(x)$. The six components of $\sigma_{\mu\nu} = 1/2[\gamma_\mu, \gamma_\nu]$ are grouped to T and X such that they transform according to representations of the chiral-parity group.

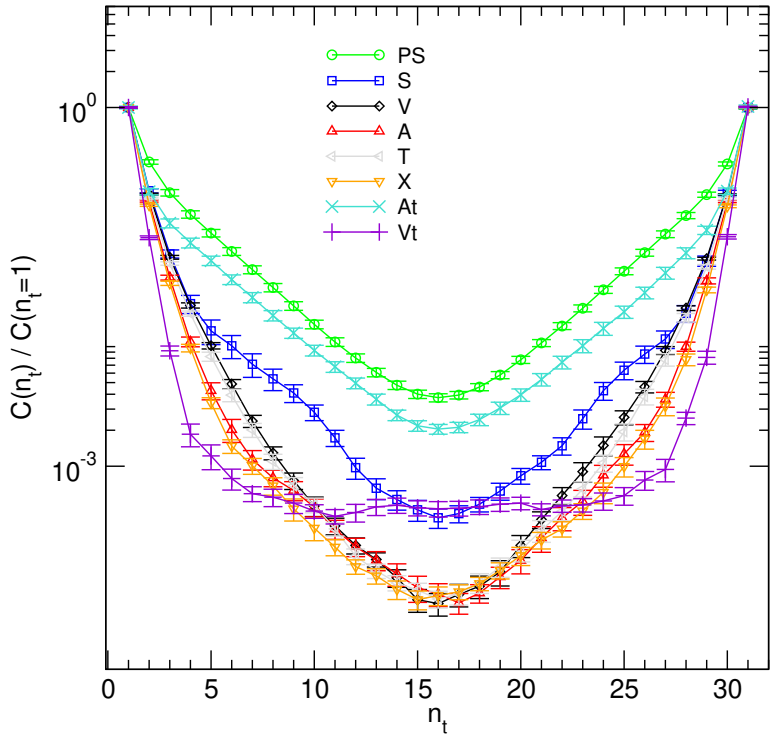

FIGURE 4.13: Zero momentum projected meson correlation functions (158) for the 16×32 ensemble. The operators are (159) with gamma structures from table 4.5. The lightest levels are the pseudoscalar (PS), *i.e.* pion, and the 'time component' of the axial vector meson A_t. In the Nambo-Goldstone mode of chiral symmetry A_t couples to the pseudoscalar channel. The 'time component' of the vector meson V_t does not propagate, according to considerations (157). The vectors V, A, T and X show similar slopes, and it would require better statistics and handling of systematic errors to disentangle the energy levels. The scalar channel S shows no exponential decay at all and no information can be extracted with this level of statistics.

abbreviation	Γ_1
D_1	$C\gamma_5$
D_2	C
D_3	$C\gamma_5\gamma_4$
D_4	$C\gamma_4$
D_5	$C\gamma_5\gamma_3$
D_6	$C\gamma_3$

TABLE 4.6: Diquark gamma structures of nucleon operators. $C = \mathrm{i}\gamma_2\gamma_4$ is the standard charge conjugation matrix with properties $C = C^{-1} = C^\dagger = -C^T$.

on nucleons only. The basic operators are

$$N_k(x) = \epsilon_{abc} u_a(x) \left[u_b^T(x) D_k d_c(x) \right], \tag{160}$$

where the expression in square brackets is the diquark with a gamma structure D_k. The different D_k's used in this study are listed in table 4.6. The single quark outside the brackets is sometimes referred to as *passenger quark*. The operators (160) are not invariant under parity transformations and mix positive and negative parity. It is therefore necessary to project them to definite parity with operators

$$\mathcal{P}_\pm = \mathcal{P}_\pm^t = \frac{1}{2}\left(1 \pm \gamma_4\right). \tag{161}$$

Here the superscript t explicitly denotes the parity projection in time direction. It is also possible to define a similar projection operator

$$\mathcal{P}_\pm^z = \frac{1}{2}\left(1 \pm \gamma_3\right), \tag{162}$$

which will be useful for studying spatial correlations in z-direction. In principle it is also possible to include an additional gamma structure for the passenger quark. For diagonal correlators however this is of minor importance: a short modification of (130) shows that as long as this additional gamma structure anti commutes with the parity projector, the parity states exchange, *i.e.* $N^+ \leftrightarrow N^-$. We take this effect into account to construct operators, which are natural parity partners and can be rotated into each other by $\mathrm{U}(1)_A$ transformations:

$$N_1^\pm \overset{\mathrm{U}(1)_A}{\longleftrightarrow} N_2^\pm \tag{163a}$$

$$N_3^\pm \overset{\mathrm{U}(1)_A}{\longleftrightarrow} N_4^\pm \tag{163b}$$

$$N_5^\pm \overset{\mathrm{U}(1)_A}{\longleftrightarrow} N_6^\pm \tag{163c}$$

Operators N_1, N_2 and N_3 have been used previously in literature to extract the nucleon ground states with various success. For a discussion on the quantum numbers and physical overlaps of this operators, the reader is referred to [87] and the discussion therein. For the operators N_4, N_5 and N_6 the behaviour is a priori not clear. Due to the $J = 1$ diquark, the operators N_5 and N_6 *e.g.* couple to $J = 1/2$ and $J = 3/2$ channels and would require spin projection to extract physical states. However, as the main interest here are symmetry properties of correlation functions, the asymptotic behaviour to extract masses is of minor interest.

The results for parity projected N_1–N_6 operators are shown in figure 4.14. A comparison of parity and z-projected states of the N_1 operator is shown in figure 4.15. As for the high temperature study spatial correlations in z-direction will be of interest, the corresponding data of the N_1 operator is shown for the vacuum in figure 4.16, again for parity projected as well as z-projected states.

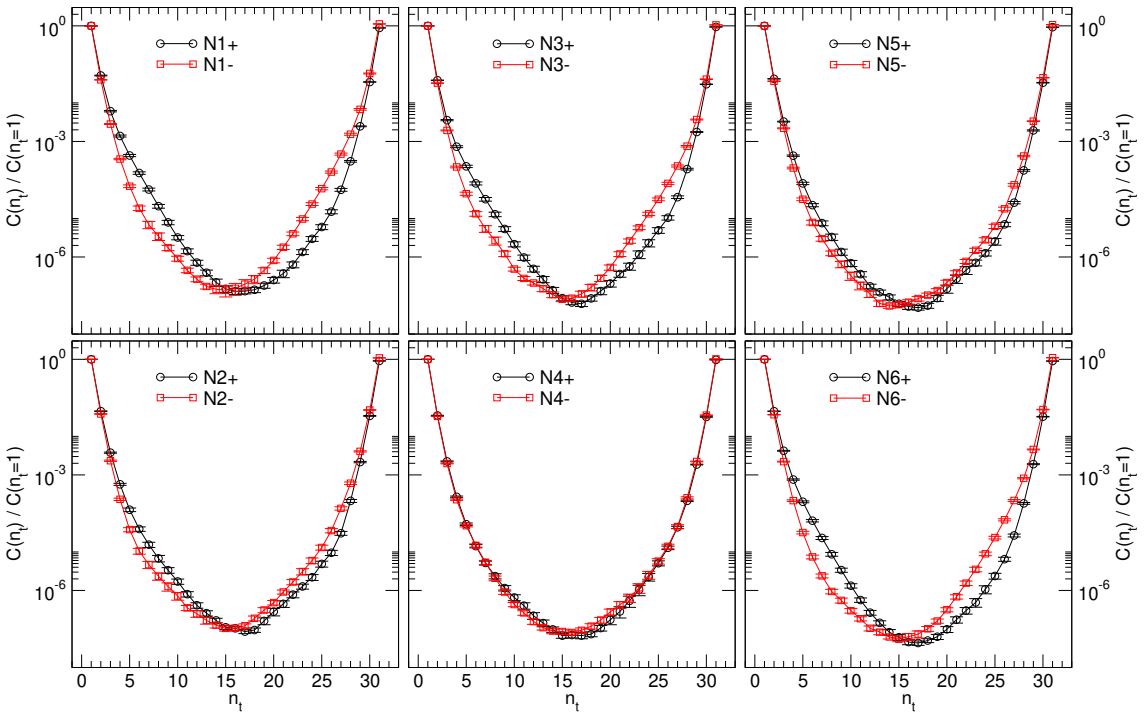

FIGURE 4.14: Normalized nucleon correlations for the 16×32 ensemble. Parity splitting is well pronounced for the N_1, N_3 and N_6 operators: For the N_1^+ channel *e.g.* the positive parity nucleon can be seen propagating forward while the negative parity nucleon is propagating backwards, and vice versa for the N_1^- channel.

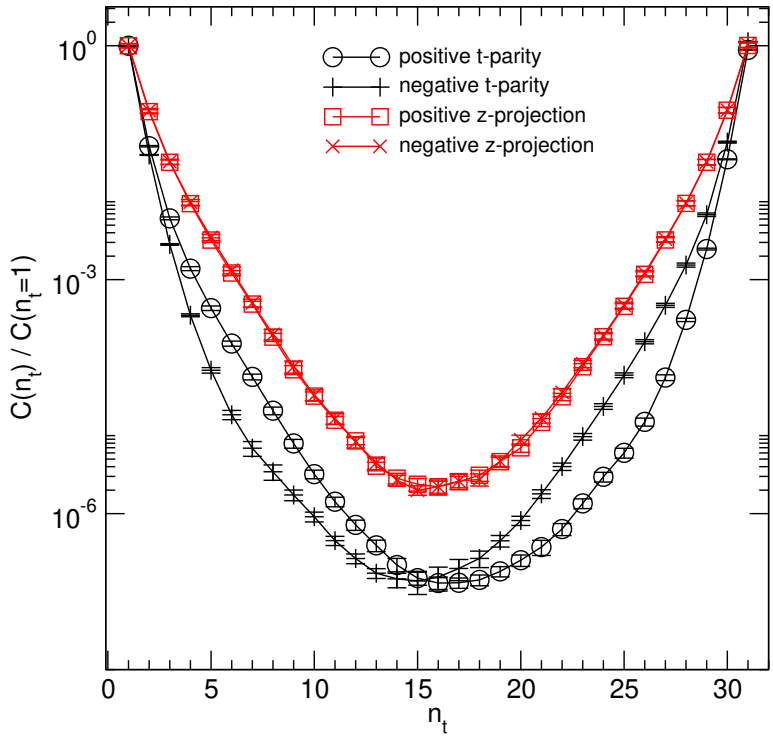

FIGURE 4.15: Normalized N_1 nucleon with different projections for correlations in time direction. Parity splitting can be seen for $\mathcal{P}_\pm^t$ projected operators.

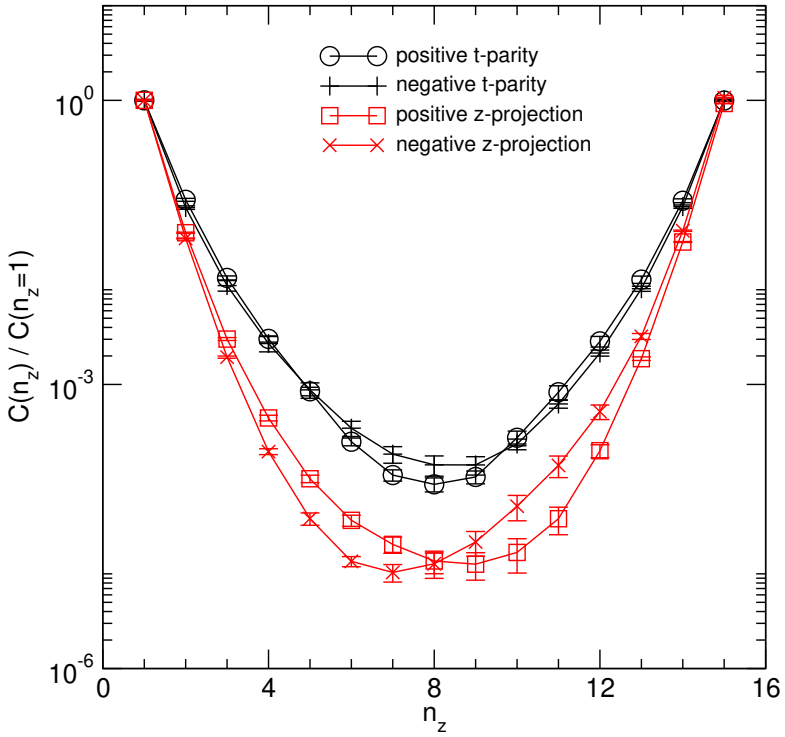

FIGURE 4.16: Normalized N_1 nucleon with different projections for spatial correlations. Clear splitting can be seen for $\mathcal{P}^z_\pm$ projected operators.

Chapter 5

Lattice QCD at high temperatures

In section 2.5 the path integral (39) was introduced, where field configurations are summed up with a statistical weight (40). The weight itself contains the Euclidean action, which is a 4-dimensional integral of the lagrangian density. A possible reinterpretation of this integral is

$$S[\Phi] = \int_0^\beta \mathrm{d}t \int \mathrm{d}^3x \; \mathcal{L}(\Phi(t, \boldsymbol{x}), \partial_\mu \Phi(t, \boldsymbol{x})), \tag{164}$$

with β being the inverse temperature $\beta = 1/T$. By this interpretation[1] the temperature T of the system is linked to the lattice extend in time direction

$$\frac{1}{T} = aN_t. \tag{165}$$

As the statistical sampling is not changed, the whole formalism of Monte Carlo lattice QCD stays the same, and just the interpretation changes by identifying the time extend of the lattice with the inverse temperature. For the limit $T \to 0$ the time extend aN_t becomes infinite and the vacuum interpretation is recovered, where both ends of the lattice in time direction are identified as $-\infty < t < \infty$.

As the lattice of the simulation is finite, this difference is a source of systematic errors. Being interested in asymptotic behaviour of observables, one usually tries to keep the time extend large. Applying the finite temperature interpretation, the systematic error linked with finite time extend requires rethinking.

Increasing the gauge coupling β gives a shorter lattice constant a and smaller spatial volumes. Therefore, the continuum limit is generally done by driving $a \to 0$ while keeping the volume fixed. Now for a fixed value of a the scale of the theory is given by the temperature T, *i.e.* $1/aN_t$. Also keeping the temperature T fixed, the 3-volume at each time step is now given by N_s^3. For fixed temperature $1/aN_t$, a larger spatial extend aN_s will obviously lead to less finite volume effects. Thus the *aspect ratio* N_s/N_t becomes significant: higher values of N_s/N_t have less systematic errors. One can counteract this effect by introducing anisotropic lattices.

In section 5.1 the high temperature lattice setup is introduced. Section 5.2 treats correlations for non-interacting fermions as reference for the lattice data. In sections 5.3 and 5.4 the lattice data for correlations functions of mesons and baryons is presented. Due to the setup of the high temperature study and the considerations above, we will focus on spatial correlations of the hadronic spectrum. This provides a lot more lattice points to study and due to the high aspect ratio $N_s/N_t \geq 4$ less systematic errors, as tradeoff the physical interpretation of the correlation function's slopes as effective masses is lost.

[1] This is the conventional notation. However, β as temperature is not the same as β describing the inverse coupling $\beta = 6/g^2$. To avoid confusion, we will use β for the single purpose of the latter case and refer to the temperature simply as T.

N_t	$\beta = 4.10$	$\beta = 4.18$	$\beta = 4.30$	$\beta = 4.37$	$\beta = 4.50$
16	108 ± 1	129 ± 1	165 ± 2	189 ± 2	241 ± 5
14	124 ± 1	147 ± 1	189 ± 2	216 ± 3	275 ± 5
12	144 ± 1	172 ± 1	220 ± 2	253 ± 4	321 ± 6
10	173 ± 1	206 ± 2	264 ± 3	303 ± 4	385 ± 7
8	217 ± 2	258 ± 2	330 ± 3	379 ± 5	482 ± 9
6	289 ± 2	344 ± 2	440 ± 4	505 ± 6	642 ± 11
4	433 ± 3	516 ± 3	660 ± 6	758 ± 10	963 ± 17

TABLE 5.1: Temperatures in MeV for combinations of β and N_t according to (165).

5.1 Setup

For the high temperature study the same basic setup is used as described in section 4.5. Using the lattice spacings and cutoffs listed in table 4.3, the corresponding temperatures can be calculated using (165). The temperatures for various combinations of N_t and β are given in table 5.1. In [19] the critical temperature for this setup was determined by the Polyakov loop[2] as

$$T_c = 175 \pm 5\text{MeV}. \tag{166}$$

The ensembles for the high temperature study are listed in table 5.2. The approximation of Overlap fermions through domain wall fermions is controlled by varying L_s, as explained in section 4.2.2. Here L_s is chosen such that the violation of the Ginsparg-Wilson equation (97) is characterized by a residual quark mass $m_{res} \simeq 0.5$ MeV, which is neglectable compared to the explicit breaking by non-vanishing quark masses. From figure 5.1 it can be seen that short-range observables represented by the plaquette expectation value $\langle U \rangle$ thermalize for all ensembles after 150 trajectories.

Figure 5.2 shows the topological charge for the high temperature ensembles, calculated accoring to (151). All ensembles in this plot correspond to temperatures above $2T_c$. For this temperatures the trivial topological sector $Q = 0$ is dominating. Long-range observables as correlation functions with no obvious connection to the topological charge should not be affected by this fact. In [83] the pion mass has been calculated for different topological sectors and the deviation to the global average has been found to be negligible. Thus we conclude the dominance of $Q = 0$ not to be a problem.

Lastly a short glance at the eigenvalue distribution is given in figure 5.3. The eigenvalue distribution for ensembles with lower temperatures closer to the critical temperature can be found in [19, 20]. While the limited amount of collected statistics does not allow for solid conclusions, it can clearly be seen that the bulk of eigenmodes starts at increasingly higher energies and a *gap* seems to open up. This data represents eigenmodes from the $Q = 0$ sector and according to (69) do not contain zero modes.

5.2 Spatial correlations for non-interacting fermions

We are interested in the general correlation of two non-interacting quarks with momenta

$$p = (p_x, p_y, p_z, p_t), \tag{167a}$$
$$q = (q_x, q_y, q_z, q_t). \tag{167b}$$

[2] The term *critical temperature* hereby refers to the role of the Polyakov loop as order parameter for Z_3 center symmetry in pure gauge theory, *cf.* section 2.5.2 for a short discussion.

$N_s^3 \times N_t$	β	m_{ud}	L_s	T [MeV]	# of trajectories
$32^3 \times 8$	4.37	0.001	12	380	770
$32^3 \times 8$	4.37	0.005	12	380	1540
$32^3 \times 8$	4.37	0.01	12	380	470
$32^3 \times 8$	4.50	0.001	12	480	1520
$32^3 \times 8$	4.50	0.005	12	480	1480
$32^3 \times 8$	4.50	0.01	12	480	1170
$32^3 \times 6$	4.30	0.001	12	440	2730
$32^3 \times 6$	4.30	0.005	12	440	2740
$32^3 \times 6$	4.30	0.01	12	440	2920
$32^3 \times 4$	4.30	0.001	10	660	2080
$32^3 \times 4$	4.30	0.005	10	660	1820
$32^3 \times 4$	4.30	0.01	10	660	2120
$32^3 \times 4$	4.50	0.001	10	960	2090
$32^3 \times 4$	4.50	0.005	10	960	2000
$32^3 \times 4$	4.50	0.01	10	960	2000
$32^3 \times 12$	4.30	0.001	24	220	226
$32^3 \times 12$	4.30	0.01	12	220	142
$32^3 \times 8$	4.10	0.001	24	220	800
$32^3 \times 8$	4.10	0.005	24	220	80
$32^3 \times 8$	4.10	0.01	12	220	80
$32^3 \times 8$	4.18	0.001	12	260	320
$32^3 \times 8$	4.18	0.005	12	260	120
$32^3 \times 8$	4.18	0.01	12	260	234
$32^3 \times 8$	4.30	0.001	12	330	260
$32^3 \times 8$	4.30	0.005	12	330	317
$32^3 \times 8$	4.30	0.01	12	330	330
$32^3 \times 8$	4.37	0.005	12	380	120

TABLE 5.2: Dynamical $n_f = 2$ domain wall fermion ensembles for high temperature use. L_s gives the length of the 5th dimension. Ensembles below the horizontal separator have been generated for a different study, but are included in the measurements for mesons correlation functions.

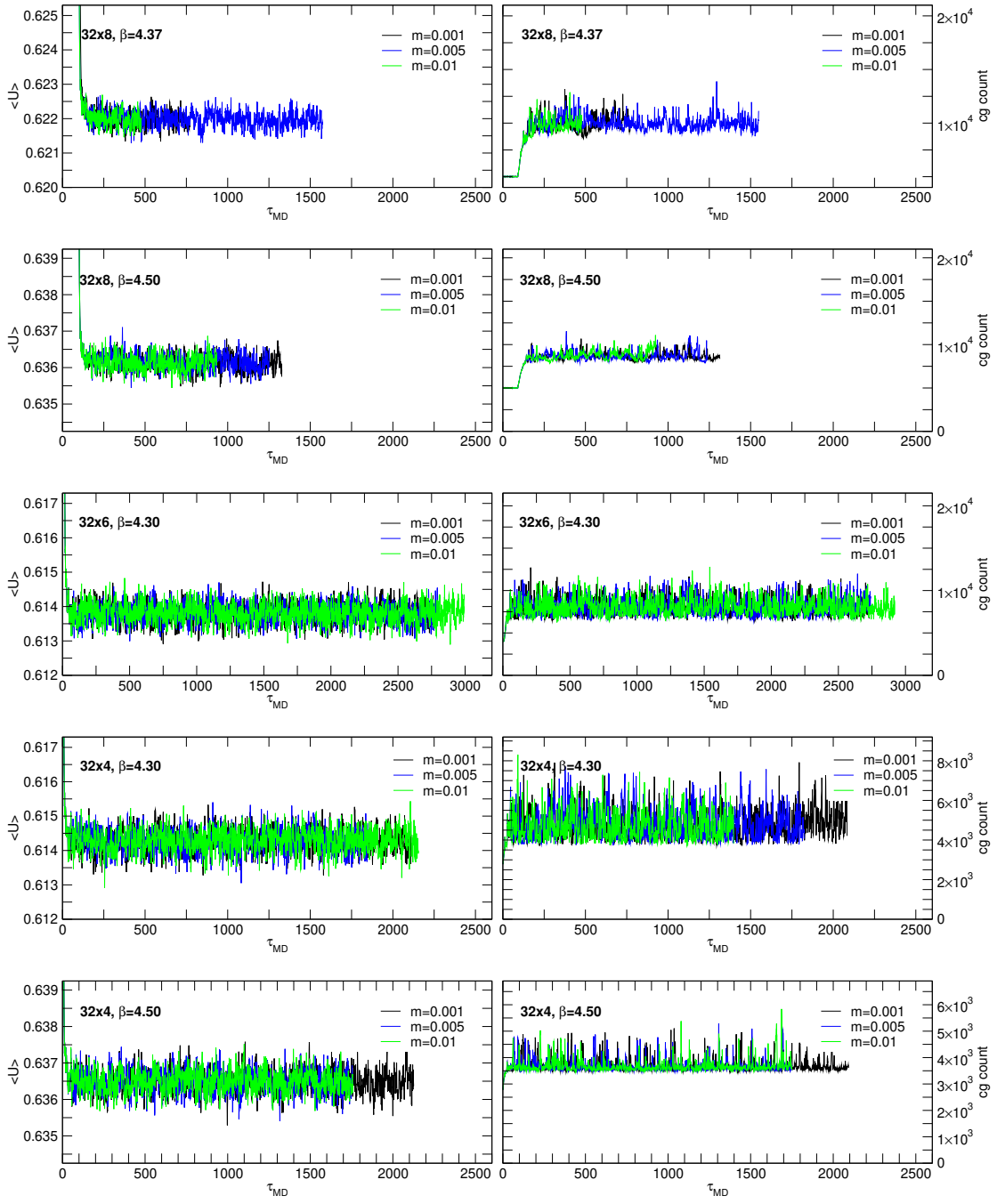

FIGURE 5.1: Monte Carlo history of the plaquette expectation value $\langle U \rangle$ according to (150) on the left side, and conjugate gradient iteration count on the right side.

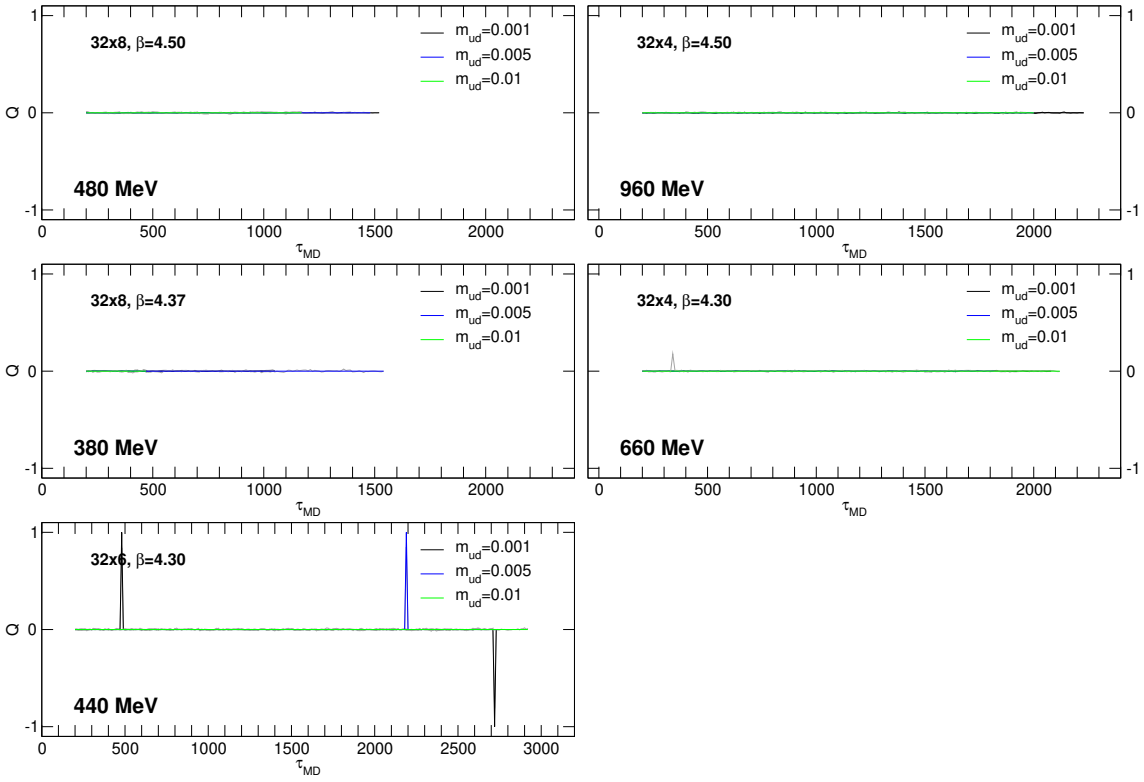

FIGURE 5.2: Monte Carlo history of the topological charge Q calculated according to (151). For the $N_t = 8$ and $N_t = 4$ ensembles all configurations lie in the trivial $Q = 0$ topological sector, for the $N_t = 6$ ensembles there are single configurations in the $Q = \pm 1$ sector. The effect of *topological freezing* is a well-known phenomenon at high temperatures.

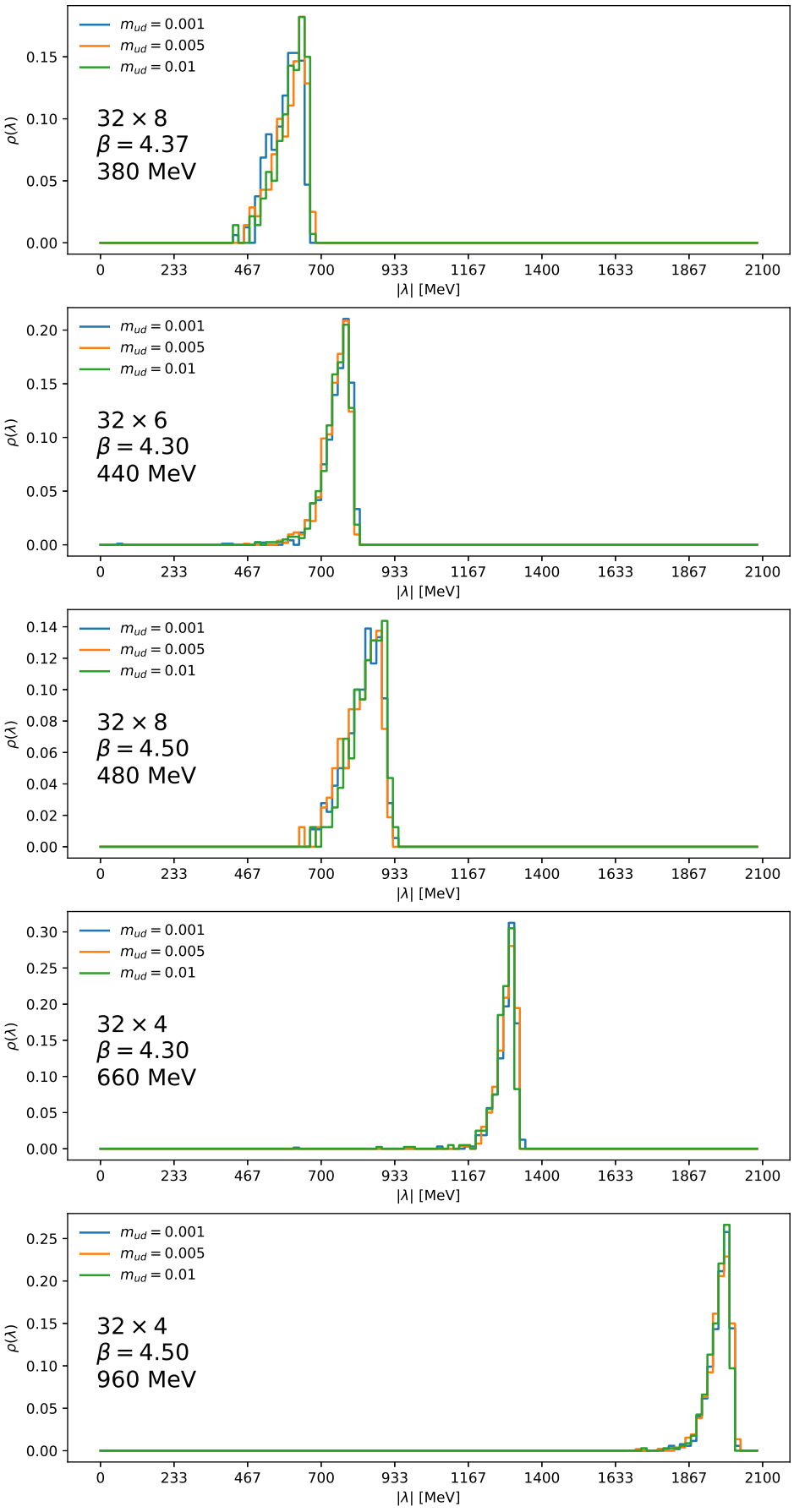

FIGURE 5.3: Eigenvalue distribution for ensembles of table 5.2. The histogram includes the lowest 40 eigenvalues for $\mathcal{O}(10)$ configurations. The beginning of the bulk of eigenmodes shifts towards higher energies. Due to the very limited statistics this plots might not be representative.

A composed state of this quarks is described by

$$\mathrm{Tr}\left[\Gamma\frac{1}{\not{p}+m}\Gamma\frac{1}{\not{q}+m}\right], \tag{168}$$

where m is the quark mass and Γ is an element of the Clifford algebra determining the quantum numbers of the state. Now spatial correlations in z-direction are measured by Fourier transforming the z-components

$$C(p_x,p_y,p_t,q_x,q_y,q_t,z)=\int\frac{dp_z}{2\pi}e^{\mathrm{i}p_z z}\int\frac{dq_z}{2\pi}e^{\mathrm{i}q_z z}\ \mathrm{Tr}\left[\Gamma\frac{1}{\not{p}+m}\Gamma\frac{1}{\not{q}+m}\right], \tag{169}$$

while the remain momenta are still open. We can extend the denominators in the trace and the integrand reads

$$\mathrm{Tr}\left[\Gamma\frac{-\gamma_1 p_x-\gamma_2 p_y-\gamma_3 p_z-\gamma_4 q_t+m}{p_x^2+p_y^2+p_z^2+q_t^2+m^2}\Gamma\frac{-\gamma_1 q_x-\gamma_2 q_y-\gamma_3 q_z-\gamma_4 q_t+m}{q_x^2+q_y^2+q_z^2+q_t^2+m^2}\right]. \tag{170}$$

Assigning the second quark momenta in opposite direction $q\to -q$ gives

$$\mathrm{Tr}\left[\Gamma\frac{-\gamma_1 p_x-\gamma_2 p_y-\gamma_3 p_z-\gamma_4 q_t+m}{p_x^2+p_y^2+p_z^2+q_t^2+m^2}\Gamma\frac{\gamma_1 q_x+\gamma_2 q_y+\gamma_3 q_z+\gamma_4 q_t+m}{q_x^2+q_y^2+q_z^2+q_t^2+m^2}\right]. \tag{171}$$

The evaluation of the trace depends on the gamma structure Γ. As an example we proceed using the pseudo scalar $\Gamma=\gamma_5$ structure. Anti commuting γ_5 through the nominator changes signs of some terms

$$\mathrm{Tr}\left[\frac{+\gamma_1 p_x+\gamma_2 p_y+\gamma_3 p_z+\gamma_4 q_t+m}{(p_z^2+M^2)}\frac{\gamma_1 q_x+\gamma_2 q_y+\gamma_3 q_z+\gamma_4 q_t+m}{(q_z^2+M'^2)}\right], \tag{172}$$

where the shorthand notation $M^2=p_x^2+p_y^2+p_t^2+m^2$ and $M'^2=q_x^2+q_y^2+q_t^2+m^2$ has been introduced. Evaluating the trace yields

$$4\int\frac{dp_z}{2\pi}e^{\mathrm{i}p_z z}\int\frac{dq_z}{2\pi}e^{\mathrm{i}q_z z}\ \frac{p_xq_x+p_yq_y+p_zq_z+p_tq_t+m^2}{(p_z^2+M^2)(q_z^2+M'^2)} \tag{173}$$

as expression for the correlation (169). Evaluating the first integral at $p_z=iM$ this becomes

$$4\frac{1}{2M}e^{-Mz}\int\frac{dq_z}{2\pi}e^{-iq_z z}\quad\frac{p_xq_x+p_yq_y+iMq_z+p_tq_t+m^2}{(q_z^2+M'^2)}, \tag{174}$$

and evaluating $q_z=-iM$ we arrive at

$$4\frac{1}{4MM'}e^{-(M+M')z}(p_xq_x+p_yq_y+MM'+p_tq_t+m^2). \tag{175}$$

Using the equality of momenta $q=p$ implies $M=M'$ and the correlation becomes

$$C(p_x,p_y,p_t,z)=\frac{1}{M^2}(p_x^2+p_y^2+M^2+p_t^2+m^2)e^{-2Mz} \tag{176}$$

for the pseudo scalar state $\Gamma=\gamma_5$. The change of signs in (172) obviously depends on the choice of Γ and affects result (176). A list of gamma structures, a corresponding shorthand notation and the resuling nominator for (172) are listed in table 5.3. Following the steps above for the gamma structures Γ of

Γ	abbreviation	nominator
γ_5	PS	$+p_xq_x + p_yq_y + p_zq_z + p_tq_t + m^2$
$\mathbb{1}$	S	$-p_xq_x - p_yq_y - p_zq_z - p_tq_t + m^2$
γ_1	V_x	$-p_xq_x + p_yq_y + p_zq_z + p_tq_t + m^2$
γ_2	V_y	$+p_xq_x - p_yq_y + p_zq_z + p_tq_t + m^2$
γ_3	V_z	$+p_xq_x + p_yq_y - p_zq_z + p_tq_t + m^2$
γ_4	V_t	$+p_xq_x + p_yq_y + p_zq_z - p_tq_t + m^2$
$\gamma_1\gamma_3$	T_x	$+p_xq_x - p_yq_y + p_zq_z - p_tq_t + m^2$
$\gamma_2\gamma_3$	T_y	$-p_xq_x + p_yq_y + p_zq_z - p_tq_t + m^2$
$\gamma_4\gamma_3$	T_t	$-p_xq_x - p_yq_y + p_zq_z + p_tq_t + m^2$

TABLE 5.3: Nominator for the trace expression in (172) The given shorthand notation is specificly used for measurements in $z-$direction.

table 5.3, the z-correlations in dependence of z and the momentum $\tilde{\boldsymbol{p}} = (p_x, p_y, p_t)$ can be calculated:

$$C_{PS}(\tilde{\boldsymbol{p}}, z) = 2\frac{p_x^2 + p_y^2 + p_t^2 + m^2}{M^2}\, e^{-2Mz} \tag{177a}$$

$$C_{S}(\tilde{\boldsymbol{p}}, z) = 2\frac{p_x^2 + p_y^2 + p_t^2}{M^2}\, e^{-2Mz} \tag{177b}$$

$$C_{Vx}(\tilde{\boldsymbol{p}}, z) = 2\frac{p_x^2 + p_t^2 + m^2}{M^2}\, e^{-2Mz} \tag{177c}$$

$$C_{Vy}(\tilde{\boldsymbol{p}}, z) = 2\frac{p_y^2 + p_t^2 + m^2}{M^2}\, e^{-2Mz} \tag{177d}$$

$$C_{Vz}(\tilde{\boldsymbol{p}}, z) = 0 \tag{177e}$$

$$C_{Vt}(\tilde{\boldsymbol{p}}, z) = 2\frac{p_x^2 + p_y^2 + m^2}{M^2}\, e^{-2Mz} \tag{177f}$$

$$C_{Tx}(\tilde{\boldsymbol{p}}, z) = 2\frac{p_x^2 + m^2}{M^2}\, e^{-2Mz} \tag{177g}$$

$$C_{Ty}(\tilde{\boldsymbol{p}}, z) = 2\frac{p_y^2 + m^2}{M^2}\, e^{-2Mz} \tag{177h}$$

$$C_{Tt}(\tilde{\boldsymbol{p}}, z) = 2\frac{p_t^2 + m^2}{M^2}\, e^{-2Mz} \tag{177i}$$

There are a few interesting observations from this results. The overall expressions depend on the momenta p_x, p_y, and p_t. The exponential decay is always determined by the momenta implicitly in M, and for a given set of momenta the same in all channels. The amplitude on the other hand is unique for each cannel, and depends on the different momenta. A few exemplary scenarios of possible combinations of momenta are given in table 5.4. The complete correlation function however is a sum over all possible momenta, and thus a sum of different exponentials.

Correlations in temporal direction can be derived in a similar fashion by defining

$$C(p_x, p_y, p_z, q_x, q_y, q_z, t) = \int \frac{dp_t}{2\pi} e^{ip_t t} \int \frac{dq_t}{2\pi} e^{iq_t t} \quad \mathrm{Tr}\left[\Gamma \frac{1}{\not{p} + m} \Gamma \frac{1}{\not{q} + m}\right]. \tag{178}$$

Adapting the considerations on spatial correlation functions from above and using the modified shorthand notation given in table 5.5, the following expressions for measurements in t-direction, now depend-

	$p_x = p_y = 0$	$p_x \neq p_y = 0$	$p_x \neq p_y \neq 0$
PS	$p_t^2 + m^2$	$p_x^2 + p_t^2 + m^2$	$p_x^2 + p_y^2 + p_t^2 + m^2$
S	p_t^2	$p_x^2 + p_t^2$	$p_x^2 + p_y^2 + p_t^2$
V_x	$p_t^2 + m^2$	$p_x^2 + p_t^2 + m^2$	$p_x^2 + p_t^2 + m^2$
V_t	m^2	$p_x^2 + m^2$	$p_x^2 + p_t^2 + m^2$
T_x	m^2	$p_x^2 + m^2$	$p_x^2 + m^2$
T_t	$p_t^2 + m^2$	$p_t^2 + m^2$	$p_t^2 + m^2$

TABLE 5.4: Amplitude of the exponential decay for different scenarios without the common factor $2/M^2$.

Γ	abbreviation	nominator
γ_5	PS	$+p_xq_x + p_yq_y + p_zq_z + p_tq_t + m^2$
$\mathbb{1}$	S	$-p_xq_x - p_yq_y - p_zq_z - p_tq_t + m^2$
γ_1	V_x	$-p_xq_x + p_yq_y + p_zq_z + p_tq_t + m^2$
γ_2	V_y	$+p_xq_x - p_yq_y + p_zq_z + p_tq_t + m^2$
γ_3	V_z	$+p_xq_x + p_yq_y - p_zq_z + p_tq_t + m^2$
γ_4	V_t	$+p_xq_x + p_yq_y + p_zq_z - p_tq_t + m^2$
$\gamma_1\gamma_4$	T_x	$+p_xq_x - p_yq_y - p_zq_z + p_tq_t + m^2$
$\gamma_2\gamma_4$	T_y	$-p_xq_x + p_yq_y - p_zq_z + p_tq_t + m^2$
$\gamma_3\gamma_4$	T_z	$-p_xq_x - p_yq_y + p_zq_z + p_tq_t + m^2$

TABLE 5.5: Nominator for the trace expression in (172) when evaluating t-correlations. The given shorthand notation is specificly used for measurements in $t-$direction.

ing on the momentum $\boldsymbol{p} = (p_x, p_y, p_z)$, can be derived:

$$C_{PS}(\boldsymbol{p}, t) = 2\frac{p_x^2 + p_y^2 + p_z^2 + m^2}{M^2}\, e^{-2Mt} \tag{179a}$$

$$C_{S}(\boldsymbol{p}, t) = 2\frac{p_x^2 + p_y^2 + p_z^2}{M^2}\, e^{-2Mt} \tag{179b}$$

$$C_{V_x}(\boldsymbol{p}, t) = 2\frac{p_y^2 + p_z^2 + m^2}{M^2}\, e^{-2Mt} \tag{179c}$$

$$C_{V_y}(\boldsymbol{p}, t) = 2\frac{p_x^2 + p_z^2 + m^2}{M^2}\, e^{-2Mt} \tag{179d}$$

$$C_{V_z}(\boldsymbol{p}, t) = 2\frac{p_x^2 + p_y^2 + m^2}{M^2}\, e^{-2Mt} \tag{179e}$$

$$C_{V_t}(\boldsymbol{p}, t) = 0 \tag{179f}$$

$$C_{T_x}(\boldsymbol{p}, t) = 2\frac{p_x^2 + m^2}{M^2}\, e^{-2Mt} \tag{179g}$$

$$C_{T_y}(\boldsymbol{p}, t) = 2\frac{p_y^2 + m^2}{M^2}\, e^{-2Mt} \tag{179h}$$

$$C_{T_z}(\boldsymbol{p}, t) = 2\frac{p_z^2 + m^2}{M^2}\, e^{-2Mt} \tag{179i}$$

As it can be seen for spatial (177a–177b) as well temporal (179a–179b) correlations, a non-vanishing mass term m is the only source of difference between pseudo scalar and scalar correlations, which is in agreement with expectations from $\mathrm{U}(1)_A$ symmetry transformations of massless non-interacting quarks. Furthermore, the correlations for channels (177e) and (179f) vanish according to considerations (157). For

a rotational invariant system, where p_x and p_y occur in equal amounts, the channels V_x and V_y coincide, as well as T_x and T_y.

The asymptotic properties of full momentum integrated correlation functions for non-interacting massless quarks have been extracted in [88]. For correlations in z-direction they fall into five different classes, where the behaviour of parity partners coincide. Using the lowest Matsubara frequency of the quarks $w_0 = \pi/\beta$, they can be written as

$$C_{PS}(z) = \frac{(2\pi)^4}{\beta^2}\frac{e^{-z2\omega_0}}{z2\omega_0}\left[1+\frac{1}{z2\omega_0}\right] + \mathcal{O}(\frac{e^{-z4\omega_0}}{z}), \tag{180a}$$

$$C_{V_x}(z) = \frac{(2\pi)^4}{\beta^2}\frac{e^{-z2\omega_0}}{z2\omega_0}\left[1+\frac{1}{(z2\omega_0)^2}+...\right] + \mathcal{O}(\frac{e^{-z4\omega_0}}{z}), \tag{180b}$$

$$C_{V_t}(z) = 2\frac{(2\pi)^4}{\beta^2}\frac{e^{-z2\omega_0}}{(z2\omega_0)^2}\left[1-\frac{1}{z2\omega_0}+...\right] + \mathcal{O}(\frac{e^{-z4\omega_0}}{z}), \tag{180c}$$

$$C_{T_x}(z) = \frac{(2\pi)^4}{\beta^2}\frac{e^{-z2\omega_0}}{(z2\omega_0)^2}\left[1-\frac{1}{z2\omega_0}+...\right] + \mathcal{O}(\frac{e^{-z4\omega_0}}{z}), \tag{180d}$$

$$C_{T_t}(z) = \frac{(2\pi)^4}{\beta^2}\frac{e^{-z2\omega_0}}{z2\omega_0}\left[1-\frac{1}{z2\omega_0}+...\right] + \mathcal{O}(\frac{e^{-z4\omega_0}}{z}). \tag{180e}$$

5.3 Mesons

The following data has been published in [89–91]. Here we summarize the findings. As stated in the introduction, spatial correlations are of interest in this study. This requires a slight modification in the setup. Namely, the calculation of correlations in z-direction is done by

$$C(z) = \langle \tilde{O}_\Gamma(\tilde{\mathbf{0}}, z)\bar{O}_\Gamma(\mathbf{0}, 0)\rangle\,, \tag{181}$$

where the momentum projection (152) now projects the meson state to zero momentum

$$\tilde{\boldsymbol{p}} = (p_x, p_y, p_t) = (0, 0, 0). \tag{182}$$

The operators itself (159) are not modified. As the rotational invariance of the lattice is broken in the finite temperature setup, the choice of gamma structures Γ for operators and components requires special care. The pseudo scalar and scalar operators stay the same

$$PS = \gamma_5, \tag{183a}$$

$$S = \mathbb{1}. \tag{183b}$$

Due to the non-propagation of $V_z = \gamma_3$ according to (157), the components of the vector meson and axial vector meson state are

$$\mathbf{V} = \begin{pmatrix} \gamma_1 = V_x \\ \gamma_2 = V_y \\ \gamma_4 = V_t \end{pmatrix}, \qquad \mathbf{A} = \begin{pmatrix} \gamma_1\gamma_5 = A_x \\ \gamma_2\gamma_5 = A_y \\ \gamma_4\gamma_5 = A_t \end{pmatrix}. \tag{184}$$

The six components of $\sigma_{\mu\nu}$ are grouped to tensor and axial tensor objects

$$\mathbf{T} = \begin{pmatrix} \gamma_1\gamma_3 = T_x \\ \gamma_2\gamma_3 = T_y \\ \gamma_4\gamma_3 = T_t \end{pmatrix}, \qquad \mathbf{X} = \begin{pmatrix} \gamma_1\gamma_3\gamma_5 = X_x \\ \gamma_2\gamma_3\gamma_5 = X_y \\ \gamma_4\gamma_3\gamma_5 = X_t \end{pmatrix}. \tag{185}$$

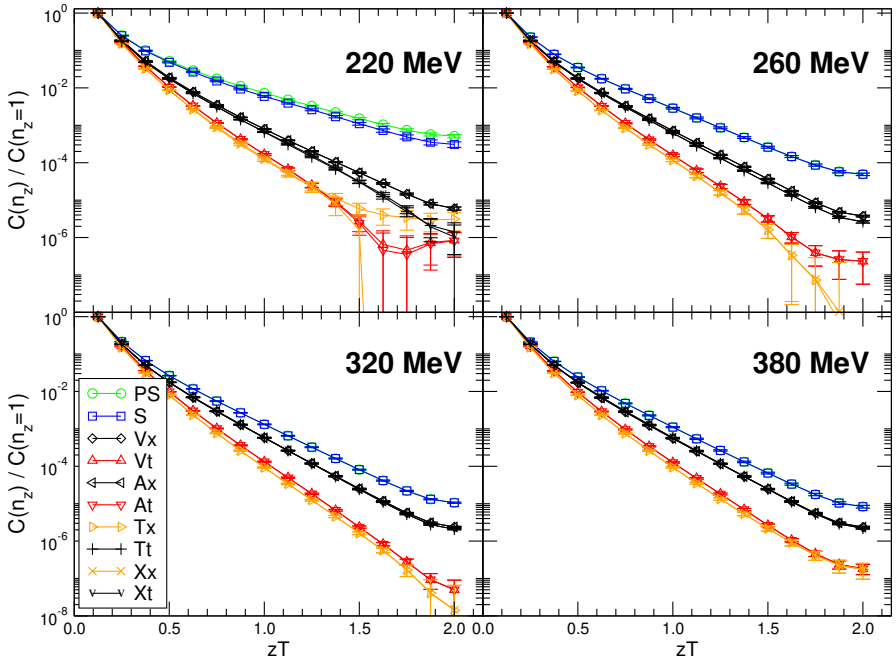

FIGURE 5.4: Normalized correlation functions for $N_t = 8$ ensembles of table 5.2.

This choice of grouping ensures that the resulting objects keep their transformation properties under the chiral-parity group and $\mathrm{U}(1)_A$ transformations as expected from the vacuum. This means that

$$PS \overset{\mathrm{U}(1)_A}{\longleftrightarrow} S, \tag{186a}$$

$$\mathbf{V} \overset{\mathrm{U}(1)_A}{\longleftrightarrow} \mathbf{A}, \tag{186b}$$

$$\mathbf{T} \overset{\mathrm{SU}(2)_A}{\longleftrightarrow} \mathbf{X}. \tag{186c}$$

First results for the spatial correlation functions[3] are given in figure 5.4. With increasing temperature there are three distinctive groups of correlations evolving. According to transformations (186a)–(186c) we would expect at most seven groups of correlations upon restoration of the chiral symmetries: one for scalars, three for the pairwise degenerate vector–axial vector, and three more for pairwise degenerate tensor elements. Taking into account the rotational symmetry of the finite temperature lattice, an additional degeneracy of x and y vector and tensor components reduces the number of expected groups to five. These five groups are the same as they are found for non-interacting quarks (180a)–(180e), where chiral symmetries including $\mathrm{SU}(2)_A$ and $\mathrm{U}(1)_A$ transformations are manifest.

The approximate multiplet structure of figure 5.4 however consists of three multiplets, in the following denoted as E_1, E_2, and E_3:

$$E_1 : \qquad PS \leftrightarrow S \tag{188a}$$

$$E_2 : \qquad V_x \leftrightarrow T_t \leftrightarrow X_t \leftrightarrow A_x \tag{188b}$$

$$E_3 : \qquad V_t \leftrightarrow T_x \leftrightarrow X_x \leftrightarrow A_t. \tag{188c}$$

[3] Plotting lattice data from different ensembles in dependence of lattice points could be misleading, as *e.g.* different β causes a different physical extend. Therefore a rescaling

$$zT = z\frac{1}{N_t a} = n_z a \frac{1}{N_t a} = \frac{n_z}{N_t} \tag{187}$$

is performed to compare dimensionless data.

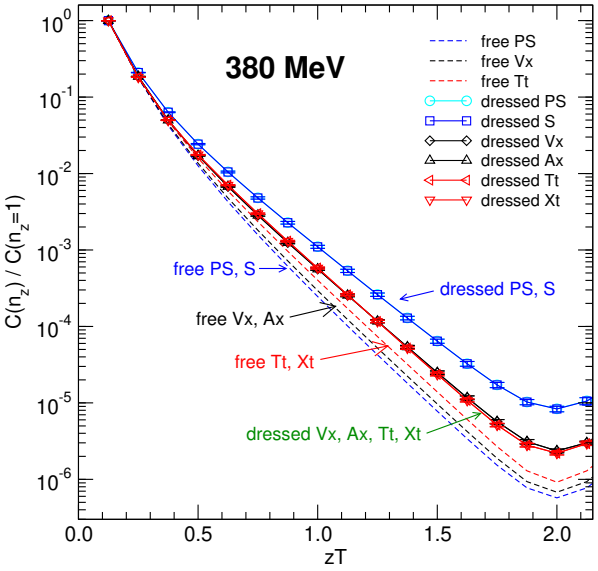

FIGURE 5.5: Correlation functions for the E_2 multiplet. Dashed lines give the corresponding correlations for non-interacting quarks. While for the non-interacting, *free* quarks the symmetry structure expected from the chiral symmetries is shown, the interacting, *dressed* data clearly shows a higher symmetry. This higher symmetry is consistent with $\mathrm{SU}(2)_{CS}$ and $\mathrm{SU}(4)$ symmetries, which have previously been found in literature — *cf.* section 4.1.

Multiplet E_1 agrees with observation of effective $\mathrm{U}(1)_A$ symmetry restoration. Multiplets E_2 and E_3 imply $\mathrm{SU}(2)_L \times \mathrm{SU}(2)_R$ restoration, but the situation of approximately degenerate states is a little more intricate in these cases. Therefore figures 5.5 and 5.6 show the E_2 and E_3 multiplets in more detail at a temperature of 380 MeV, along with data for non-interacting fermions.

The exponential decay of correlation functions gives a first impression of how mesonic modes are realized at high temperature. In chapter 6 the symmetry properties of meson correlations will be investigated in terms of ratios, which allows for a more detailed study.

5.4 Baryons

For baryon spectroscopy at high temperature similar considerations apply as for mesons. The operators are given by (160) with the diquark structures of table 4.6. Correlations are calculated by

$$C_{N_k^\pm}(z) = \langle N_k(\tilde{\mathbf{0}}, z)\mathcal{P}^\pm N_k(\mathbf{0}, 0)\rangle \,. \tag{189}$$

The zero momentum projection for measurement in z-direction now projects to momentum (182). Furthermore, two kinds of projection operators are used:

- $\mathcal{P}_t^\pm$ of (161) for parity, and
- $\mathcal{P}_z^\pm$ of (162) for z-projection.

The results for parity projected operators are given in figure 5.8, for z-projected operators the plots are in figure 5.8.

Again, as the data points of the exponential decrease are close to each other and less predicative, the symmetry properties will be discussed later in chapter 6 in terms of ratios of correlation functions.

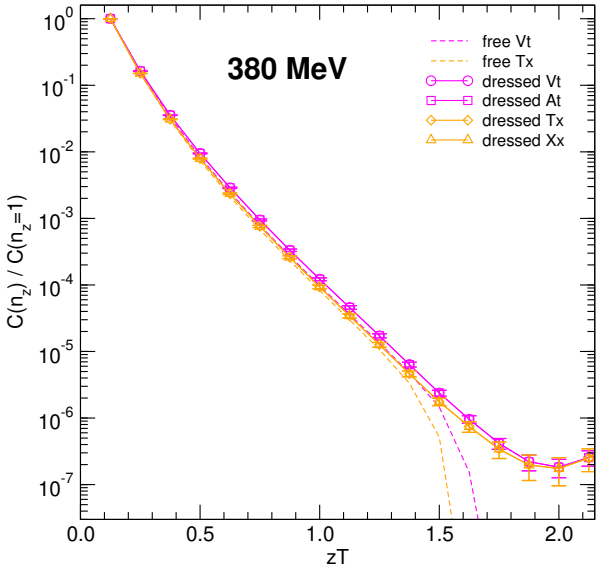

FIGURE 5.6: Correlation functions for the E_3 multiplet. Dashed lines give the corresponding correlations for non-interacting quarks. The non-interacting data shows a zero crossing after some distance. As this behaviour is not consistent with asymptotic expectations from continuum calculations presented in 5.2, it is concluded to be a lattice artifact due to the propagation of free quarks. The dynamics for this set of operators is not fully understood yet.

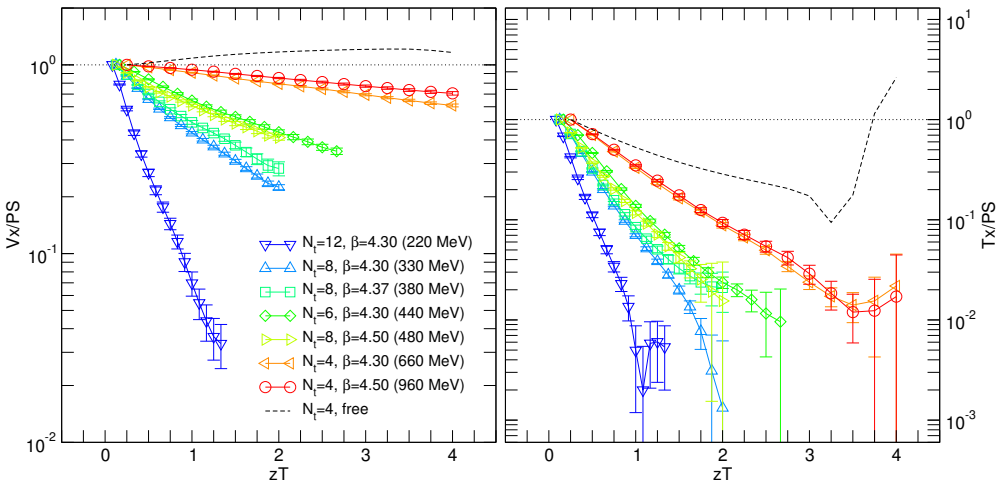

FIGURE 5.7: The left panel shows the ratio of normalized V_x to PS correlators. While for lower temperatures the difference is large due to the light pion mass, the spacing diminishes for higher temperatures. On the right panel the ratio of normalized T_x to PS is shown.

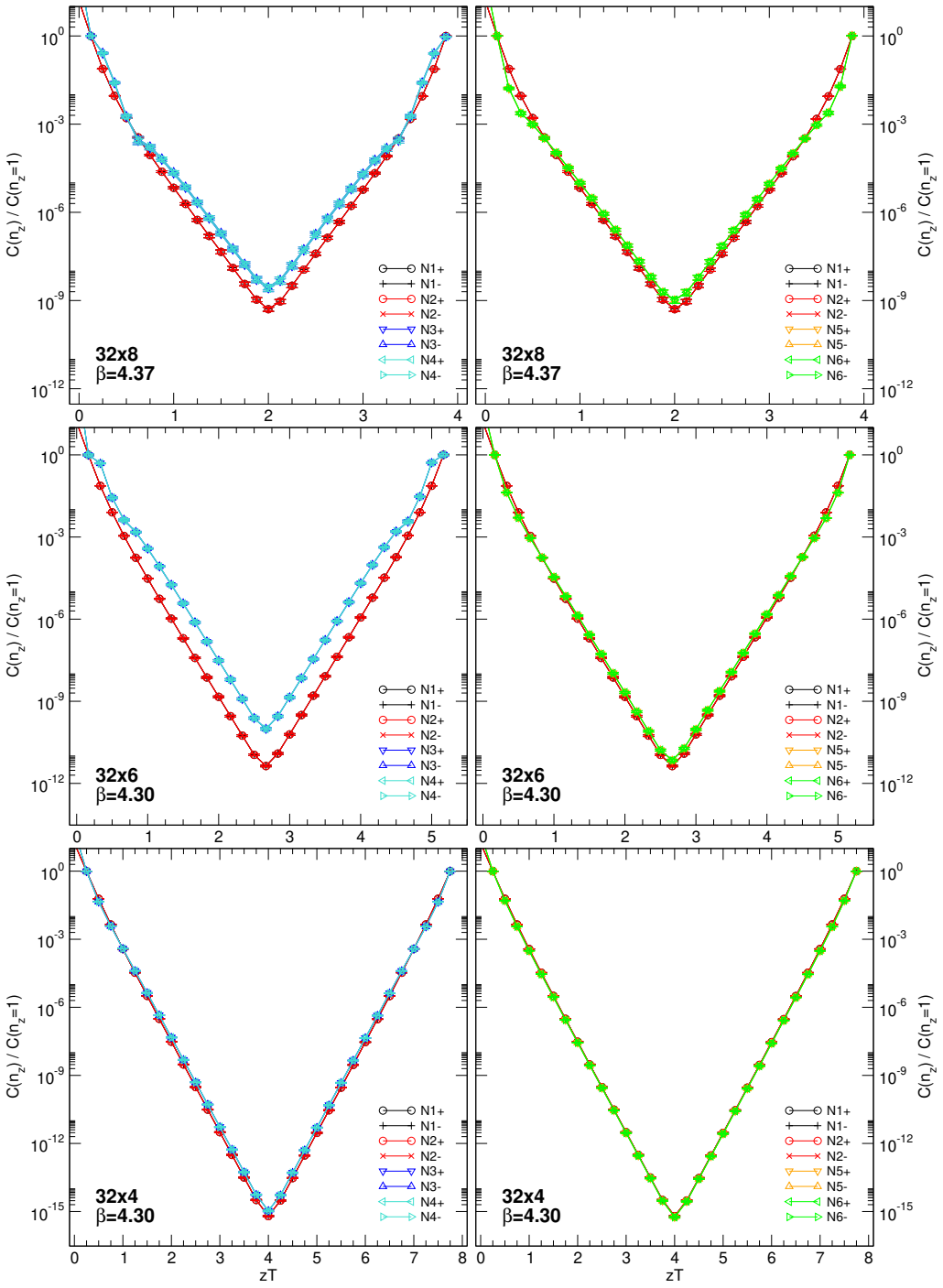

FIGURE 5.8: Absolute value of normalized nucleon correlators using parity projection. Note that for the 32×8 and 32×6 ensembles zero crossing occurs for operators N_3 and N_4 at a distance $zT \approx 0.75$. The dynamics responsible are not yet understood.

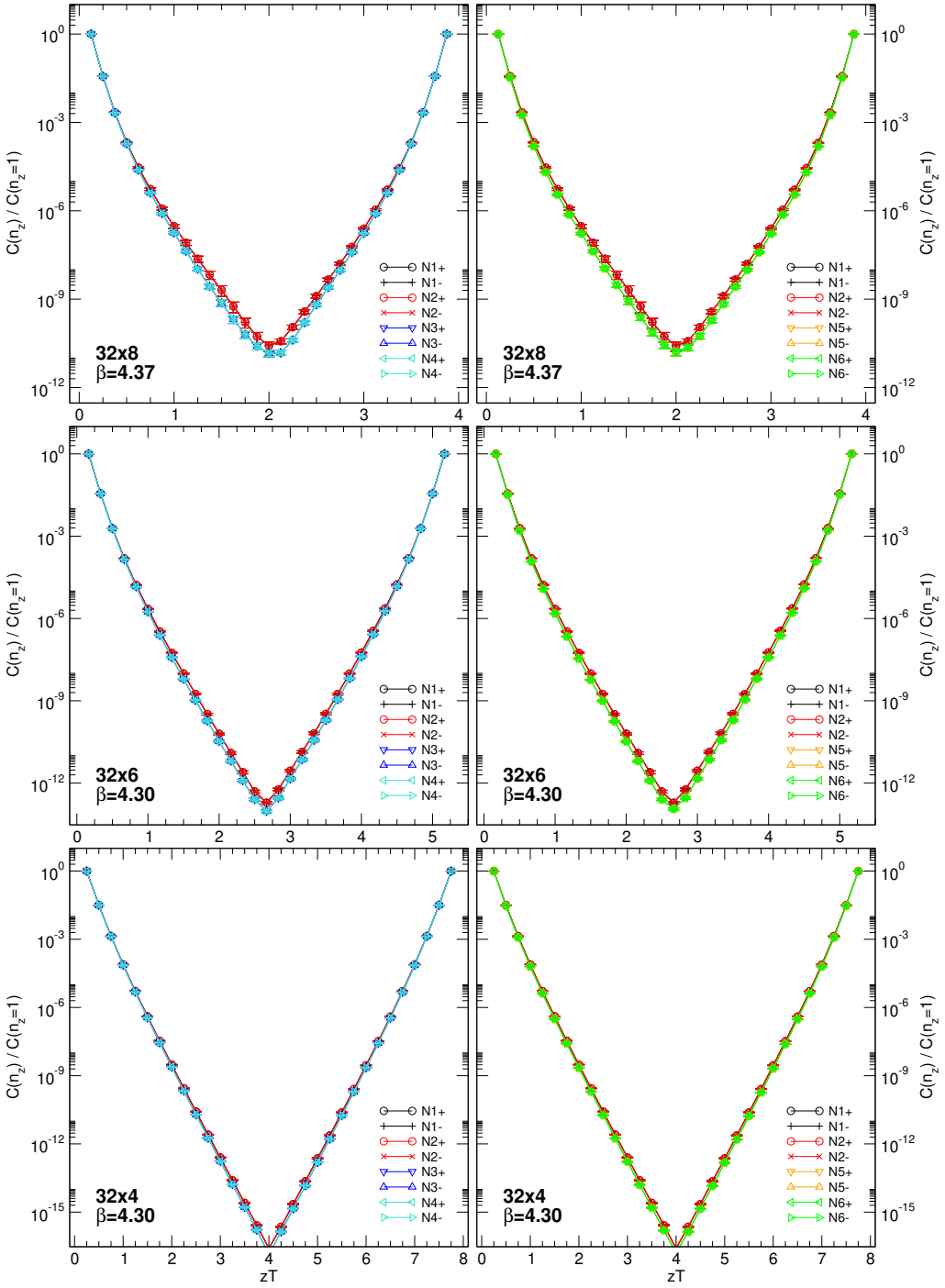

FIGURE 5.9: Normalized nucleon correlators z-projected.

Chapter 6

Symmetries at high temperature

A wise lesson to be drawn from one's life experiences is, that long arguments are often much more dubious than short ones.

— Gerard 't Hooft, *Cellular Automaton Interpretation of Quantum Mechanics*

Usual hadron spectroscopy extracts effective masses of states from the asymptotic behaviour of Euclidean correlation functions in temporal direction. Due to the finite temperature interpretation the asymptotic behaviour is inaccessible in our simulation, as discussed in the introduction to chapter 5, hence the extraction of effective masses is not possible. Measurements of local or bulk thermodynamical properties are not directly affected, neither are long-ranged hadronic correlations in spatial directions.

The chiral properties of the hadron spectrum are inherited from the corresponding correlation functions. If the correlation functions are symmetric under a certain symmetry group, this directly becomes manifest in the spectrum. Thus it is sufficient to study symmetry properties of correlation functions.

In sections 6.1 and 6.2 chiral– and $\mathrm{U}(1)_A$ symmetry properties of the lattice data are shown. Section 6.3 introduces $\mathrm{SU}(2)_{CS}$ and $\mathrm{SU}(4)$ symmetries and identifies its multiplets in the present simulation setup. Section 6.4 presents the corresponding lattice data. Section 6.5 ends this chapter with observations and implications of $\mathrm{SU}(4)$ symmetry.

6.1 Chiral symmetry

Chiral symmetry – in the sense of flavor non-singlet $\mathrm{SU}(2)_L \times \mathrm{SU}(2)_r$ transformations – is spontaneously broken in the QCD vacuum, *i.e.* realized in the Nambu–Goldstone mode. Hence the chiral partners of hadrons, which lie within the same irreducible representation of the chiral-parity group, are not mass degenerate. For simple lattice calculations of vacuum QCD this has been verified in chapter 4.

Chiral symmetry restoration is expected in the high temperature phase of QCD after some critical temperature. Therefore chiral partners are required to become mass degenerate, as their correlation functions transform within the same representation of the chiral-parity group.

For mesons *e.g.* the $\mathbf{V}$ and $\mathbf{A}$ operators both transform according to the $(1,0)\oplus(0,1)$ representation

$$\mathbf{V}, \mathbf{A} \in (1,0) \oplus (0,1). \tag{190}$$

The representation has a multiplicity of $\mathbf{6}$, *cf.* section 3.3, which is saturated by three isovector components of $\mathbf{V}$ and $\mathbf{A}$ each. Given a scenario of perfect symmetry restoration and massless quarks, their correlation functions should be identical and result in a ratio of 1. Figure 6.1 shows the ratio of normalized x-components of $\mathbf{V}$ and $\mathbf{A}$. For any ensemble, *i.e.* temperature above $T > 220$ MeV, the ratio

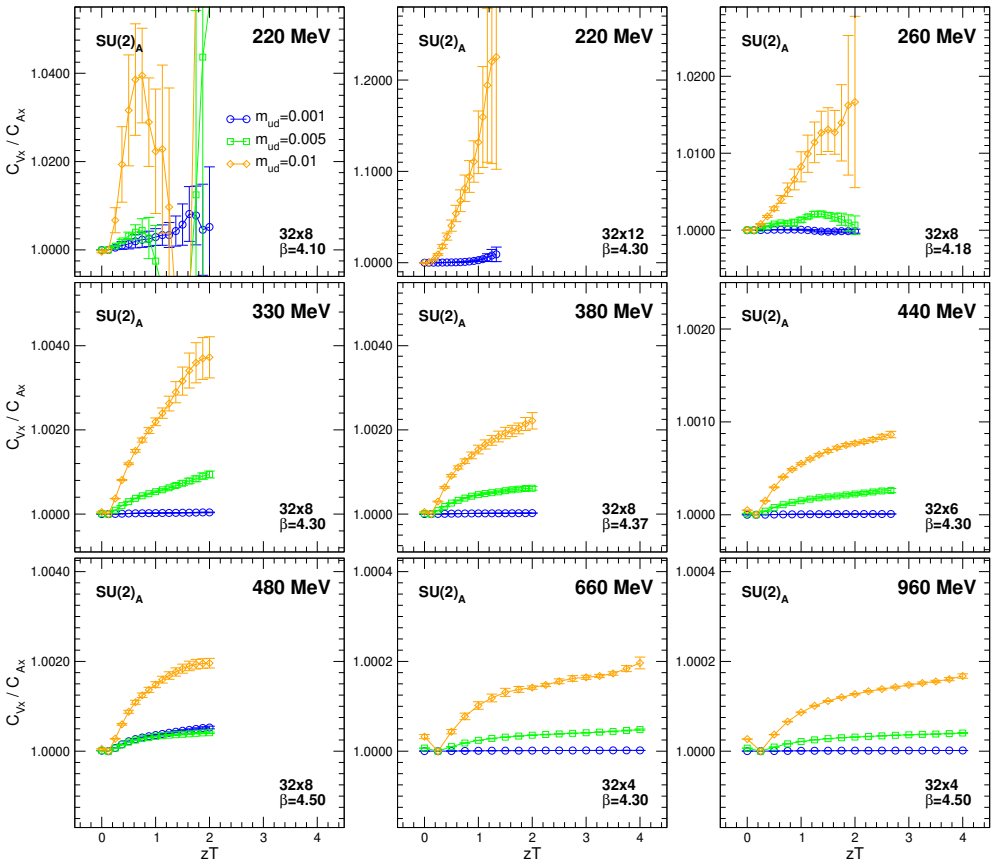

FIGURE 6.1: $SU(2)_A$ symmetry violation for different temperatures and masses. The x-components of $\mathbf{V}$ and $\mathbf{A}$ operators transform according to the $(1,0)\oplus(0,1)$ representation of the chiral-parity group. Chiral symmetry restoration therefore requires the correlation functions of the operators to be identical, *i.e.* give a ratio of 1. However, for any finite mass there is still explicit symmetry breaking. Depicted is the ratio of normalized correlation functions.

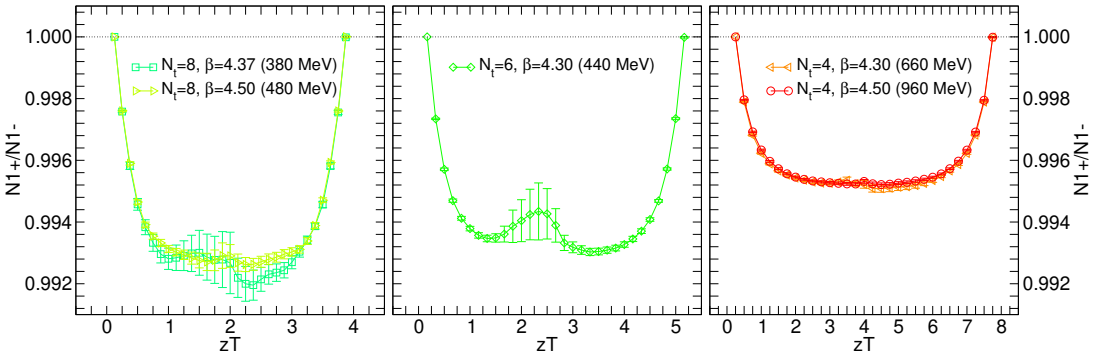

FIGURE 6.2: Parity doubling in the nucleon channel for N_1 operators.

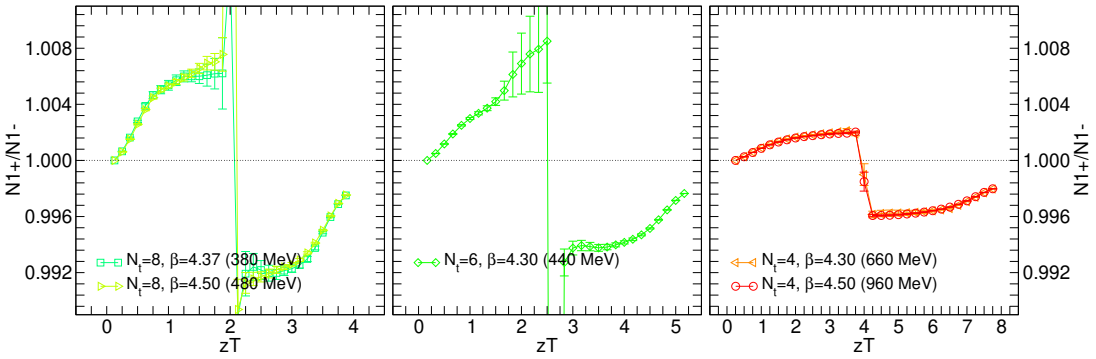

FIGURE 6.3: 'Parity doubling' in the nucleon channel for N_1 operators of z-projection. The change of sign at the symmetry point has the following origin: By measuring the N_1^+ operator of z-projection in z-direction, its partner particle is propagating backwards, *i.e.* the N_1^-. While measuring the ratio N_1^+/N_1^- in forward direction, it is the ratio N_1^-/N_1^+ in backward direction.

for the lowest quark mass $m_{ud} = 0.001$ is below 1.01 and the breaking therefore at a sub-percent level. With increasing temperature the ratio approaches 1. At the same time the estimate for the statistical error diminishes, which means that fluctuations due to the gauge field get smaller and the deviation from an exact ratio of 1 are dominated by the explicit symmetry breaking due to the finite quark mass. In total there is compelling evidence of chiral symmetry restoration in the mesonic spectrum.

For nucleons the restoration of chiral symmetry requires the coincidence of parity partners of operators, *e.g.* N_1^+ and N_1^-. This can be seen again by studying the irreducible representations of the chiral-parity group:

$$N_1^+, N_1^- \in (0, \frac{1}{2}) \oplus (\frac{1}{2}, 0). \tag{191}$$

Both N_1 operators come in two isospin flavors – which are the same for exact isospin symmetry and connected by the $\mathrm{SU}(2)_V$ isospin subgroup – hence one $(0, 1/2) \oplus (1/2, 0)$ representation of (90) with multiplicity **4** is saturated. Our lattice results are given in figures 6.2 and 6.3. As for the mesons, the deviation from exact chiral symmetry restoration is less than one percent. The statistical error seems to dominate at highest temperatures, which indicates the dominance of explicit breaking of chiral symmetry. The restoration of chiral symmetry through parity doubling in baryons has been studied *e.g.* in [92, 93] using $n_f = 2 + 1$ Wilson fermions on anisotropic lattices, or in [94] using a quenched simulation of clover–improved Wilson fermions. Both cases find similar results. The exact details of how partiy doubling for baryons is realized could be of theoretical interest for understanding modifications of thermodynamical properties [95].

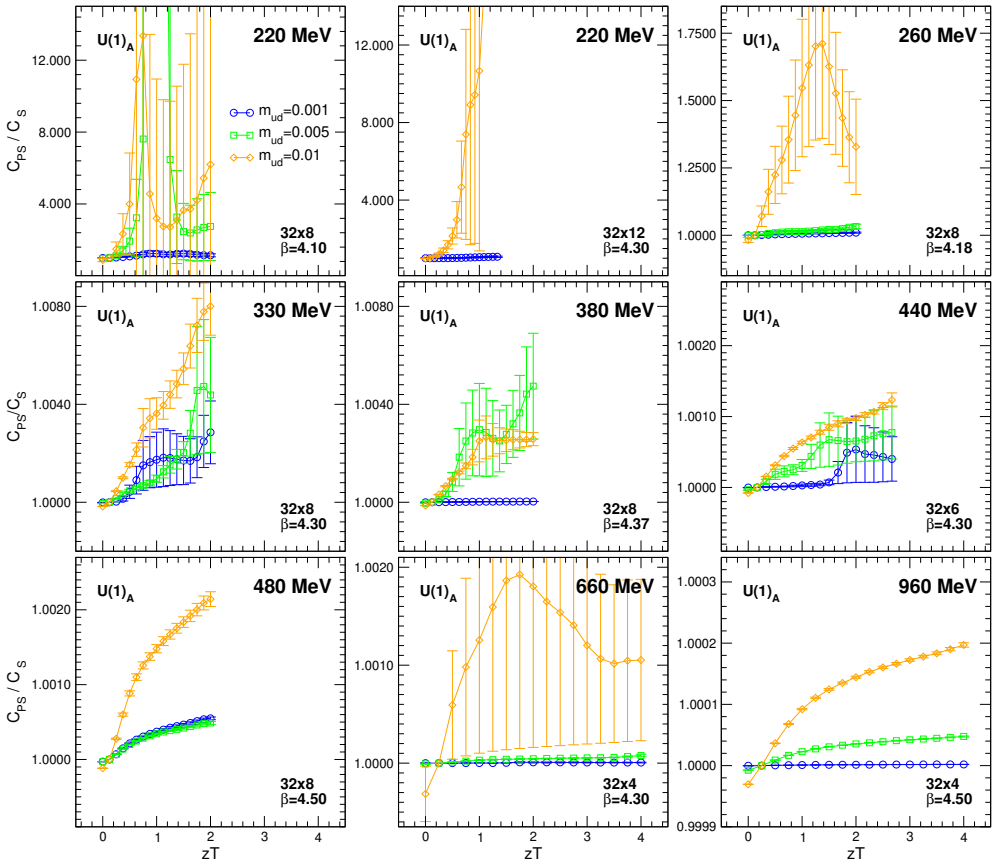

FIGURE 6.4: $\mathrm{U}(1)_A$ symmetry violation for different temperatures and masses. Pseudo scalar PS and scalar S operators belong to different representations of the chiral-parity group, but transform into each other under $\mathrm{U}(1)_A$ transformations. Effective restoration of $\mathrm{U}(1)_A$ symmetry therefore requires the correlation functions of the operators to be identical, *i.e.* give a ratio of 1. However, for any finite mass there is still explicit symmetry breaking, as well as the anomalous breaking due to the axial anomaly. Depicted is the ratio of normalized correlation functions.

6.2 $\mathrm{U}(1)_A$ symmetry

The situation concerning $\mathrm{U}(1)_A$ symmetry is different from non-singlet chiral symmetry. The symmetry is broken due to explicit, spontaneous and anomalous effects, *cf.* section 3.2. In literature however a possible weakening of the axial anomaly is discussed, *e.g.* [96, 97], such that there are no anomalous breaking effects left at high temperatures.

We study $\mathrm{U}(1)_A$ symmetry breaking through ratios of isovector pseudo scalar PS and scalar S mesons. They belong to different representations of the chiral-parity group:

$$PS \in (\frac{1}{2}, \frac{1}{2})_a, \tag{192a}$$

$$S \in (\frac{1}{2}, \frac{1}{2})_b, \tag{192b}$$

where the subscript denotes two different representations of opposite parity. $\mathrm{U}(1)_A$ transformations mix both representations, and studying the ratio of PS and S enables to quantify $\mathrm{U}(1)_A$ symmetry breaking effects. Our lattice data is represented in figure 6.4. Quantitatively very similiar results are found as for

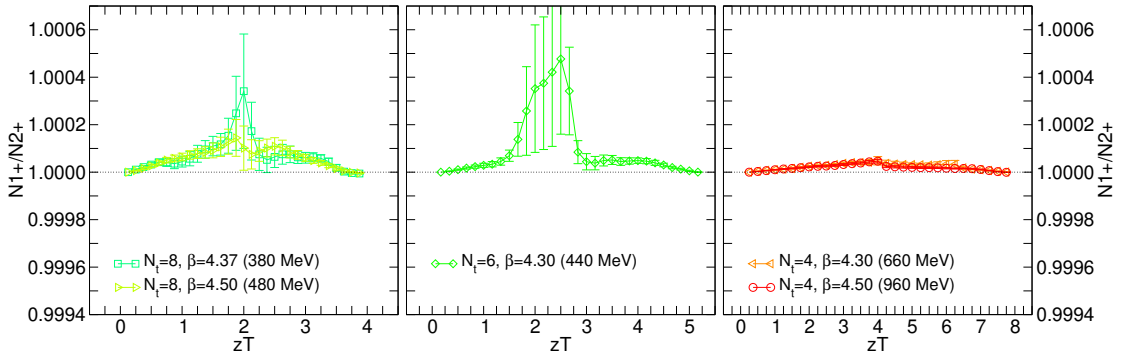

FIGURE 6.5: $\mathrm{U}(1)_A$ symmetry violation in nucleons.

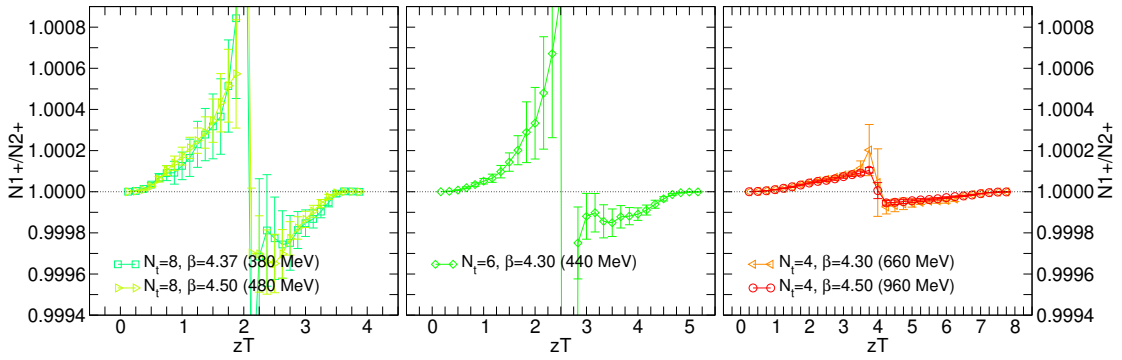

FIGURE 6.6: $\mathrm{U}(1)_A$ symmetry violation in nucleons of z-projection. For a description of the sign-changing effect see the description of figure 6.3.

the chiral symmetry breaking in figure 6.1. Indeed no strong effects of anomalous symmetry breaking are observed.

For studying $\mathrm{U}(1)_A$ symmetry in baryons, two nucleon operators with different chiral properties are required:

$$N_1^+ \in (0, \frac{1}{2}) \oplus (\frac{1}{2}, 0)_a \tag{193a}$$

$$N_2^+ \in (0, \frac{1}{2}) \oplus (\frac{1}{2}, 0)_b. \tag{193b}$$

Again, the subscript denotes two distinctive irreducible representations of the chiral-parity group. $\mathrm{U}(1)_A$ symmetry mixes both representations, and the ratio N_1^+/N_2^+ quantifies its breaking. The lattice data is presented in figures 6.5 and 6.6. The conclusions are consistent with the mesonic case: $\mathrm{U}(1)_A$ symmetry is realized to a high degree, and its violation is dominated by explicit breaking at high temperatures.

6.3 $\mathrm{SU}(2)_{CS}$, $\mathrm{SU}(4)$ and multiplets

In addition to flavor singlet and non-singlet chiral symmetries, a newly proposed $\mathrm{SU}(2)_{CS}$ *chiral spin* symmetry is of interest at high temperatures, *cf.* sections 4.1 and 4.4. This symmetry acts in Dirac space and is diagonal in flavor space. Its generators are given by

$$\vec{\Sigma} = \{\gamma_k, -i\gamma_5\gamma_k, \gamma_5\}, \tag{194}$$

which satisfy a $\mathfrak{su}(2)$ algebra

$$[\Sigma_\alpha, \Sigma_\beta] = 2i\epsilon^{\alpha\beta\gamma}\Sigma_\gamma \tag{195}$$

for any $k = 1, 2, 3, 4$. The γ_5 in its generators means that $\mathrm{U}(1)_A$ is a subgroup of any realization of the $\mathrm{SU}(2)_{CS}$ group. The anomalous breaking properties[1] are therefore inherited. Incorporating rotations in flavor space with generators τ_a a minimal group $\mathrm{SU}(2n_f)$ containing flavor non-singlet chiral symmetry and chiral spin symmetry can be derived with generators

$$\{(\tau_a \otimes \mathbb{1}_D), (\mathbb{1}_F \otimes \Sigma_i), (\tau_a \otimes \Sigma_i)\}, \tag{196}$$

where $a = 1 \,..\, (n_f^2 - 1)$ is the flavor index and $i = 1, 2, 3$ the chiral spin index.

The chiral spin transformations mix left-handed and right-handed parts of Dirac spinors by construction. Thus also different irreducible representations of the chiral-parity group are affected and mixed. To study this behaviour in detail, the following representations of $\mathrm{SU}(2)_{CS}$, obeying (195), are defined:

$$R_1 : \{\gamma_1, -i\gamma_5\gamma_1, \gamma_5\} = \{\sigma^{23}\, i\gamma_5\gamma_4, \sigma^{23}\, \gamma_4, \gamma_5\}, \tag{197a}$$
$$R_2 : \{\gamma_2, -i\gamma_5\gamma_2, \gamma_5\} = \{\sigma^{31}\, i\gamma_5\gamma_4, \sigma^{31}\, \gamma_4, \gamma_5\}. \tag{197b}$$

Those differ from the representation $\{\gamma_4, -i\gamma_5\gamma_4, \gamma_5\}$ relevant for t-direction correlators [98] by the rotations $\sigma^{23} = \frac{i}{2}[\gamma_2, \gamma_3]$ and $\sigma^{31} = \frac{i}{2}[\gamma_3, \gamma_1]$. Keeping in mind notation (183a)-(185) for mesons propagating in z-direction, transformations R_1 and R_2 connect the following operators:

$$R_1 : (V_y, T_t, X_t) \tag{198a}$$
$$R_1 : (V_t, T_y, X_y) \tag{198b}$$
$$R_2 : (V_x, T_t, X_t) \tag{198c}$$
$$R_2 : (V_t, T_x, X_x) \tag{198d}$$

In more detail this can be seen by[2]

$$R_1 : \quad \begin{array}{ccccc} V_y & \longleftrightarrow & -iT_t & \longleftrightarrow & -X_t \\ \Updownarrow & & \Updownarrow & & \Updownarrow \\ \gamma_2 & & \gamma_2(-i\gamma_5\gamma_1) & & \gamma_2\gamma_1 \\ & & = -i\gamma_4\gamma_3 & & = -\gamma_4\gamma_3\gamma_5 \end{array}$$

$$R_2 : \quad \begin{array}{ccccc} V_x & \longleftrightarrow & iT_t & \longleftrightarrow & X_t \\ \Updownarrow & & \Updownarrow & & \Updownarrow \\ \gamma_1 & & \gamma_1(-i\gamma_5\gamma_2) & & \gamma_1\gamma_2 \\ & & = i\gamma_4\gamma_3 & & = \gamma_4\gamma_3\gamma_5 \end{array}$$

As the finite temperature lattice is symmetric in x and y directions, the physics should not change under exchange of x and y. Now an interchange operator $\hat{P}_{xy}$ can be defined

$$\hat{P}_{xy} : \quad \gamma_1 \leftrightarrow \gamma_2 \tag{199a}$$
$$\hat{P}_{xy} : \quad \hat{P}_{xy}\gamma_5 = -\gamma_5. \tag{199b}$$

Then applying $\hat{P}_{xy}R_1$ modifies the representation to $\{\gamma_2, i\gamma_5\gamma_2, -\gamma_5\}$, which is isomporphic to the R_2 generator set. The finite temperature lattice includes both $\hat{P}_{xy}$ and $\mathbb{1}$ transformations, which form a

[1] Note that the anomalous breaking as shown by Fujikawa [49,50] occurs for the generator γ_5, and γ_5 only.

[2] This is a sloppy notation. The symmetry acts in Dirac space only, thus the relevant Dirac structure of an operator is given.

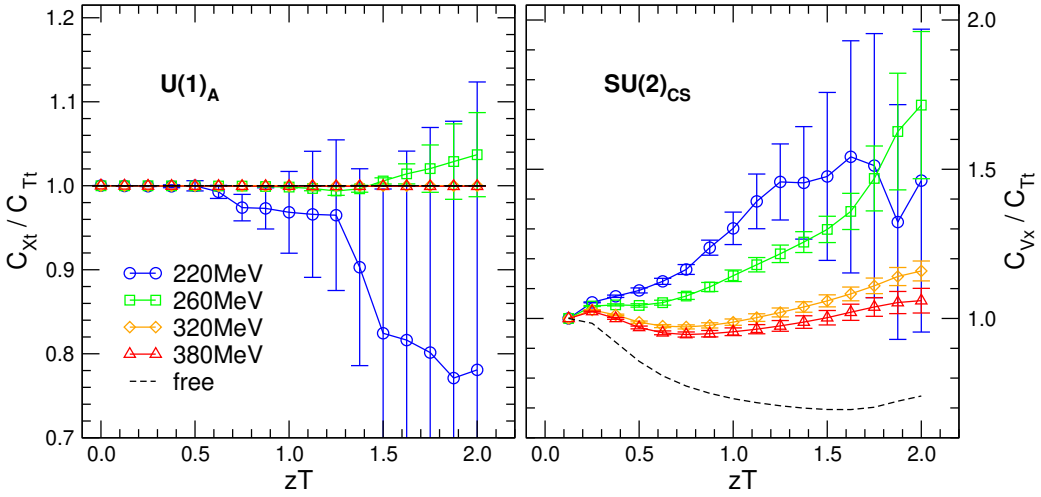

FIGURE 6.7: The left panel shows a ratio of normalized correlators connected by $U(1)_A$ transformations for various temperatures. The right panel shows a ratio of normalized correlators connected by $SU(2)_{CS}$ transformations from the E_2 multiplet (188b).

group S_2. This means that $S_2 \times SU(2)_{CS}$ contains the multiplets

$$(V_x, V_y, T_t, X_t) \tag{200a}$$
$$(V_t, T_x, T_y, X_x, X_y), \tag{200b}$$

which is the approximate multiplet structure identified in (188b)–(188c).

6.4 $SU(2)_{CS}$ lattice data

In figure 5.4 the evolution of different vector channel operators has been shown for increasing temperatures. At 380 MeV three approximate mutliplets E_1, E_2 and E_3 have been identified.

In figure 6.7 a more detailed plot for the symmetries of the E_2 group can be seen. The $U(1)_A$ symmetry therein has already been discussed in section 6.2. On the right side a ratio for quantifying the $SU(2)_{CS}$ symmetry introduced in section 6.3 is shown. The same ratio for all available lattice ensembles and temperatures is shown in 6.8, along with the ratio for non-interacting quarks. The ratio depends strongly on the temperature and can be used to identify three coarse regions:

- $V_x/T_t > 1$ $SU(2)_{CS}$ is broken at low temperatures
- $V_x/T_t \simeq 1$ $SU(2)_{CS}$ is approximately manifest at $2T_c$
- $V_x/T_t < 1$ $SU(2)_{CS}$ is broken at high temperatures

Figure 6.9 shows a $SU(2)_{CS}$ ratio for operators from the E_3 multiplet, again with non-interacting data for comparison. The ratio does not depend on the temperature at all and gives a constant $SU(2)_{CS}$ violation.

6.5 Consequences of $SU(2)_{CS}$

The approximate observation of $SU(2)_{CS}$ symmetry in the spectrum of mesons has a few interesting implications. For the following discussion of $SU(2)_{CS}$ we choose a $k = 4$ representation of generators (194).

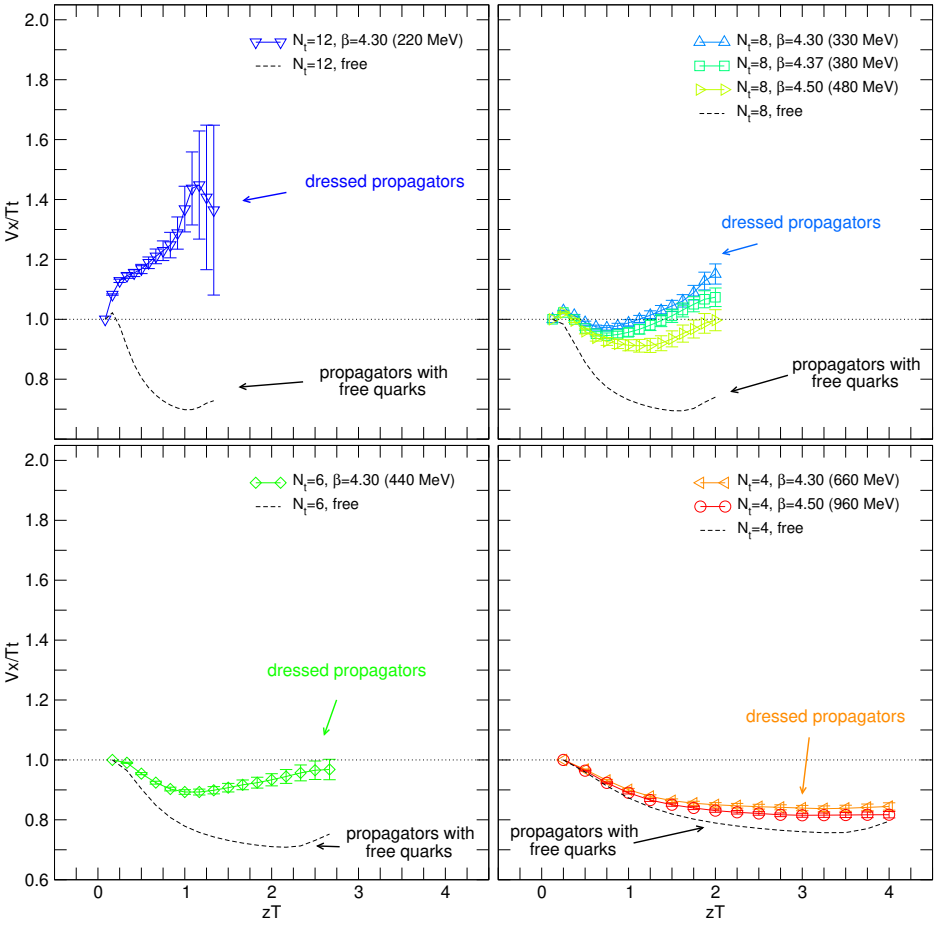

FIGURE 6.8: Detailed ratio for correlation functions of operators connected by $SU(2)_{CS}$ from the E_2 multiplet. The subplots group lattices of same geometry. Dashed lines give the ratio for non-interacting quarks. As it can be seen for all ensembles, the non-interacing quarks do not show $\mathrm{SU}(2)_{CS}$ symmetry. For interacting quarks the $\mathrm{SU}(2)_{CS}$ symmetry properties depend strongly on the temperature. Most notably, there is an intermediate temperature region of $350 - 400$ MeV, where the operators from the E_2 multiplet show $\mathrm{SU}(2)_{CS}$ symmetry. At very high temperatures $T > 1000$ MeV the interacting data seemingly converges to non-interacting data, which is consistent with an asymptotic free scenario.

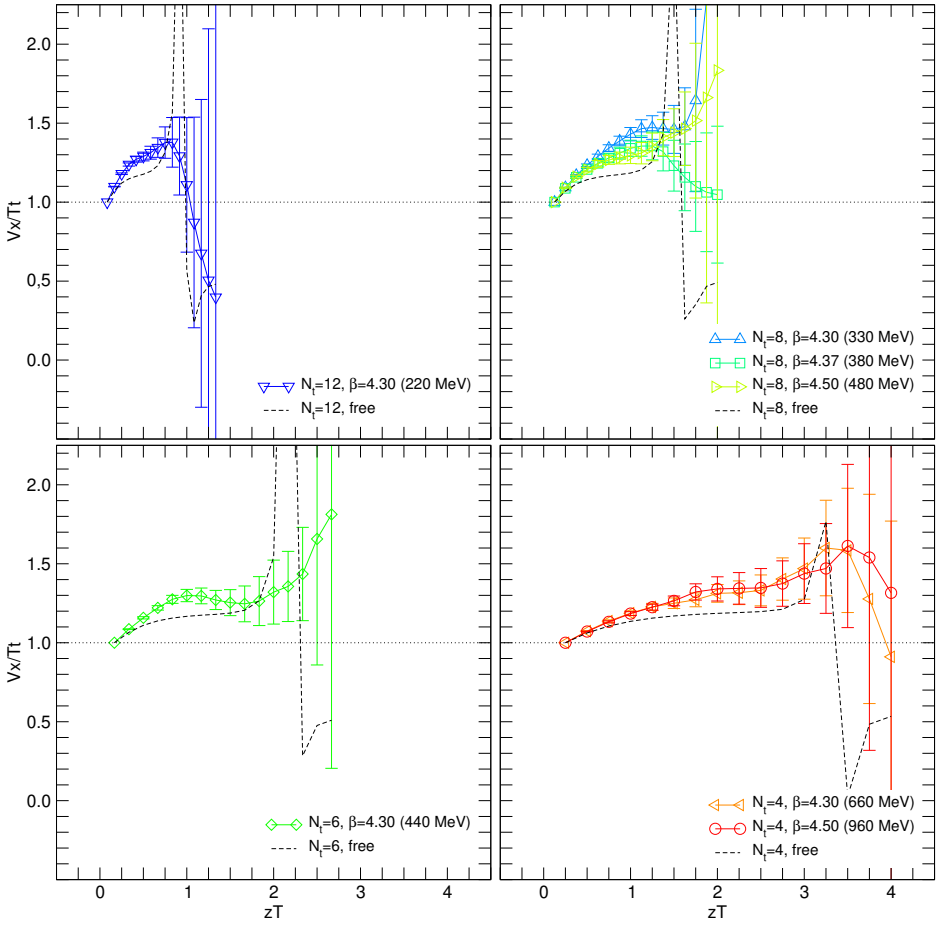

FIGURE 6.9: Detailed ratio for correlation functions of operators connected by $SU(2)_{CS}$ for the E_3 multiplet. The subplots group lattices of same geometry. Dashed lines give the ratio for non-interacting quarks. As it can be seen for all ensembles, the non-interacing quarks do not show $\mathrm{SU}(2)_{CS}$ symmetry. Close to the symmetry point, the non-interacting quarks show divergent behaviour, *cf.* figure 5.6. The interacting data shows similar behaviour to free quarks and a consistent $\mathrm{SU}(2)_{CS}$ violation of $20-40\%$, which is independent from temperature.

First it is instructive to study the symmetry of the massless Dirac lagrangian densitiy (1)

$$\mathcal{L} = \bar{\Psi} \mathrm{i} \partial\!\!\!/ \Psi. \tag{201}$$

While it shows full invariance under chiral– and $\mathrm{U}(1)_A$ transformations, $\mathrm{SU}(2)_{CS}$ symmetry is absent. This is in agreement with the numerical findings of section 6.4, where data for non-interacting quarks is represented by dashed lines. Now as it was introduced in section 2.2, the interaction of gluons and fermions is by construction encoded in the covariant derivative (17):

$$D_\mu = \partial_\mu + A_\mu, \tag{202}$$

where A_μ is composed of gluonic fields. The massless QCD lagrangian density (23) is therefore given by

$$\mathcal{L} = \bar{\Psi} \mathrm{i} D\!\!\!/ \Psi = \bar{\Psi} \mathrm{i} \gamma^4 D_4 \Psi + \bar{\Psi} \mathrm{i} \gamma^i D_i \Psi, \tag{203}$$

where in the last step the covariant derivative is split into a $\bar{\Psi} \mathrm{i} \gamma^4 D_4 \Psi$ part containing the color-electric field A_4, and a $\bar{\Psi} \mathrm{i} \gamma^i D_i \Psi$ part containing the color-magnetic field A_i. $\mathrm{SU}(2)_{CS}$ transformations have the following effect on these parts:

$$\left(\bar{\Psi} \mathrm{i} \gamma^4 D_4 \Psi\right)' \to \left(\bar{\Psi} \mathrm{i} \gamma^4 D_4 \Psi\right), \tag{204a}$$

$$\left(\bar{\Psi} \mathrm{i} \gamma^i D_i \Psi\right)' \nrightarrow \left(\bar{\Psi} \mathrm{i} \gamma^i D_i \Psi\right), \tag{204b}$$

i.e. the color-electric interaction containing part is invariant under $\mathrm{SU}(2)_{CS}$ transformations, the color-magnetic interaction containing part is not. With this observation, the $\mathrm{SU}(2)_{CS}$ ratio $R_{CS} = V_x/T_t$ in figure 6.8 can be interpreted in the following way:

- The kinetic term (201) of non-interacting quarks breaks this symmetry, which can be seen by a ratio $R_{CS} < 1$ in accordance with analytic considerations.
- Any contribution from the color-electric field A_4 will give a ratio $R_{CS} = 1$, as this part of the theory is invariant under $\mathrm{SU}(2)_{CS}$ transformations (204a).
- A ratio of $R_{CS} > 1$ is thus possible only through contributions from the color-magnetic field A_i. The breaking of $\mathrm{SU}(2)_{CS}$ through color-magnetic interaction is clear from (204b).

These considerations offer the possibility to estimate the strength of color-magnetic and color-electric interactions at high temperature. By applying these symmetry arguments to the spectrum of a theory, derived statements are implicitly gauge-invariant.

For the present case of figure 6.8 this means *e.g.* that at lower temperatures $T \simeq 220$ MeV the color-magnetic interaction is dominating, as R_{CS} is well above 1. For increasing temperature its contribution is diminishing and the ratio R_{CS} gets approximately 1 at $T \simeq 2T_c$. For even higher temperatures the ratio drops below 1 and approaches the kinetic data for non-interacting fermions. In this limit asymptotic freedom is reached.

Chapter 7

Conclusion

In anything at all, perfection is finally attained not when there is no longer anything to add, but when there is no longer anything to take away, when a body has been stripped down to its nakedness.

— Antoine de Saint-Exupéry, *Wind, Sand and Stars*

While the vacuum phenomenology of QCD is well understood by means of non-perturbative lattice methods, strongly interacting matter at high temperatures is still an elusive subject, theoretically as well as experimentally. The general consens of experimental results on heavy ion collisions states the formation of a new kind of matter, whose properties differ vastly from ordinary hadronic matter. Many problems remain unanwered, most notably is the still open question for the effective degrees of freedom, which describe the dynamics at high temperatures.

The theoretical study of gauge theories offers incentives to find models and explanations, and from early on these were directed towards free and deconfined quarks and gluons. In analogy to QED a plasma-like phase is conjectured, and most models account for a *liberation of degrees of freedom*.

As theoretical understanding of QCD progresses, many hints are revealed, which help to understand the thermodynamics at finite temperature. Especially the various effects associated with chiral symmetry and the chiral transition are well understood. However, alleged phenomenon of deconfinement is not. Arguments from QCD as pure gauge theory, *e.g.* the Z_3 center symmetry, place the color-deconfinement transition at a similar temperature range as the chiral transition. But it is a priori not clear how fermions change this picture. The notion of a direct link between chiral symmetry retoration and deconfinement is further supported by Cashers argument [99], which qualitatively argues that chiral symmetry is necessarily broken in confining theories. In general this is not always true, and certain scenarios have been stated [100] in which the argument breaks down. In the large N_c limit *e.g.* chiral symmetry restoration and deconfinement might be separate phenomena, with the possibility of chirally symmetric but confined matter [101]. By studying the hadronic screening spectrum in quenched lattice QCD, evidence of the presence of hadronic modes in the high temperature phase of QCD has been found [102,103], which is a strong argument against the common *deconfinement folklore* [102,103].

In this work the symmetry properties of strongly interacting matter at high temperatures are investigated by means of a fully dynamical, $n_f = 2$ flavor lattice simulation using chiral fermions. The spectrum of spatial correlation functions is examined to verify chiral symmetry restoration. In section 6.1 the findings are reported. The correlation functions of chiral partners coincide to a high degree, with some explicit breaking due to non-vanishing quark masses remaining. Thus chiral symmetry is realized in the Wigner-Weyl mode, which is supported by a strong increase in the slope of the pseudo scalar operator — *i.e.* the Goldstone mode vanishes and heavier $\bar{q}q$ modes contribute in this channel. For nucleons parity doubling could be verified to a high degree, again with some residual breaking left which is attributed to

explicit symmetry breaking.

For flavor singlet axial transformations, *i.e.* $\mathrm{U}(1)_A$ symmetry, the stack of symmetry breaking effects includes the axial anomaly. In literature [96, 97] it is argued that under certain technical assumptions the anomalous breaking effects should not be visible and the symmetry be effectively restored. In section 6.2 effective restoration is observed by verifying degeneracy of different representations of the chiral-parity group, which are connected by $\mathrm{U}(1)_A$ transformations.

Lastly the properties of a recently proposed $\mathrm{SU}(2)_{CS}$ symmetry are evaluated for the mesonic spectrum in section 6.4. A reduced rotational invariance of the finite temperature setup causes the vector components of mesonic operators to naturally split into two energy levels, which are denoted as E_2 and E_3. Operators of the E_2 multiplet show approximate $\mathrm{SU}(2)_{CS}$ symmetry at a temperature of $2T_c$. Due to considerations presented in section 6.5, this symmetry could be a useful tool to distinguish effects of color-electric and color-magnetic fields. For the E_3 multiplet the situation is a lot less clear, as the data shows a constant breaking of $\mathrm{SU}(2)_{CS}$ regardless of temperature. Also the dynamics for non-interacting quarks are not obvious for these operator modes.

As open questions a few interesting points can be mentioned. The exact relevance and physical meaning of the E_3 meson multiplet is not clear. Its dynamics for non-interacting quarks as well as the constant $\mathrm{SU}(2)_{CS}$ symmetry breaking pose questions which need to be answered. The $\mathrm{SU}(2)_{CS}$ symmetry structure for baryons in a finite temperature setup, *i.e.* measurements in z-direction, represents an interesting questions.

Finally, the effective degrees of freedom for this strongly interacting matter at intermediate to high temperatures stay a riddle. They are certainly no hadrons, gluons or single quarks, but chiral and color-singlet objects. For identifying their interaction, $\mathrm{SU}(2)_{CS}$ may be of importance.

And then, as in any lattice study, the statistics could be improved.

Appendices

Appendix A

Conventions

Throughout this work natural units are used, this means

$$\hbar = c = k_B = 1, \tag{205}$$

and implies

$$[\text{energy}] = [\text{momentum}] = [\text{mass}] = [\text{temperature}] = 1/[\text{length}] = 1/[\text{time}] = \text{MeV}.$$

An often used conversion factor is

$$\hbar c = 197.3269631 \text{ MeV fm}. \tag{206}$$

Latin indices usually run from $1 \ldots 3$, greek indices in Minkowski space from $0 \ldots 3$, and greek indices in Euclidean space from $1 \ldots 4$.

The Pauli matrices are given by

$$\sigma_1 = \begin{bmatrix} 0 & 1 \\ 1 & 0 \end{bmatrix}, \quad \sigma_2 = \begin{bmatrix} 0 & -\mathrm{i} \\ \mathrm{i} & 0 \end{bmatrix}, \quad \sigma_3 = \begin{bmatrix} 1 & 0 \\ 0 & -1 \end{bmatrix}, \tag{207}$$

where in the context of isospin they will be referred to as τ matrices.

The Euclidean gamma matrices in 4 dimensions are given by

$$\{\gamma_\mu, \gamma_\nu\} = 2\delta_{\mu\nu}\mathbb{1}_4, \tag{208}$$

and the γ_5 by the standard definition

$$\gamma_5 = \gamma_1\gamma_2\gamma_3\gamma_4, \tag{209}$$

The gamma matrices used for the lattice calculations in this work are given in Dirac representation:

$$\begin{gathered} \gamma_1 = \begin{bmatrix} 0 & 0 & 0 & -\mathrm{i} \\ 0 & 0 & -\mathrm{i} & 0 \\ 0 & \mathrm{i} & 0 & 0 \\ \mathrm{i} & 0 & 0 & 0 \end{bmatrix}, \quad \gamma_2 = \begin{bmatrix} 0 & 0 & 0 & -1 \\ 0 & 0 & 1 & 0 \\ 0 & 1 & 0 & 0 \\ -1 & 0 & 0 & 0 \end{bmatrix}, \quad \gamma_3 = \begin{bmatrix} 0 & 0 & -\mathrm{i} & 0 \\ 0 & 0 & 0 & \mathrm{i} \\ \mathrm{i} & 0 & 0 & 0 \\ 0 & -\mathrm{i} & 0 & 0 \end{bmatrix}, \\ \gamma_4 = \begin{bmatrix} 1 & 0 & 0 & 0 \\ 0 & 1 & 0 & 0 \\ 0 & 0 & -1 & 0 \\ 0 & 0 & 0 & -1 \end{bmatrix}, \quad \gamma_5 = \begin{bmatrix} 0 & 0 & 1 & 0 \\ 0 & 0 & 0 & 1 \\ 1 & 0 & 0 & 0 \\ 0 & 1 & 0 & 0 \end{bmatrix}. \end{gathered} \tag{210}$$

Appendix B

Angular and chiral content of the ρ and ρ' mesons

In section 2.3 the low lying hadrons are classified by the flavor content of their quarks. Negative parity mesons of isospin $I = 1$ and spin $J = 1$ are classically called ρ mesons. In a non-relativistic approach mesons can be described as boundstates of its constituent quarks, and thus be assigned quantum numbers, *e.g.* by the $n^{2s+1}\ell_J$ notation. Table 15.2 of [31] lists three experimental ρ states and following classification,

$$\rho(770) \to 1^3S_1, \tag{211a}$$
$$\rho(1450) \to 2^3S_1, \tag{211b}$$
$$\rho(1700) \to 1^3D_1, \tag{211c}$$

where the possibility is mentioned, that the latter two actually might be mixtures of S and D partial waves.

B.1 Previous lattice work

In the context of a larger scale hadron spectroscopy work [104] the overlap of ρ-like operators with extracted states has been used to assign partial waves S and D to physical mesons as seen in (211a)–(211c). Their work however relies on a non-relativistic interpretations of the constituent quarks. It is argued that the D wave overlap of the operators origins from the 'lower' spinor components and gives sub-leading contributions. This is amplified by explicitly projecting to the 'upper' Dirac components. Given the relatively high pion masses $400 - 700$ MeV this seems reasonable.

In a different study [105,106], relying on an ultra-relativistic interpretation of the operator basis, the assignment (211a) could be verified. However, a follow-up study [107,108] found a significant admixture of D wave for the first excited ρ state, *i.e.* the $\rho(1450)$.

B.2 Chiral fermions and the chiral-parity group

In a previous work of the author [109, 110] the same question was addressed, applying the same ultra-relativistic interpretation as in [105–108]. It is highlighted briefly in the following.

A key observation is the fact that the ρ meson couples to two different interpolating fields

$$J^V_\rho(x) = \bar{\Psi}(x)(\tau^a \otimes \gamma^i)\Psi(x), \quad \in (0,1) \oplus (1,0) \tag{212a}$$
$$J^T_\rho(x) = \bar{\Psi}(x)(\tau^a \otimes \gamma^0\gamma^i)\Psi(x), \quad \in (1/2,1/2)_b. \tag{212b}$$

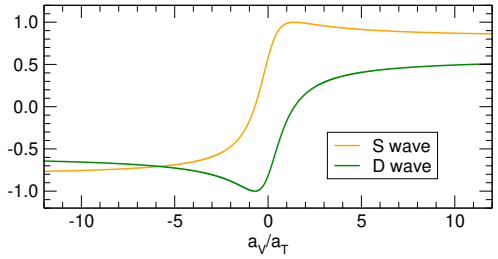

FIGURE B.1: Unitary transformation (213a)–(213b) to connect the chiral- and angular momentum basis.

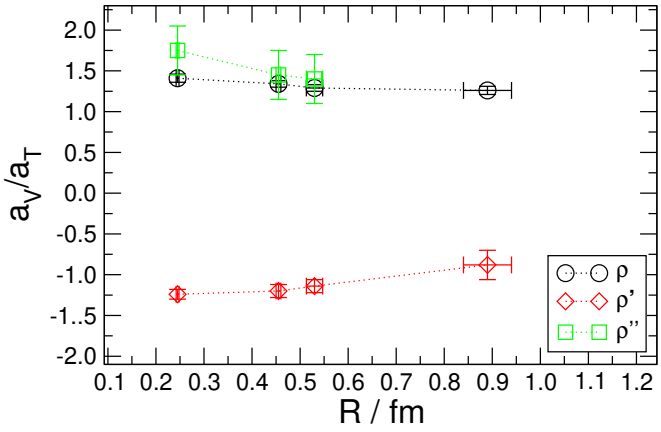

FIGURE B.2: Lattice measurement of operator contributions to the energy levels of ρ, ρ' and ρ'' as measured in [109,110].

which belong to two different representations of the chiral-parity group, *cf.* section 3.3.1. There exists a unitary transformation to connect the chiral-parity group representations to the angular momentum basis [111]

$$|\rho_{(0,1)\oplus(1,0)}\rangle = \sqrt{\frac{2}{3}}\,|1;^3S_1\rangle + \sqrt{\frac{1}{3}}\,|1;^3D_1\rangle \ , \tag{213a}$$

$$|\rho_{(1/2,1/2)_b}\rangle = \sqrt{\frac{1}{3}}\,|1;^3S_1\rangle - \sqrt{\frac{2}{3}}\,|1;^3D_1\rangle \ . \tag{213b}$$

Now by measuring the relative contributions of (212a) and (212b) to an energy level on the lattice, the partial wave content (213a)–(213b) can be extracted.

This was done in [109, 110] on a 16×32 lattice with lattice spacing $a = 0.1184(21)$ fm, $n_f = 2$ dynamical Overlap fermions and $m_\pi = (289.0 \pm 1.8)$ MeV. The following decomposition could be extracted:

$$|\rho(770)\rangle = +\,(0.998 \pm 0.002)\,|^3S_1\rangle - (0.05 \quad \pm 0.025)\,|^3D_1\rangle \ , \tag{214a}$$

$$|\rho(1450)\rangle = -\,(0.106 \pm 0.09 \ )\,|^3S_1\rangle - (0.994 \pm 0.005)\,|^3D_1\rangle \ , \tag{214b}$$

$$|\rho(1700)\rangle = +\,(0.99 \pm 0.01)\,|^3S_1\rangle - (0.01 \pm 0.12)\,|^3D_1\rangle \, . \tag{214c}$$

The results for $\rho(770)$ and $\rho(1450)$ are in obvious disagreement with [104] and the quark model suggestion. The discrepancy however is easily explained by comparing the non-relativistic reduction in both cases: while [104] relies on heavy quarks, the method using the chiral-parity group assumes ultra-relativistc quarks to render the chiral-parity group applicable in the first place.

Appendix C

Exotic Mesons

The quark model, as briefly introduced in section 2.3, describes the quantum numbers of a hadronic bound states in terms of its constituent quarks. In doing so, not all combinations of quantum numbers can be constructed. Such states of quantum numbers (32) are called exotic states.

Generally QCD does not forbid such states, and operators of exotic quantum numbers can be constructed. For a mesonic bound state *e.g.* additional quantum numbers can be carried by gluons, which do not contribute flavor content but possibly momentum and angular momentum[1].

On the lattice meson operators with quark content, as well as color-electric and color-magnetic contributions can be constructed, so-called *hybrid* mesons. Also pure glueballs without valence quarks are possible. Their overlap with physical states and signal strength will depend on the actual presence of gluonic modes in the considered channel. In [112] a few 'ordinary' mesonic states with additional admixture of gluonic degrees of freedom, as well as pure exotic operators are constructed.

The measurement of hybrid mesons might be of interest not only for comparison with experiment[2], but to shed light onto the role of explicit gluonic excitations, especially in the high temperature phase of QCD. As described in the main text of this thesis, the relative importance of color-electric and color-magnetic fields may shift significantly with increasing temperature. This could be verified with spectroscopy of hybrid operators.

C.1 Interpolator construction

In this section the construction of hybrid operators and its calculation on the lattice is briefly sketched. The operators of hybrid mesons are build ontop of ordinary meson operators by explicitly including gluonic degrees of freedom through the fieldstrength $G^{ab}_{\mu\nu}(x)$. The quantum numbers of the resulting operator are given by the combined symmetry properties.

A color-singlet hybrid operator $O_H(x)$ for isovector mesons is given by

$$O_H(x) = \bar{\Psi}_u(x)\Gamma G(x)\Psi_d(x) \tag{215}$$

The adjoint operator is given by

$$\begin{aligned} O_H(x)^\dagger &= \left(\bar{\Psi}_u(x)\Gamma G(x)\Psi_d(x)\right)^\dagger \\ &= -\bar{\Psi}_d(x)\gamma_4 G^\dagger(x)\Gamma^\dagger\gamma_4\Psi_u(x) \\ &= (\pm)\bar{\Psi}_d(x)\Gamma G^\dagger(x)\Psi_u(x), \end{aligned} \tag{216}$$

where the overall sign depends on $\gamma_4\Gamma^\dagger\gamma_4 = (\pm)\Gamma$.

[1] A second possibilty would be states of four or more quarks, *i.e.* tetra- and pentaquarks.

[2] A larger experiment dedicated to the measurement of exotic states would be *GlueX* at Jefferson Laboratory [113].

Now the diagonal correlation

$$\langle O_H(x) O_H(0)^\dagger \rangle \tag{217}$$

is evaluated for a given gaugefield configuration, i.e. the fermionic expectation value

$$\langle \bar{\Psi}_u(x) \Gamma G(x) \Psi_d(x) \bar{\Psi}_d(0) \Gamma G^\dagger(0) \Psi_u(0) \rangle_F \tag{218}$$

is done. Using explicit Dirac- and color-indices the Wick contraction can be done:

$$\begin{aligned}
&\left\langle \bar{\Psi}_u(x)^{\alpha_1}_{c_1} \Gamma_{\alpha_1\beta_1} G(x)_{c_1 d_1} \Psi_d(x)^{\beta_1}_{d_1} \bar{\Psi}_d(0)^{\alpha_2}_{c_2} \Gamma_{\alpha_2\beta_2} G^\dagger(0)_{c_2 d_2} \Psi_u(0)^{\beta_2}_{d_2} \right\rangle_F = \\
&\Gamma_{\alpha_1\beta_1} \Gamma_{\alpha_2\beta_2} G(x)_{c_1 d_1} G^\dagger(0)_{c_2 d_2} \left\langle \bar{\Psi}_u(x)^{\alpha_1}_{c_1} \Psi_d(x)^{\beta_1}_{d_1} \bar{\Psi}_d(0)^{\alpha_2}_{c_2} \Psi_u(0)^{\beta_2}_{d_2} \right\rangle_F = \\
&\Gamma_{\alpha_1\beta_1} \Gamma_{\alpha_2\beta_2} G(x)_{c_1 d_1} G^\dagger(0)_{c_2 d_2} D_d^{-1}(x|0)^{\beta_1\alpha_2}_{d_1 c_2} D_u^{-1}(0|x)^{\beta_2\alpha_1}_{d_2 c_1} = \\
&\Gamma_{\alpha_1\beta_1} \Gamma_{\alpha_2\beta_2} G(x)_{c_1 d_1} G^\dagger(0)_{c_2 d_2} D_d^{-1}(x|0)^{\beta_1\alpha_2}_{d_1 c_2} (\gamma_5)_{\alpha_1\alpha_1'} D_u^{-1}(x|0)^*_{\alpha_1'\beta_2'}{}_{c_1 d_2} (\gamma_5)_{\beta_2'\beta_2} = \\
&(\gamma_5\Gamma)_{\alpha_1\beta_1} (\Gamma\gamma_5)_{\alpha_2\beta_2} G(x)_{c_1 d_1} G^\dagger(0)_{c_2 d_2} D_d^{-1}(x|0)^{\beta_1\alpha_2}_{d_1 c_2} D_u^{-1}(x|0)^*_{\alpha_1'\beta_2'}{}_{c_1 d_2},
\end{aligned} \tag{219}$$

where the γ_5 hermiticity

$$D(x|y)^{\alpha\beta}_{cd} = (\gamma_5)_{\beta\beta'} D^{-1}(y|x)^*_{\beta'\alpha'}{}_{dc} (\gamma_5)_{\alpha'\alpha} \tag{220}$$

has been used. Here the Gamma structure Γ as well as the fieldstrength $G(x)$ carry external indices, which determine the quantum numbers of the state. They have been suppressed here and can easily be restored at the source and sink and give

$$\begin{aligned}
\langle O_H^k(x) O_H^l(0)^\dagger \rangle = (\gamma_5 \Gamma^k)_{\alpha_1\beta_1} (\Gamma^l \gamma_5)_{\alpha_2\beta_2} \times \\
G^k(x)_{c_1 d_1} G^{l\dagger}(0)_{c_2 d_2} D_d^{-1}(x|0)^{\beta_1\alpha_2}_{d_1 c_2} D_u^{-1}(x|0)^*_{\alpha_1'\beta_2'}{}_{c_1 d_2}
\end{aligned} \tag{221}$$

as final formula.

Following [112], hybrid and exotic states are now obtained by

$$\rho \otimes B: \quad \epsilon_{ijk} \bar{\Psi}^{c_1} \gamma_i \Psi^{c_2} G_{jk}^{c_1 c_2}, \tag{222a}$$

$$\rho \otimes B: \quad \bar{\Psi}^{c_1} \gamma_j \Psi^{c_2} G_{ji}^{c_1 c_2}, \tag{222b}$$

$$a_1 \otimes E: \quad \bar{\Psi}^{c_1} \gamma_5 \gamma_i \Psi^{c_2} G_{i0}^{c_1 c_2}. \tag{222c}$$

In (222a) a combination of the classical vector meson with the color-magnetic field gives the quantum numbers of the pion, hence this is a hybrid operator. (222b) couples the vector meson with the color-magnetic field to give a 1^{-+} state, which is a true exotic. (222c) corresponds to an exotic 0^{--} combination of the axial vector meson with the color-electric field.

C.2 Smearing & topological sector

Stout smearing [114] is a method to smooth gauge fields and remove ultraviolet fluctuations, thus speeding up convergence properties of iterative procedures and improve the signal strengh of gluonic observables. Stout smearing does not change the topology of a gauge field, therefore it can be used to 'flatten

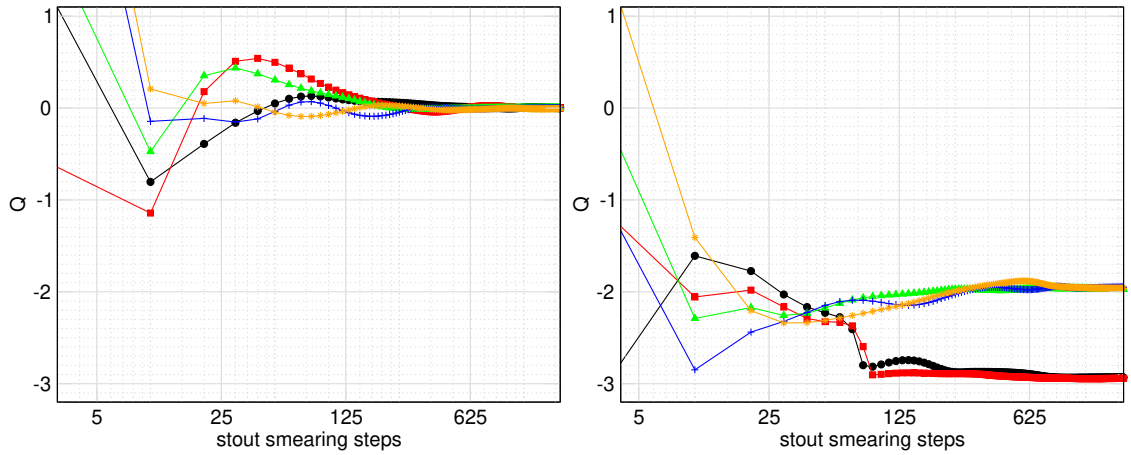

FIGURE C.1: Measurement of topological sector using stout smearing. Different lines correspond to different gauge configurations. The smearing parameters are $\rho_{jk} = 0.01$ for spatial links and $\rho_{4\mu} = 0.0$ for temporal links. The gauge configurations are from the ensemble described in B. For the configurations on the left side, the topological sector has been measured as $Q = 0$ by the zero modes of the overlap operator. For the configurations on the right side, a topological charge $Q = -2$ was measured through zero modes..

out' a gauge field before measuring the topological charge by integrating the local topological density, as described by (151).

A smearing step on a gauge field $U_\mu(x)$ is given by

$$U_\mu^{(n+1)}(x) = \exp\left(iQ_\mu^{(x)}(x)\right) U_\mu^{(x)}(x), \tag{223}$$

where the matrix Q is

$$Q_\mu(x) = \frac{\mathrm{i}}{2}\left(\Omega_\mu^\dagger(x) - \Omega_\mu(x)\right) - \frac{\mathrm{i}}{2N}\mathrm{Tr}\left[\Omega_\mu^\dagger(x) - \Omega_\mu(x)\right] \tag{224}$$

$$\Omega_\mu(x) = C_\mu(x)U_\mu^\dagger(x) \tag{225}$$

with

$$\begin{aligned} C_\mu(x) = \sum_{\nu\neq\mu} \rho_{\mu\nu}\big(&U_\nu(x)U_\mu(x+\hat{\nu})U_\nu^\dagger(x+\hat{\mu}) \\ &+U_\nu^\dagger(x-\hat{\nu})U_\mu(x-\hat{\nu})U_\nu(x-\hat{\nu}+\hat{\mu})\big). \end{aligned} \tag{226}$$

The matrix $Q_\mu(x)$ is hermitian and traceless, so $\exp(iQ_\mu(x))$ is an element of $\mathrm{SU}(3)$ and the whole operation gauge invariant. Spatial smearing uses

$$\rho_{jk} = \rho, \quad \rho_{4\mu} = 0, \tag{227}$$

and generally ρ as well as the number of total smearing steps N are free parameters.

An example of using stout smearing to measure the topological charge of gauge fields can be seen in figure C.1.

Appendix D

Spin $J = 0$ Mesons and low mode removal

In the following section unpublished data of the low mode trunaction procedure, as described in sections 4.1 and 4.4, on $J = 0$ mesons is presented. The trunaction procedure involves the construction of a reduced quark propagator

$$D_{red}^{-1} = D^{-1} - \sum_{i \leq k} \frac{1}{\lambda_i} |\lambda_i\rangle \langle\lambda_i| \gamma_5, \tag{228}$$

by manually subtracting k lowest modes $|\lambda_i\rangle$ of the Dirac operator from the full propagtator.

In tables D.1 and D.2 the isovector and isoscalar quark bilinears of $J = 0$ are listed. The $(1/2, 1/2)$ representations of the chiral-parity group include operators from both tables, which transform into each other via $\mathrm{SU}(2)_A$ transformations, *i.e.* $\pi \leftrightarrow \sigma$ and $\eta \leftrightarrow a_0$. Here only the isovectors are calculated. The smearing setup of the quark sources is the same as described in 4.4, and in the data presented here the 'wide' parameter set will be used. The gauge ensemble is the same as described in B.2, *i.e.* a fully dynamical $n_f = 2$ simulation using Overlap fermions on a $16^3 \times 32$ lattice.

In figure D.1 the temporal correlation function of operator $\bar{q}(\gamma_4 \otimes \frac{\vec{\tau}}{2})q$ is shown for various levels of removed low modes k. This operator does usually not propagate due to the conservation of the vector current (157). Furthermore, $\bar{q}q$-states in the $(0, 1) + (1, 0)$ representation of the chiral-parity group are forbidden for spin $J = 0$. However, after removing $k = 10$ modes, a very clean exponential decay becomes visible for this operator.

In figure D.2 correlation functions of all four operators from table D.1 are given. While it can be seen that $\mathrm{SU}(2)_A$ and $\mathrm{U}(1)_A$ connected operators become degenerate upon truncation, the two pairs itself differ. For the pion and parity partner the correlation functions do not show clean exponential behaviour, which means that no light states show up in the spectrum, *i.e.* the pion as Goldstone mode is gone.

	J^{PC}	operator	chiral rep.	
π	0^{-+}	$\bar{q}(\gamma_5 \otimes \frac{\vec{\tau}}{2})q$	$(1/2, 1/2)_a$	$\rceil\, U(1)_A$
a_0	0^{++}	$\bar{q}(\mathbb{1} \otimes \frac{\vec{\tau}}{2})q$	$(1/2, 1/2)_b$	
	0^{-+}	$\bar{q}(\gamma_5\gamma_0 \otimes \frac{\vec{\tau}}{2})q$	$(0, 1) + (1, 0)$	$\rceil\, SU(2)_A$
	0^{+-}	$\bar{q}(\gamma_0 \otimes \frac{\vec{\tau}}{2})q$	$(0, 1) + (1, 0)$	

TABLE D.1: $J = 0$ isovector operators and transformations.

	J^{PC}	operator	chiral rep.	
η	0^{-+}	$\bar{q}(\gamma_5 \otimes \mathbb{1}_F)q$	$(1/2,1/2)_b$	$\Big]\, U(1)_A$
σ	0^{++}	$\bar{q}(\mathbb{1} \otimes \mathbb{1}_F)q$	$(1/2,1/2)_a$	
	0^{-+}	$\bar{q}(\gamma_5\gamma_0 \otimes \mathbb{1}_F)q$	$(0,0)$	
	0^{+-}	$\bar{q}(\gamma_0 \otimes \mathbb{1}_F)q$	$(0,0)$	

TABLE D.2: $J = 0$ isoscalar operators and transformations.

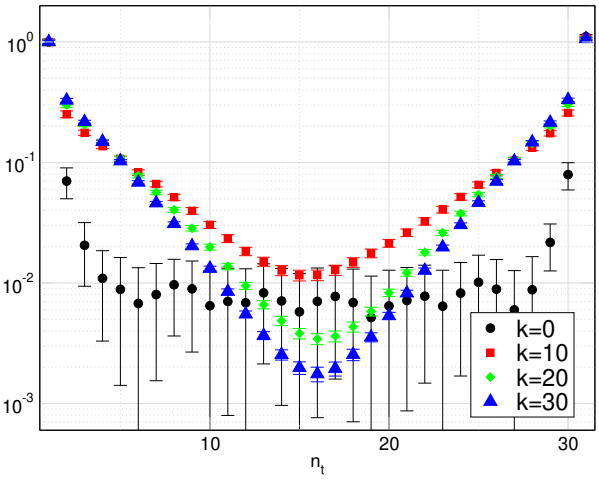

FIGURE D.1: Temporal correlation functions for $\bar{q}(\gamma_4 \otimes \frac{\vec{\tau}}{2})q$ operator. k denotes the number of removed eigenmodes. $k = 0$ is the untrunced case, *i.e.* the full quark propagator is used.

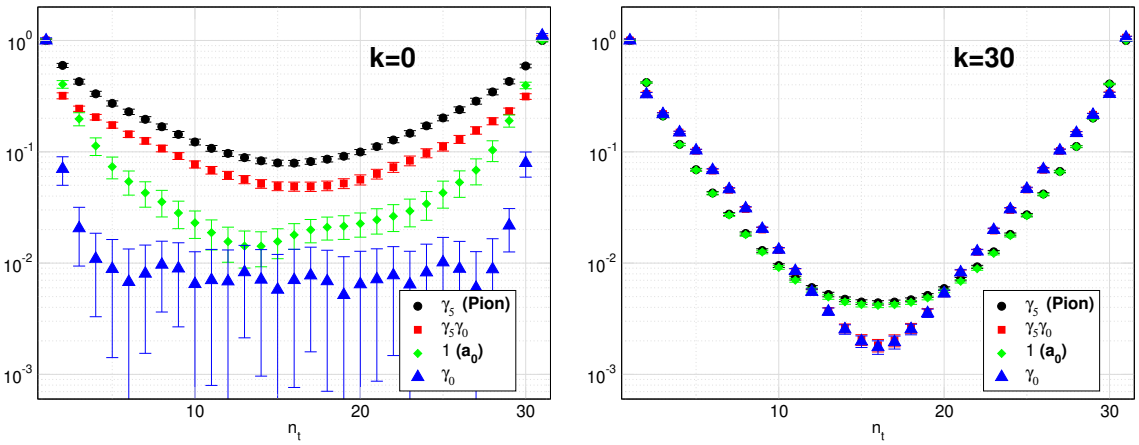

FIGURE D.2: Full (*left side*) and $k = 30$ truncated (*right side*) correlation functions for isovector $J = 0$ mesons operators. The gamma structure in the legend denotes the corresponding operators from table D.1.

References

[1] Thomas A. DeGrand and Anna Hasenfratz. Low lying fermion modes, topology and light hadrons in quenched QCD. *Phys. Rev.*, D64:034512, 2001, hep-lat/0012021.

[2] Thomas A. DeGrand. Short distance current correlators: Comparing lattice simulations to the instanton liquid. *Phys. Rev.*, D64:094508, 2001, hep-lat/0106001.

[3] Thomas A. DeGrand. Eigenvalue decomposition of meson correlators. *Phys. Rev.*, D69:074024, 2004, hep-ph/0310303.

[4] C. B. Lang and Mario Schrock. Unbreaking chiral symmetry. *Phys. Rev.*, D84:087704, 2011, 1107.5195.

[5] C. B. Lang and Mario Schrock. Effects of the low lying Dirac modes on the spectrum of ground state mesons. *PoS*, LATTICE2011:111, 2011, 1110.6149.

[6] L. Ya. Glozman, C. B. Lang, and M. Schrock. Symmetries of hadrons after unbreaking the chiral symmetry. *Phys. Rev.*, D86:014507, 2012, 1205.4887.

[7] L. Ya. Glozman, C. B. Lang, and M. Schrock. Effects of the low lying Dirac modes on excited hadrons in lattice QCD. *Acta Phys. Polon. Supp.*, 5:1001–1006, 2012, 1207.7323.

[8] M. Schröck, M. Denissenya, L. Ya. Glozman, and C. B. Lang. More effects of Dirac low-mode removal. *PoS*, LATTICE2013:116, 2014, 1309.0202.

[9] M. Denissenya, L. Ya. Glozman, C. B. Lang, and M. Schröck. Effects of Low vs. High Fermionic Modes on Hadron Mass Generation. *PoS*, LATTICE2013:115, 2014, 1310.8584.

[10] M. Denissenya and L. Ya. Glozman. Chiral symmetry breaking and the generation of light hadron masses. 2014, 1401.6034.

[11] M. Denissenya, L. Ya. Glozman, and C. B. Lang. Symmetries of mesons after unbreaking of chiral symmetry and their string interpretation. *Phys. Rev.*, D89(7):077502, 2014, 1402.1887.

[12] M. Denissenya, L. Ya. Glozman, and C. B. Lang. Isoscalar mesons upon unbreaking of chiral symmetry. *Phys. Rev.*, D91(3):034505, 2015, 1410.8751.

[13] M. Denissenya, L. Ya. Glozman, and C. B. Lang. Mesons upon low-lying Dirac mode exclusion. *PoS*, LATTICE2014:068, 2014, 1411.1578.

[14] M. Denissenya, L. Ya. Glozman, and M. Pak. Evidence for a new $SU(4)$ symmetry with $J = 2$ mesons. *Phys. Rev.*, D91(11):114512, 2015, 1505.03285.

[15] M. Denissenya, L. Ya. Glozman, and M. Pak. Emergence of a new $SU(4)$ symmetry in the baryon spectrum. *Phys. Rev.*, D92(7):074508, 2015, 1508.01413. [Erratum: Phys. Rev.D92,no.9,099902(2015)].

[16] M. Denissenya, L. Glozman, and M. Pak. Testing the SU(4) degeneracy after low-mode removal with J = 2 mesons. *PoS*, LATTICE2015:063, 2016, 1510.09015.

[17] A. Bazavov et al. The chiral transition and $U(1)_A$ symmetry restoration from lattice QCD using Domain Wall Fermions. *Phys. Rev.*, D86:094503, 2012, 1205.3535.

[18] Guido Cossu, Sinya Aoki, Hidenori Fukaya, Shoji Hashimoto, Takashi Kaneko, Hideo Matsufuru, and Jun-Ichi Noaki. Finite temperature study of the axial U(1) symmetry on the lattice with overlap fermion formulation. *Phys. Rev.*, D87(11):114514, 2013, 1304.6145. [Erratum: Phys. Rev.D88,no.1,019901(2013)].

[19] A. Tomiya, G. Cossu, S. Aoki, H. Fukaya, S. Hashimoto, T. Kaneko, and J. Noaki. Evidence of effective axial U(1) symmetry restoration at high temperature QCD. *Phys. Rev.*, D96(3):034509, 2017, 1612.01908. [Addendum: Phys. Rev.D96,no.7,079902(2017)].

[20] Kei Suzuki, Sinya Aoki, Yasumichi Aoki, Guido Cossu, Hidenori Fukaya, and Shoji Hashimoto. Axial $U(1)$ symmetry at high temperature in 2-flavor lattice QCD. *EPJ Web Conf.*, 175:07025, 2018, 1711.09239.

[21] S. Pokorski. *GAUGE FIELD THEORIES*. Cambridge University Press, 2005.

[22] F. Halzen and Alan D. Martin. *QUARKS AND LEPTONS: AN INTRODUCTORY COURSE IN MODERN PARTICLE PHYSICS*. 1984.

[23] Steven Weinberg. *The quantum theory of fields. Vol. 2: Modern applications*. Cambridge University Press, 2013.

[24] Michael E. Peskin and Daniel V. Schroeder. *An Introduction to quantum field theory*. Addison-Wesley, Reading, USA, 1995.

[25] I. Montvay and G. Munster. *Quantum fields on a lattice*. Cambridge Monographs on Mathematical Physics. Cambridge University Press, 1997.

[26] Christof Gattringer and Christian B. Lang. Quantum chromodynamics on the lattice. *Lect. Notes Phys.*, 788:1–343, 2010.

[27] H. Fritzsch, Murray Gell-Mann, and H. Leutwyler. Advantages of the Color Octet Gluon Picture. *Phys. Lett.*, 47B:365–368, 1973.

[28] Murray Gell-Mann. A Schematic Model of Baryons and Mesons. *Phys. Lett.*, 8:214–215, 1964.

[29] G. Zweig. An SU(3) model for strong interaction symmetry and its breaking. Version 1. 1964.

[30] G. Zweig. An SU(3) model for strong interaction symmetry and its breaking. Version 2. In D.B. Lichtenberg and Simon Peter Rosen, editors, *DEVELOPMENTS IN THE QUARK THEORY OF HADRONS. VOL. 1. 1964 - 1978*, pages 22–101. 1964.

[31] M. Tanabashi et al. Review of Particle Physics. *Phys. Rev.*, D98(3):030001, 2018.

[32] V. E. Barnes et al. Observation of a Hyperon with Strangeness -3. *Phys. Rev. Lett.*, 12:204–206, 1964.

[33] Y. Aoki, G. Endrodi, Z. Fodor, S. D. Katz, and K. K. Szabo. The Order of the quantum chromodynamics transition predicted by the standard model of particle physics. *Nature*, 443:675–678, 2006, hep-lat/0611014.

[34] A. Bazavov et al. The chiral and deconfinement aspects of the QCD transition. *Phys. Rev.*, D85:054503, 2012, 1111.1710.

[35] Szabocls Borsanyi, Zoltan Fodor, Christian Hoelbling, Sandor D. Katz, Stefan Krieg, and Kalman K. Szabo. Full result for the QCD equation of state with 2+1 flavors. *Phys. Lett.*, B730:99–104, 2014, 1309.5258.

[36] A. Bazavov, P. Petreczky, and J. H. Weber. Equation of State in 2+1 Flavor QCD at High Temperatures. *Phys. Rev.*, D97(1):014510, 2018, 1710.05024.

[37] T. Matsui and H. Satz. J/ψ Suppression by Quark-Gluon Plasma Formation. *Phys. Lett.*, B178:416–422, 1986.

[38] Johann Rafelski and Berndt Muller. Strangeness Production in the Quark - Gluon Plasma. *Phys. Rev. Lett.*, 48:1066, 1982. [Erratum: Phys. Rev. Lett.56,2334(1986)].

[39] Miklos Gyulassy and Michael Plumer. Jet Quenching in Dense Matter. *Phys. Lett.*, B243:432–438, 1990.

[40] J. Adams et al. Azimuthal anisotropy in Au+Au collisions at s(NN)**(1/2) = 200-GeV. *Phys. Rev.*, C72:014904, 2005, nucl-ex/0409033.

[41] K Aamodt et al. Elliptic flow of charged particles in Pb-Pb collisions at 2.76 TeV. *Phys. Rev. Lett.*, 105:252302, 2010, 1011.3914.

[42] Georges Aad et al. Measurement of the pseudorapidity and transverse momentum dependence of the elliptic flow of charged particles in lead-lead collisions at $\sqrt{s_{NN}} = 2.76$ TeV with the ATLAS detector. *Phys. Lett.*, B707:330–348, 2012, 1108.6018.

[43] Berndt Muller. Statistical fluctuations as probes of dense matter. *Nucl. Phys.*, A702:281–290, 2002, nucl-th/0111008.

[44] Chi Yang. The STAR beam energy scan phase II physics and upgrades. *Nucl. Phys.*, A967:800–803, 2017.

[45] Kenneth G. Wilson. Confinement of Quarks. *Phys. Rev.*, D10:2445–2459, 1974. [,319(1974)].

[46] G. Ecker. Chiral symmetry. *Lect. Notes Phys.*, 521:83–129, 1999, hep-ph/9805500.

[47] L. Ya. Glozman. Restoration of chiral and U(1)A symmetries in excited hadrons. *Phys. Rept.*, 444:1–49, 2007, hep-ph/0701081.

[48] R. A. Bertlmann. *Anomalies in quantum field theory*. 1996.

[49] Kazuo Fujikawa. Path Integral Measure for Gauge Invariant Fermion Theories. *Phys. Rev. Lett.*, 42:1195–1198, 1979.

[50] Kazuo Fujikawa. Path Integral for Gauge Theories with Fermions. *Phys. Rev.*, D21:2848, 1980. [Erratum: Phys. Rev.D22,1499(1980)].

[51] M. F. Atiyah and I. M. Singer. The Index of elliptic operators. 1. *Annals Math.*, 87:484–530, 1968.

[52] M. F. Atiyah and I. M. Singer. The Index of elliptic operators. 5. *Annals Math.*, 93:139–149, 1971.

[53] Gerard 't Hooft. Symmetry Breaking Through Bell-Jackiw Anomalies. *Phys. Rev. Lett.*, 37:8–11, 1976. [,226(1976)].

[54] Jeffrey Goldstone, Abdus Salam, and Steven Weinberg. Broken Symmetries. *Phys. Rev.*, 127:965–970, 1962.

[55] C. Vafa and Edward Witten. Restrictions on Symmetry Breaking in Vector-Like Gauge Theories. *Nucl. Phys.*, B234:173–188, 1984.

[56] Murray Gell-Mann, R. J. Oakes, and B. Renner. Behavior of current divergences under SU(3) x SU(3). *Phys. Rev.*, 175:2195–2199, 1968.

[57] Thomas D. Cohen and Xiang-Dong Ji. Chiral multiplets of hadron currents. *Phys. Rev.*, D55:6870–6876, 1997, hep-ph/9612302.

[58] Holger Bech Nielsen and M. Ninomiya. Absence of Neutrinos on a Lattice. 1. Proof by Homotopy Theory. *Nucl. Phys.*, B185:20, 1981. [,533(1980)].

[59] Holger Bech Nielsen and M. Ninomiya. Absence of Neutrinos on a Lattice. 2. Intuitive Topological Proof. *Nucl. Phys.*, B193:173–194, 1981.

[60] Holger Bech Nielsen and M. Ninomiya. No Go Theorem for Regularizing Chiral Fermions. *Phys. Lett.*, 105B:219–223, 1981.

[61] Paul H. Ginsparg and Kenneth G. Wilson. A Remnant of Chiral Symmetry on the Lattice. *Phys. Rev.*, D25:2649, 1982.

[62] Tom Banks and A. Casher. Chiral Symmetry Breaking in Confining Theories. *Nucl. Phys.*, B169:103–125, 1980.

[63] L. Ya. Glozman. SU(4) symmetry of the dynamical QCD string and genesis of hadron spectra. *Eur. Phys. J.*, A51(3):27, 2015, 1407.2798.

[64] L. Ya. Glozman. No deconfinement in QCD ? 2015, 1512.06703.

[65] L. Ya. Glozman. A hidden classical symmetry of QCD. *EPJ Web Conf.*, 164:03002, 2017, 1608.07269.

[66] Thomas D. Cohen. On the nature of an emergent symmetry in QCD. *Phys. Rev.*, D93(3):034508, 2016, 1511.03956.

[67] L. Ya. Glozman. $SU(2N_F)$ hidden symmetry of QCD. 2015, 1511.05857.

[68] M. Shifman. Dynamically Emergent Flavor in a Confining Theory with Unbroken Chiral Symmetry. *Phys. Rev.*, D93(7):074035, 2016, 1602.06699.

[69] Herbert Neuberger. Exactly massless quarks on the lattice. *Phys. Lett.*, B417:141–144, 1998, hep-lat/9707022.

[70] Herbert Neuberger. A Practical implementation of the overlap Dirac operator. *Phys. Rev. Lett.*, 81:4060–4062, 1998, hep-lat/9806025.

[71] R. C. Brower, H. Neff, and K. Orginos. Mobius fermions. *Nucl. Phys. Proc. Suppl.*, 153:191–198, 2006, hep-lat/0511031.

[72] Richard C. Brower, Harmut Neff, and Kostas Orginos. The Möbius domain wall fermion algorithm. *Comput. Phys. Commun.*, 220:1–19, 2017, 1206.5214.

[73] M. Luscher and P. Weisz. On-Shell Improved Lattice Gauge Theories. *Commun. Math. Phys.*, 97:59, 1985. [Erratum: Commun. Math. Phys.98,433(1985)].

[74] G. Curci, P. Menotti, and G. Paffuti. Symanzik's Improved Lagrangian for Lattice Gauge Theory. *Phys. Lett.*, 130B:205, 1983. [Erratum: Phys. Lett.135B,516(1984)].

[75] Christof Gattringer, Roland Hoffmann, and Stefan Schaefer. Setting the scale for the Luscher-Weisz action. *Phys. Rev.*, D65:094503, 2002, hep-lat/0112024.

[76] Benoit Blossier, Michele Della Morte, Georg von Hippel, Tereza Mendes, and Rainer Sommer. On the generalized eigenvalue method for energies and matrix elements in lattice field theory. *JHEP*, 04:094, 2009, 0902.1265.

[77] Tommy Burch, Christof Gattringer, Leonid Ya. Glozman, Reinhard Kleindl, C. B. Lang, and Andreas Schaefer. Spatially improved operators for excited hadrons on the lattice. *Phys. Rev.*, D70:054502, 2004, hep-lat/0405006.

[78] William A. Bardeen, A. Duncan, E. Eichten, Nathan Isgur, and H. Thacker. Chiral Loops and Ghost States in the Quenched Scalar Propagator. *Phys. Rev.*, D65:014509, 2001, hep-lat/0106008.

[79] Sasa Prelovsek, C. Dawson, T. Izubuchi, K. Orginos, and A. Soni. Scalar meson in dynamical and partially quenched two-flavor QCD: Lattice results and chiral loops. *Phys. Rev.*, D70:094503, 2004, hep-lat/0407037.

[80] Sasa Prelovsek. Simulations of light scalar mesons on the lattice and related difficulties. 2008, 0804.2549. [AIP Conf. Proc.1030,311(2008)].

[81] Guido Cossu, Hidenori Fukaya, Shoji Hashimoto, and Akio Tomiya. Violation of chirality of the Möbius domain-wall Dirac operator from the eigenmodes. *Phys. Rev.*, D93(3):034507, 2016, 1510.07395.

[82] S. Hashimoto, S. Aoki, G. Cossu, H. Fukaya, T. Kaneko, J. Noaki, and P. A. Boyle. Residual mass in five-dimensional fermion formulations. *PoS*, LATTICE2013:431, 2014.

[83] Junichi Noaki, S. Aoki, G. Cossu, H. Fukaya, S. Hashimoto, and T. Kaneko. Fine lattice simulations with the Ginsparg-Wilson fermions. *PoS*, LATTICE2014:069, 2014.

[84] J. Noaki, S. Aoki, G. Cossu, H. Fukaya, S. Hashimoto, and T. Kaneko. Fine lattice simulations with chirally symmetric fermions. *PoS*, LATTICE2013:263, 2014.

[85] Guido Cossu, Jun Noaki, Shoji Hashimoto, Takashi Kaneko, Hidenori Fukaya, Peter A. Boyle, and Jun Doi. JLQCD IroIro++ lattice code on BG/Q. In *Proceedings, 31st International Symposium on Lattice Field Theory (Lattice 2013): Mainz, Germany, July 29-August 3, 2013*, 2013, 1311.0084.

[86] Martin Lüscher. Properties and uses of the Wilson flow in lattice QCD. *JHEP*, 08:071, 2010, 1006.4518. [Erratum: JHEP03,092(2014)].

[87] Dirk Brommel, Peter Crompton, Christof Gattringer, Leonid Ya. Glozman, C. B. Lang, Stefan Schaefer, and Andreas Schafer. Excited nucleons with chirally improved fermions. *Phys. Rev.*, D69:094513, 2004, hep-ph/0307073.

[88] Christof Gattringer. personal communication.

[89] C. Rohrhofer, Y. Aoki, G. Cossu, H. Fukaya, L. Ya. Glozman, S. Hashimoto, C. B. Lang, and S. Prelovsek. Approximate degeneracy of $J = 1$ spatial correlators in high temperature QCD. *Phys. Rev.*, D96(9):094501, 2017, 1707.01881.

[90] Christian Rohrhofer, Yasumichi Aoki, Guido Cossu, Hidenori Fukaya, Leonid Glozman, Shoji Hashimoto, Christian B. Lang, and Sasa Prelovsek. Degeneracy of vector-channel spatial correlators in high temperature QCD. In *35th International Symposium on Lattice Field Theory (Lattice 2017) Granada, Spain, June 18-24, 2017*, 2017, 1710.08287.

[91] C. Rohrhofer, Y. Aoki, G. Cossu, L. Ya. Glozman, S. Hashimoto, and S. Prelovsek. Meson correlation functions at high temperature QCD: $SU(2)_{CS}$ symmetry vs. free quarks. In *36th International Symposium on Lattice Field Theory (Lattice 2018) East Lansing, MI, United States, July 22-28, 2018*, 2018, 1809.00244.

[92] Gert Aarts, Chris Allton, Simon Hands, Benjamin Jäger, Chrisanthi Praki, and Jon-Ivar Skullerud. Nucleons and parity doubling across the deconfinement transition. *Phys. Rev.*, D92(1):014503, 2015, 1502.03603.

[93] Gert Aarts, Chris Allton, Davide De Boni, Simon Hands, Benjamin Jäger, Chrisanthi Praki, and Jon-Ivar Skullerud. Light baryons below and above the deconfinement transition: medium effects and parity doubling. *JHEP*, 06:034, 2017, 1703.09246.

[94] Saumen Datta, Sourendu Gupta, M. Padmanath, Jyotirmoy Maiti, and Nilmani Mathur. Nucleons near the QCD deconfinement transition. *JHEP*, 02:145, 2013, 1212.2927.

[95] Chihiro Sasaki. Parity doubling of baryons in a chiral approach with three flavors. *Nucl. Phys.*, A970:388–397, 2018, 1707.05081.

[96] Thomas D. Cohen. The High temperature phase of QCD and U(1)-A symmetry. *Phys. Rev.*, D54:R1867–R1870, 1996, hep-ph/9601216.

[97] Hidenori Fukaya. Can axial U(1) anomaly disappear at high temperature? *EPJ Web Conf.*, 175:01012, 2018, 1712.05536.

[98] L. Ya. Glozman and M. Pak. Exploring a new SU(4) symmetry of meson interpolators. *Phys. Rev.*, D92(1):016001, 2015, 1504.02323.

[99] Aharon Casher. Chiral Symmetry Breaking in Quark Confining Theories. *Phys. Lett.*, 83B:395–398, 1979.

[100] L. Ya. Glozman. Confined but chirally symmetric hadrons at large density and the Casher's argument. *Phys. Rev.*, D80:037701, 2009, 0907.1473.

[101] Larry McLerran and Robert D. Pisarski. Phases of cold, dense quarks at large N(c). *Nucl. Phys.*, A796:83–100, 2007, 0706.2191.

[102] Carleton E. Detar and John B. Kogut. The Hadronic Spectrum of the Quark Plasma. *Phys. Rev. Lett.*, 59:399, 1987.

[103] Carleton E. Detar and John B. Kogut. Measuring the Hadronic Spectrum of the Quark Plasma. *Phys. Rev.*, D36:2828, 1987.

[104] Jozef J. Dudek. The lightest hybrid meson supermultiplet in QCD. *Phys. Rev.*, D84:074023, 2011, 1106.5515.

[105] Leonid Ya. Glozman, C. B. Lang, and Markus Limmer. Angular momentum content of the rho-meson in lattice QCD. *Phys. Rev. Lett.*, 103:121601, 2009, 0905.0811.

[106] Leonid Ya. Glozman, C. B. Lang, and Markus Limmer. The Chiral and angular momentum content of the rho-meson. *Few Body Syst.*, 47:91–103, 2010, 0909.2939.

[107] L. Ya. Glozman, C. B. Lang, and M. Limmer. Effective chiral restoration in the ρ'-meson in lattice QCD. *Phys. Rev.*, D82:097501, 2010, 1007.1346.

[108] L. Ya. Glozman, C. B. Lang, and M. Limmer. Chiral symmetry breaking and the spin content of the rho and rho' mesons. *Phys. Lett.*, B705:129–133, 2011, 1106.1010.

[109] C. Rohrhofer, M. Pak, and L. Ya. Glozman. Angular momentum content of the $\rho(1450)$ from chiral lattice fermions. *Bled Workshops Phys.*, 17(1):20–24, 2016, 1603.04665.

[110] Christian Rohrhofer, Markus Pak, and Leonid Glozman. Angular and chiral content of the ρ and ρ' mesons. *PoS*, LATTICE2016:099, 2016.

[111] L. Ya. Glozman and A. V. Nefediev. Chiral symmetry and the string description of excited hadrons. *Phys. Rev.*, D76:096004, 2007, 0704.2673.

[112] Claude W. Bernard et al. Exotic mesons in quenched lattice QCD. *Phys. Rev.*, D56:7039–7051, 1997, hep-lat/9707008.

[113] Daniel S. Carman. GlueX: The Search for gluonic excitations at Jefferson Laboratory. *AIP Conf. Proc.*, 814:173–182, 2006, hep-ex/0511030. [,173(2005)].

[114] Colin Morningstar and Mike J. Peardon. Analytic smearing of SU(3) link variables in lattice QCD. *Phys. Rev.*, D69:054501, 2004, hep-lat/0311018.

Acknowledgements

First and foremost I want to express deep gratitude to my advisor Leonid Glozman for the introduction to interesting topics in particle physics, sharing his knowledge, and the possibilities to participate at international conferences. I would like to say a very warm thank you to Shoji Hashimoto for the hospitality during my research stay at KEK. I learned a lot about physics, technicalities and working in a collaboration during these months. For various discussions on physics and their collaboration I want to thank Christian Lang, Christof Gattringer, Sasa Prelovsek, Hidenori Fukaya, Yasumichi Aoki and Guido Cossu. For their company while drinking coffee, eating burgers and related activities I want to thank Angel, Brian, Carlotta, Daniel, Franzi, Jordi, Katsumasa, Lukas, Marco, Mario, Oliver, Pablo, Pascal and Vincenzo. For their help in fighting bureaucracy I want to thank Fanny Maetz and Makiko Oishi. The author would like to acknowledge the use of HPC resources provided by ZID at the University of Graz, the Vienna Scientifc Cluster, and especially the efforts of Ursula Winkler. Special thanks go to Walter Melcher for his catching enthusiasm for science in general, and the etching at the beginning of this thesis in particular. At last I want to thank my parents Franz and Christine, my grandparents Franz and Gerti, and my aunt Veronika for their constant support and thus making this education possible in the first place. *Thank you!*